Thermodynamic Modelling of High Strength, High Toughness Ti Alloys

By

Hang Wang

School of Metallurgy and Materials

University of Birmingham

A thesis submitted to:
The University of Birmingham.
for the degree of:
DOCTOR OF PHILOSOPHY

School of Metallurgy & Materials
The University of Birmingham

February 2012

Abstract

Titanium alloys with good combinations of toughness and strength are being designed for aerospace applications: *e.g.* aeroengine compressors and aircraft undercarriages. It is not an easy process to optimise the balance between toughness and strength in this system, and in practice some aspects of the physical metallurgy of titanium alloys are not very well understood, such as the B2-type ordering in titanium alloys. The aim of this work mainly concerns the development of thermodynamic models, based upon CALPHAD techniques (CALculation of PHAse Diagrams).

First-principles calculations were performed in order to provide the thermodynamic modelling with information concerning sublattice occupation. The energies of formation of different point defects in the ordered B2 phase of the Ti-Al binary system have been predicted. The dominant point defects in the sublattice of the B2-TiAl structure were determined to be either substitutional vacancies or anti-site defects, depending on the major element in the alloy. The concentrations of total and thermal point defects were estimated in the present work. The results of first-principles calculations have been adopted in the CALPHAD thermodynamic modelling.

Thermodynamic assessment of the Ti-Al-Cr-V quaternary system was carried out, neglecting substitutional vacancies. A two sublattice model for B2 phase $(Al,Cr,Ti,V)_{0.5}:(Al,Cr,Ti,V)_{0.5}$ was used and a set of self-consistent thermodynamic parameters is presented. The predicted phase equilibria and order/disorder transformation temperature are shown to be in good agreement with experimental information, both in the

Ti-Al-Cr-V quaternary system and in the important binary and ternary subsystems. The modelling results were used to predict the B2-stable region, which is important for the design of titanium alloys. Next, substitutional vacancies were taken into account in a thermodynamic model of the B2 phase $(\mathrm{Al,Ti,V,Va})_{0.5}:(\mathrm{Al,Ti,V,Va})_{0.5}$ in the Ti-Al-V ternary system, taking into account the theoretical results of first-principles calculations. The temperature of the β transus in Ti-6Al-4V alloy has been predicted to aid simulation of microstructure evolution. Experiments were carried out in order to calibrate the thermodynamic models, and to investigate the effect of B2-ordering on the kinetics of α precipitation from the β matrix.

By using the obtained thermodynamic parameters, two databases of atomic mobilities were developed – one with substitutional vacancies and the other without. The calculated results from both databases fit the experimental data: concentration profiles, diffusivities and diffusion paths. Finally, microstructural kinetics associated with the β/α phase transformation in the Ti-6Al-4V alloy has been simulated using the phase-field method coupled with the CALPHAD approach. The needle-shape α structure was simulated and the mechanism of formation of Widmanstätten α structure was studied.

For my parents

Acknowledgements

It has been a wonderful experience for me to study at the University of Birmingham. During these three and a half years, I have fallen in love with this country, this university and this research group. It has provided me with the chance to learn professional skills while enjoying the fabulous civilisation in Europe.

My first thanks must be given to my supervisor Prof. Roger C. Reed. Although he is an extremely busy man, he has always found an opportunity to supervise me. His supervision is very special from that of any other professors I have ever met. The guidance from him is always thorough, which has provided me with an overview of interdisciplinary research work. Thanks to his suggestions, I felt confident with the standard of my research.

I also thank Prof. Xinhua Wu and Prof. Michael H. Loretto for their help with experimental work. I would also like to thank Dr. Nils Warnken for his suggestions on my work – especially my first lesson on MICRESS software. Also, I am honored to be Dr. Jean-Christophe Gebelin's dearest student, and I will forever remember the experience of VASP compilation with his help.

I am highly appreciative of the support from my friends, Dr. Lijun Zhang, Dr. Xiaoma Tao, Dr. Jianglin Huang, Dr. Atsushi Sato, Mr. Christopher Watson and all the people who have helped me.

Contents

List of illustrations

List of tables

Chapter 1 Introduction

1.1 Phase diagram and computational materials design

In a phase diagram, the coordinate axes are independent variables and the coordinate space shows the 'state of the system', *i.e.* how many and which phases are in equilibrium at defined conditions (most often at some certain temperature and mean composition) [1]. The equilibrium state of a system is described by classical thermodynamics [1]. Because alloy systems try to reach this equilibrium state during processing, it is a necessary foundation for materials design and development.

In the field of computational thermodynamics, data from thermodynamics, phase diagrams, and atomistic properties are combined together into a unified and consistent model. Computational thermodynamics of equilibria can then be used to construct various types of diagram, with phase diagrams among the most useful [2]. It has been employed in a wide field of applications, and many examples can be found in the recent work by Kaufman [3].

1.2 High strength, high toughness Ti alloys

Increase in toughness in a Ti-based alloy is sometimes coupled with decrease in strength; therefore the possibility of increasing toughness dramatically whilst maintaining or slightly increasing tensile strength opens up a wide range of applications in titanium metallurgy. If the approach of optimising balance of properties is successful, it would lead to a reassessment of the role of Ti-based alloys in areas where high strength and high toughness are required, such as aircraft undercarriages, artillery, armoured vehicles and spacecraft.

It has been shown that addition of carbon results in a dramatic decrease in the extent of grain boundary α and a refinement of the alpha precipitated within the grains [4]. The presence of carbon in solution dramatically slows down diffusion of oxygen to the grain boundaries during ageing and it has thus been inferred that segregation of oxygen (an α stabiliser) to grain boundaries is a prime factor influencing grain boundary alpha precipitation. The mechanism of refinement of the alpha within the grains is not understood, although it has been suggested that the carbon atoms, which may be associated with the oxygen atoms, act as nuclei – perhaps with the aid of quenched-in vacancies. The suggestion, that vacancies may be involved in ageing, is consistent with the observation that the ageing response is strongly influenced by the time taken to heat samples to the ageing temperature [4], as well as work which showed that the kinetics of hardening associated with the precipitation of α are strongly influenced by the quenching rate [5, 6].

It is of course widely accepted that the thermal vacancy concentration is very small in bcc metals/alloys, and equally well known that alloys with the ordered B2 crystal structure can develop very high concentrations of vacancies [7, 8]. In Ti-25V-15Cr-6Al (where B2 has been identified) the neutron scattering factors for the various atoms are very different, but the site occupancy, determined using ALCHEMI (Atom Location by Channelling-enhanced Emission) on this alloy [9], shows that the scattering factors from the two sites in the B2 crystal are very similar for neutrons. Hence it is possible that alloys are ordered so that they may have high vacancy concentrations, but no direct evidence has been presented so far.

1.3 The scope of the present work

The main objective of the present work is a fundamental investigation of the thermodynamic modelling of the Ti alloys systems to predict the presence of the ordered B2 structure. In addition, first-principles calculations are also to be used as a necessary pre-condition of the thermodynamic modelling. The simulation of atomic mobility and phase transformation in the Ti-Al-V alloy is also a meaningful kinetic extension of the thermodynamic work, and can be used to analyse the phase evolution in high strength, high toughness Ti alloys.

In chapter 2, the background of the physical metallurgy of Ti alloys and ordering in those alloys is described. It also gives an introduction of the modelling methods used in the present work, such as first-principles calculations, CALPHAD (CALculation of PHAse Diagrams), and phase-field simulations.

In chapter 3, the methodology of the modelling work is specified. The framework of the present work is illustrated by a flow chart followed by a separate section in which each modelling procedure is explained in detail.

In chapter 4, the results of first-principles calculations are presented. The site preference of the point defects in the Ti-Al binary system has been predicted. It provides information concerning crystal structure needed to inform the thermodynamic modelling of chapter 5.

In chapter 5, a thermodynamic database for the Ti-Al-Cr-V quaternary system is created as an addendum to a commercially available Ti-alloy database. Some experiments have been carried out to examine the accuracy of the database, and to analyse the effect of thermal vacancies on the kinetics of α precipitating from β matrix. The Ti-Al-V ternary system is re-optimised considering the site preference of the point defects (substitutional vacancies, see chapter 4).

In chapter 6, two kinetic databases of the atomic mobilities of the Ti-Al-V ternary system are built. One excludes substitutional vacancies; the other is based on a refined thermodynamic database taking into account substitutional vacancies. Both databases can be applied to scientific and industrial work depending on the choice of thermodynamic database required by users.

In chapter 7, the β/α phase transformation under slow cooling is simulated by the phase-field method on the basis of parameters provided by the optimisation work in chapters 5 and 6. The mechanism of the formation of Widmanstätten α has been investigated, and results have been compared with available experimental work.

In chapter 8, the conclusions made in the present work are summarised. Some suggestions are also made concerning future work.

1.4 Publications

The following is a list of the publications made during the Ph.D. work:

1. H. Wang, N. Warnken, R.C. Reed, Thermodynamic and kinetic modelling of bcc phase in the Ti-Al-V ternary system, Materials Science and Engineering A, 528 (2010), 622-630;
2. H. Wang, N. Warnken, R.C. Reed, Thermodynamic assessment of the ordered B2 phase in the Ti-Al-Cr-V quaternary system, CALPHAD, 35 (2011), 204-208;
3. H. Wang, R.C. Reed, J.-C. Gebelin, N. Warnken, On the modelling of the point defects in ordered B2 phase of Ti-Al system: Combining CALPHAD with first-principles calculations, submitted to CALPHAD;
4. H. Wang, N. Warnken, J.-C. Gebelin, R.C. Reed, Phase-field simulation of β-α phase transformation in Ti-6Al-4V alloy, in preparation.

Chapter 2 Background

2.1 Titanium alloys

2.1.1 The metallurgy of titanium and its alloys

Pure titanium like many other metals (*e.g.* Ca, Fe, Co, Zr) exhibits an allotropic phase transformation, β (body-centred cubic crystal structure) to α (close-packed crystal structure). For titanium, the transformation temperature is 882±2°C; however the exact value depends on the purity of the metal, due to the great influence of interstitial and substitutional elements. Information concerning the crystal structures has been investigated very intensively and can be found in many references.

The hexagonal unit cell of the alpha-Ti phase is shown in Fig. 1; the room temperature values of the lattice parameters are a=0.295nm and c=0.468nm [10]. Thus the c/a ratio for pure alpha titanium can be calculated to be 1.587. This value is smaller than the ideal ratio of 1.633 for the hcp crystal structure. There are three most densely packed types of lattice planes as shown in Fig. 1 – (0002), $(10\bar{1}0)$, and $(10\bar{1}\bar{1})$. The three planes are also called the basal plane, prismatic planes, and pyramidal planes, respectively. The three marked a1, a2, and a3 axes are the close-packed directions, and are given the indices $<11\bar{2}0>$.

The body-centred cubic unit cell of the beta-Ti phase is shown in Fig. 2 [10]. The most densely packed plane (110) and the close-packed directions $<111>$ are also illustrated in the figure. The pure beta titanium is stable at higher temperatures than the pure alpha titanium, therefore the lattice parameter value at 900°C is given to be a=0.332nm.

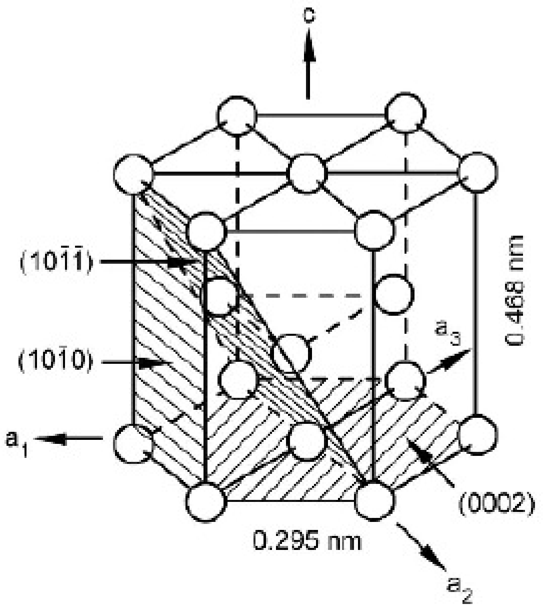

Figure 1: Unit cell of the α-Ti phase [10].

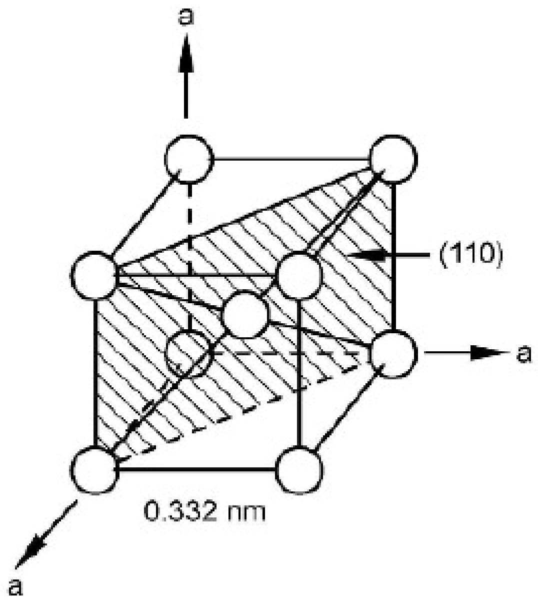

Figure 2: Unit cell of β-Ti phase [10].

There are two main ways in which the β phase at higher temperatures can transform to the α phase at lower temperatures, depending on both the cooling rate and alloy compositions – martensite (at high cooling rate) and Widmanstätten α (at fairly low cooling rate, controlled by diffusion). The crystallographic orientation relationship between the phases obeys the so-called Burgers relationship for both the martensite and the Widmanstätten processes. The Burgers relationship was proposed by Burgers [11]:

$(110)_\beta \parallel (0002)_\alpha$

$[1\bar{1}1]_\beta \parallel [11\bar{2}0]_\alpha$

This relationship was confirmed firstly for zirconium, and later also for titanium [12]. In light of this relationship, 12 hexagonal variants, having different orientations from the parent beta crystal, can be chosen for a bcc crystal.

Alloying elements in titanium are usually divided into three groups – either α or β stabilising additions or alternatively neutral, depending on their influence on the α/β transformation temperature of 882°C of pure titanium (increase, decrease, or non-change) [10]. The α stabilisers can increase the transus temperature when solute content is increased as shown in Fig. 3. This category of elements includes Al, O, N, C, B, Ga, Ge, and the rare earth elements. Al is the most frequently used alloying element; however B, Ga, Ge and the rare earth elements are not used as alloying elements due to their lower solubilities when compared to Al or O. The β stabilisers can decrease the transus temperature, and are further classified into β isomorphous elements and β eutectoid forming elements, as shown in Fig. 3. The elements V, Mo, Nb, Ta and Re are β isomorphous elements in titanium alloys. The first three (V, Mo, Nb) are more frequently used; but the other two (Ta, Re) are rarely used due to their high density. From the other group of β eutectoid forming elements, Cr, Fe, and Si are frequently used, whereas Ni, Cu, Mn, W, Pd, and Bi are very limited used, and Co, Ag, Au, Pt, Be, Pb, and U are not used at all. The last group of elements which includes Zr, Hf and Sn, behaves more or less neutrally (Fig. 3) since they have only a slight effect on the α/β transformation temperature: decrease with small additions and increase with higher concentrations[10].

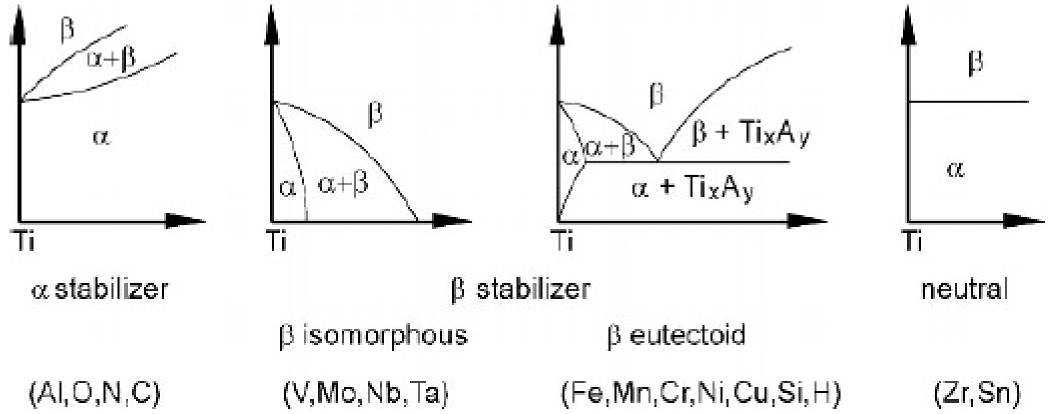

Figure 3: Effect of alloying elements on phase diagrams of titanium alloys (schematically) [10].

2.1.2 Commercial titanium alloys

Since the end of the Second World War, titanium and titanium alloys have been of increasing interest. The research and usage of titanium based alloys is widespread, increasing particularly since 1950 when it was realised that the addition of Al improves the strength of the alloy. A major breakthrough was the appearance of the still commonly used alloy Ti-6Al-4V in the USA in 1954, and the introduction of the alloy Ti-4Al-4Mo-2Sn-0.5Si in the UK [10].

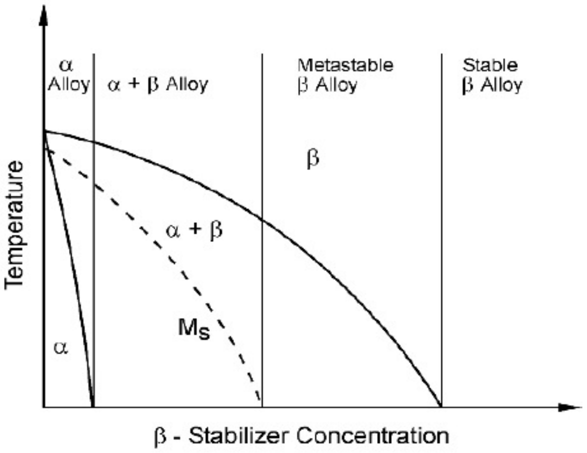

Figure 4: Pseudo-binary section through a β isomorphous phase diagram (schematically) [10]. Different types of titanium alloys are classified according to their position in the section. The dashed line refers to martinsite transformation line.

Some of the most important commercial alloys are listed in Table 1, which provides for each alloy the common name, the alloy composition, and the temperature of beta transus [10]. Three families of titanium alloys used commercially are identified depending on their position in a pseudo-binary section through a beta isomorphous phase diagram, schematically shown in Fig. 4 [10]. In the first category, the so-called α alloys include two types of alloys – commercially pure titanium and the 'real' α alloys. The commercially pure titanium is not really 'pure' as some alloying elements are present in some concentrations, according to the grade. The 'real' α alloys are those alloys which contain only small amount of the β phase (2-5 vol%) after annealing well below the corresponding beta transus. The β phase in the 'real' α alloys is often stabilised by Fe. The second group consists of the α+β alloys because of their range in the phase diagram (Fig. 4); the alloys located between the α/α+β phase boundary and the intersection of the Ms-line with room temperature belong to the α+β alloy. The last category of alloy – the β alloys – are in fact metastable β alloys since the location of those alloys in the phase diagram is still within the α+β phase field. However, the expression 'β alloy' is still employed because those 'real' β alloys within the β single phase region are not yet used widely for commercial applications.

Table 1: Selected important commercial titanium alloys [10].

Common Name	Alloy Composition (wt.%)	T_β (°C)
	α Alloys and Commercially Pure Titanium	
Grade 1	CP-Ti (0.2Fe, 0.18O)	890
Grade 2	CP-Ti (0.3Fe, 0.35O)	915
Ti-5-2.5	Ti-5Al-2.5Sn	1040
	α+β Alloys	
Ti-6242	Ti-6Al-2Sn-4Zr-2Mo-0.1Si	995
Ti-6-4	Ti-6Al-4V (0.20O)	995
	β Alloys	
Ti-6246	Ti-6Al-2Sn-4Zr-6Mo	940
Ti-15-3	Ti-15V-3Cr-3Al-3Sn	760
B120VCA	Ti-13V-11Cr-3Al	700

2.1.3 Applications

Titanium alloys is frequently used in many fields, *e.g.* aerospace applications, automotive production medical applications, and so forth. The main area of application for aerospace is in the gas turbine engine, since titanium is the standard engine material besides nickel. In the first jet engines introduced at the beginning of the 1950s, titanium alloys were included [10]. The content of titanium alloys has steadily increased in different applications, however recently a trend of replacement titanium alloys by composites has occurred [13]. Nevertheless, the requirement of titanium alloys is likely to keep increasing in the foreseen future.

2.2 B2 ordering in bcc phase

2.2.1 Order and disorder

Solid solutions of metals are usually of two types: interstitial and substitutional. For substitutional solid solutions, the atoms are randomly located on the crystal lattice. In a number of alloys with stoichiometric compositions and experimentally observed at sufficiently low temperatures, the atoms of each species are positioned at a certain site in the crystal lattice; an alloy in such an arrangement of atoms is termed ordered [14]. With increasing temperature, a portion of the atoms are found to transfer from their sites to foreign sites making an alloy partially ordered. As the temperature increases up to the melting point, the concentration of atoms on different kinds of sites becomes more identical so that the alloy becomes more disordered. The order-disorder phase transition temperature (the critical temperature) is defined as the temperature at which such a transition occurs; this changes as a function of the alloy composition since the order-disorder phase transition also occurs in alloys with non-stoichiometric compositions.

The completely ordered alloy shows similar translational crystalline symmetry with the pure metals which is unlikely to happen in a disordered alloy. Yet it presents the possibility of the occupation of different sites by different species of atoms, even when the ordering is not complete. There are two kinds of order-disorder transition, during which the symmetry will be changed. A first-order phase transition occurs when the probability of site occupation changes discontinuously at the transition point, while a second-order phase transition can arise if such a probability changes continuously [14]. From absolute zero to the ordering temperature, a finite degree of ordering can be achieved, which can be described by the occupation probabilities (η) of the element (i) within the two sublattices *I* and *II* [15]:

$$\eta_i = x_i^{II} - x_i^{I} \qquad \textbf{(1)}$$

One of the best known ordering reactions is in beta-brass. As shown in Fig. 5, atoms of one component of this alloy (A or B) are randomly positioned over all sites of the lattice, which is the state of disorder [15]. On the other hand, when the alloy is ordered, atoms of different types are distributed with unequal probability on different sites. Taking A atoms for example, they mainly occupy the sites at the corners of the cubic unit cells, and the remaining are predominantly located at B atoms. At exact stoichiometry, the alloy AB will be in a completely ordered state, and all the centres of the cell are occupied by atoms of one type (A) and all corners by the other type (B). Also, the state remains unchanged if atoms of two types exchange their locations – A at corners and B at centres. There are some ordered alloys, such as CuZn, CuBe, CuPd, AgMg, FeAl, AuZn, FeCo, NiAl etc, for which the stoichiometry is almost exact; sometimes the ordering remains to temperatures approaching and beyond the melting temperature, *e.g.* AuZn [14].

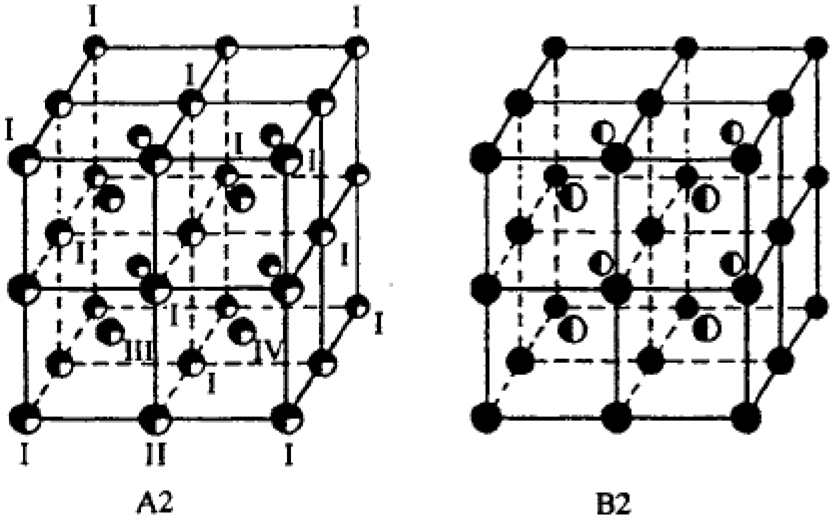

Figure 5: Relative occupation of sublattices for the A2 and B2 variants of a basic body-centred cubic arrangement [15]. In the A2 structure, all sites are occupied by the atoms randomly; in the B2 structure, positions at the centre and the corner are occupied by different types of atoms.

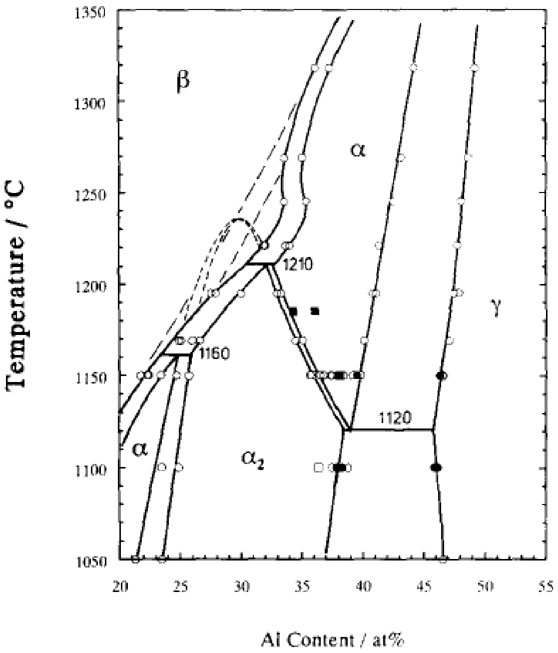

Figure 6: An unusual bending down of the β/α phase boundaries in the Ti-Al binary system [16].

2.2.2 A2-B2 transformation in the Ti-Al and Al-Cr binary systems

The A2-B2 transformation is one the most controversial equilibria in the Ti-Al binary system. The possibility of B2-type ordering in this system was first raised by Kainuma *et* *al.* [16]. An unusual bending down of the β/α boundary was found between the temperature ranges of 1150-1250°C, see Fig. 6. This phenomenon is improbable unless a special physical effect is occurring [17], which was attributed to be A2-B2 transformation in the bcc phase. This kind of ordering was later supported by DSC work on the Ti-32.6at.%Al alloy [18] as shown in Fig. 7.

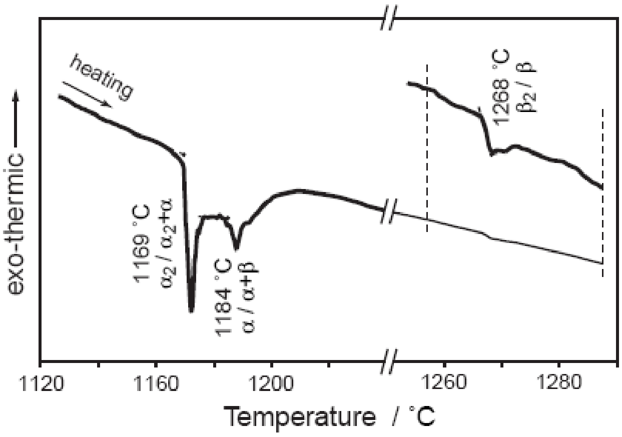

Figure 7: DSC result of the Ti-32.6at.%Al sample [18].

The B2 structure was also detected using the XRD method in the Al-Cr system [19]. The XRD patterns of alloys containing 58.4-64.8at.%Al, quenched from 885°C and 905°C, showed peaks which are consistent with the B2 phase. Although a region of B2 ordering is established, it is of little importance for the Al-Cr binary system itself because it is such a small region, as pointed out by the authors. Nevertheless, it may have much influence on higher-ordered systems based on Al-Cr system, taking Fe-Al-Cr, Ni-Al-Cr and Ti-Al-Cr for example.

2.2.3 A2-B2 transformation in Ti-Al-X (X=V,Cr) ternary systems

Much research has been done on the Ti-Al-X systems (X=Nb [20-22], V [23-26], Ta [22], Cr [27-30], Fe [28], Ru [31], Mo [22]) which supports further the possibility of the order-disorder transformation occurring in the Ti-Al binary system.

In the Ti-Al-V system, for example, the ordered B2 phase was observed in samples quenched from 1200°C by transmission electron microscopy, for which the selected area diffraction patterns of some samples are shown in Fig. 8. Also, the ordering temperature was found to decrease with increasing V content, whereas the opposite effect was observed with the addition of Al. The long-period superlattice structure of B2 phase was investigated [26], generated by periodic arrangements of anti-phase domain boundaries between every four B2 cells along the <100>B2 directions. And the effective A2 to B2 transformation temperature was found to be lower with higher cooling rates [24].

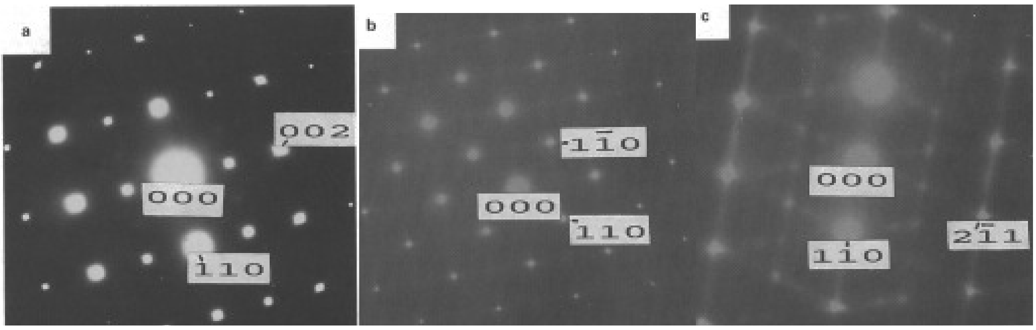

Figure 8: Selected area diffraction patterns for a: <110> b: <001> c: <113> [26].

In the other ternary system with B2 ordering, the Ti-Al-Cr system, the B2 phase was first detected by Kimura *et al.* [27] using X-ray diffraction. Many reliable results were obtained at 800°C and 1000°C by combined examination using optical microscopy, scanning electron microscopy, X-ray diffraction and energy dispersive spectroscopy [29, 30]. Another method called the Singular Point Method was later applied in the Ti-Al-Cr system [28]. This method is theoretically based on the difference in interdiffusivity between the ordered and disordered phases. A diffusion couple of Ti-30Al-20Cr / Ti-10Al-10Cr (in at.%) was annealed at 1000°C for 10h, and a clear singularity in the concentration profiles of Al and Cr was observed. This singularity in the concentration-penetration profile indicates a drastic change in the interdiffusivity of components, at which critical A2/B2 ordering boundary is located.

2.2.4 A2-B2 transformation in Ti-Al-Cr-V quaternary system

The A2-B2 transformation was also found within certain composition ranges in the quaternary system Ti-Al-Cr-V [9, 32]. In these studies, optical microscopy and scanning electron microscopy were employed to generate micrographs of microstructure, and energy dispersive spectroscopy was used to determine the phase compositions. Transmission electron microscopy was introduced to detect the crystal structure and dislocation pairs, and neutron diffraction results were the final confirmation of the conclusions. The research results are listed in Table 2. No super-lattice reflections were found in electron diffraction patterns or in X-ray spectra for samples without Al. However, the matrices of the Ti-37V-15Cr-6.6Al (wt.%) and Ti32V-15Cr-5.6Al (wt.%) alloys were detected to be the ordered B2 phase *via* the superlattice diffraction maxima.

The dislocations in four samples of different Al content were later investigated using transmission electron microscopy. In the lowest Al content alloy (2wt.%), the dislocations were relatively randomly distributed and there was no obvious pairing of dislocations; however, it was very clear that the dislocations were arranged as loosely coupled pairs in the 3wt.%Al, 4wt.%Al and 5.6wt.%Al samples. All these dislocation arrays suggested that only at 2wt.%Al was the alloy truly disordered and that for all other Al contents the alloys possessed a significant amount of long range order so that the dislocations remain coupled. Therefore there are strong suggestions that Al alloying can transform the disordered A2 phase into the ordered B2 phase and that only with concentrations less than 2wt.%Al are the alloys truly disordered.

Table 2: Experimental result through various methods on B2 ordering transformation in Ti-Al-Cr-V quaternary system [9, 32].

Methods / Compositions	in situ transmission electron microscopy (super lattice)	neutron diffraction (peak)	transmission electron microscopy (dislocation couple)
Ti-25V-15Cr	No	No	Relatively random
Ti-30V-15Cr	No	No	Relatively random
Ti-30V-15Cr-1Al	No	No	Relatively random
Ti-25V-15Cr-2Al	No	No	Relatively random
Ti-30V-15Cr-2Al	No	No	Relatively random
Ti-25V-15Cr-3Al	No	No	Loosely coupled
Ti-25V-15Cr-4Al	No	Humps	Loosely coupled
Ti-30V-15Cr-4Al	No	Humps	Loosely coupled
Ti-21V-15Cr-3.8Al	No	Humps	Loosely coupled
Ti-27V-15Cr-4.7Al	Weak	Broad	Coupled
Ti-32V-15Cr-5.6Al	Strong	Large	Coupled
Ti-37V-15Cr-6.6Al	Strong	Large	Coupled

Furthermore, the B2 ordering temperature of Ti-32V-15Cr-5.6Al (wt.%) alloy was determined to be 620°C. The atom locations were also obtained by channelling electron microscopy, which indicates that Al takes V sites, while Cr substitutes for Ti. It was later pointed out that further work is still required using calorimetry, which would perhaps be the most sensitive method for detecting ordering [33].

2.3 CALPHAD approach

2.3.1 Basic ideas

CALPHAD, is abbreviation for CALculation of PHAse Diagrams, and is known in academia as an approach for establishing self-consistent descriptions of phase diagrams, as well as thermodynamic properties. CALPHAD (Computer Coupling of Phase Diagrams and Thermochemistry) and Journal of Phase Equilibria and Diffusion (previously called Journal of Phase Equilibria before 2004 and Bulletin of Alloy Phase Diagrams before 1980) are two major journals publishing the scientific progress of phase diagrams in various fields and systems, such as assessment, experimental determination, thermodynamic calculation, new technology and so forth.

Larry Kaufman first described the approach of CALPHAD in the book Computer Calculations of Phase Diagrams [34], where the important concept of ‘lattice stability’ [35] was introduced. Saunders & Miodownik [15] wrote a comprehensive guide to the CALPHAD method in 1998, which is the first one to integrate many aspects of CALPHAD as a whole. Later in 2007, a book named Computational thermodynamics: CALPHAD was published by Lucas *et al.* [1] including more practical information on the CALPHAD approach. Spencer [36] recently published a brief history of CALPHAD.

Gibbs-energy models were applied to the calculations of phase diagrams by van Laar and many others [37, 38]. The most common way involves finding the minimum value of the Gibbs energy G for constant values of temperature T, pressure p, and mole fraction of component(s) x or weight fraction of component(s) w or site fraction of component(s) y. Thus the Gibbs energy G is obtained as a function of these conditions. Several minima-compatible values of the Gibbs energy may be calculated under these conditions, of which the most negative value of G is called the 'global minimum' and corresponds to the 'stable equilibrium'; the rest are 'local minima' corresponding to 'metastable equilibria' [1]. Thus the phase diagram can be obtained numerically by computing the global minimum Gibbs energy under series of conditions. It is very clear that searching the 'global minimum' is of the utmost importance to the calculation of the phase diagrams.

Thermodynamic models are of importance in order to calculate the Gibbs energy under different situations. In general, the total Gibbs energy of a phase is expressed as [1]

$$G = G^{\mathrm{srf}} + G^{\mathrm{phys}} + G^{\mathrm{id}} + G^{\mathrm{ex}} \qquad \mathbf{(2)}$$

The superscripts 'srf', 'phys', 'id', and 'ex' stand for 'surface of reference', 'physical', 'ideal', and 'excess', respectively. The first term G^{srf} is often called the reference state, which represents the Gibbs energy due to an unreacted mixture of the constituents. The second term G^{phys} is the Gibbs energy induced by a physical model involving, for example, magnetic transitions. This part of the Gibbs energy is not taken into account in the present work. The third term G^{id} represents the contribution of ideal mixing, which is based on the configurational entropy. The last term G^{ex} is the excess Gibbs energy, which represents the rest contribution to the Gibbs energy other than the first three terms. The partitioning for the Gibbs energy indicates the models are not established on the basis of the physical origins of the Gibbs energy, except G^{phys}; configurational as well as vibrational, electronic, and other contributions to the Gibbs energy will be included within those Gibbs energy terms [1].

2.3.2 CALPHAD procedures

The procedures of the CALPHAD method usually consist of three distinct stages - the assessment of the available experimental or theoretically calculated data, the choice of models for the phases, and the optimisation of the thermodynamic parameters.

First of all, various types of data are required at the beginning of the optimisation work, including all the information concerning thermodynamic properties, phase equilibria, and crystal structure. These data could come from experiments, theoretical calculation, review papers, and also previous optimisations, and are used for different purposes during the optimisation. For example, the information of crystal structure plays a key role in the model selection; experimental data of phase equilibria and thermodynamic properties are considered as the validation of the optimisation results; results from first-principles calculations make it possible to compare with some hypothetical properties. The critical assessment of these data is one of the most important procedures here, as it decides the accuracy of the optimisation work. In most cases, the data are consistent with each other, while occasionally some different sets of information for the same quantity may be contradictory. Those data are required to be given different weights in the optimisation.

Generally speaking, there are some common ways to judge, *i.e.* when and how they were obtained. In the worst case, some data may be abandoned or used to compare with the results only, and not taken into account during the optimisation.

As each phase in the investigated system should be assessed independently, one specific model will be chosen for each phase; it could be the same model for two or more phases with the same structure. Here, the thermodynamic models for the ordered B2 phase need be mentioned. The phases of the A2 and B2 phases were first treated as one phase [39] using a two sublattice model. This is different from the model for other solution phases: only one sublattice excluding interstitial vacancy. This treatment was successfully used in the Ni-Al system, but then met severe difficulties during the extrapolation to higher systems, like Ni-Al-Nb. The problem lies in the incompatible models for the disordered A2 phase in three constitutional binary systems. The A2 phase in both Ni-Nb and Al-Nb systems has been conventionally modelled as $(Nb,Ni)_1$ and $(Al,Nb)_1$, respectively. However, the A2 phase in Ni-Al system was obviously $(Al,Ni)_{0.5}$:$(Al,Ni)_{0.5}$, consistent with the ordered B2 phase. Under such situation, it was impossible to combine these two models together, so that extrapolation cannot be achieved. To overcome this limitation, the authors [40] later proposed another model for the ordered B2 phase, separated but dependent on the disordered A2 phase. The idea was to add the contribution of ordering to the disordered phase so that the model for the A2 phase can be kept the same as for the other A2 phases. This will be discussed in the later chapters.

Optimising the parameters contained in each model is sometimes semi-empirical, and can be divided into two steps: first is to gain a set of parameters that can reproduce approximately the main features of the most reliable experimental data; the second step is fine-tuning the parameters to the selected data after self-assessment. The optimisation is always carried out by using appropriate software, like Thermo-Calc [41], Pandat [42], BINGSS [43] , ChemSage [44] and so on. It often obeys the rule that the optimisation should be from the constitutional subsystems to higher order system (binary – ternary – quaternary – ……).

2.3.3 Applications

Since the development of the CALPHAD approach, there has been an increasing drive to apply the phase diagram information obtained from the relative calculations into practical processes. Many significant examples can be found in the journals mentioned previously. Extrapolation to higher order systems with more elements is one of the features of CALPHAD, due to its provision of information where otherwise only educated guesses could be used. Taking the design of lead-free solders for example, some important qualities of the candidates have been predicted using CALPHAD, such as the melting point and so forth. Major progress in the application of phase diagram information has been made in the implementation of such calculations in casting simulation software [45]. Thermodynamic calculation of the phase equilibria of a multicomponent alloy was also interfaced with a micromodel for computing the change of fraction solid and temperature, given a specified change in enthalpy during the liquid-solid transformation [45]. This coupling was incorporated into a finite element modelling package developed for the solidification of castings; the simulation was carried out for a step wedge part and a Ni-15Al-2Ta (wt.%) alloy [46].

2.3.4 The direct coupling of thermodynamics and kinetics

From the beginning, the main area of the direct coupling of thermodynamics and kinetics has been used for constructing transformation diagrams in steels [47-49]. Only some simple formalism has been considered in the Gibbs energy models for the solution phases, which have usually been in the dilute solution range of phases such as austenite and ferrite [50-53]. Good results have been demonstrated with the models, and these have been extensively applied to low to medium alloyed steels. Limitation lies in their use for only low concentrations of substitutional elements, although quite complex carbides have been taken into account [54].

Until the end of last century, the more generally applicable concentrated solution models have not been used because they lead to an increase in computational time which is necessary to calculate equilibria with the more complex models, and the lack of good assessments using more generally applicable concentrated solution models [15]. Later on, kinetic modelling in multi-component alloys [55] can be carried out in the the DICTRA software program [41]. The necessary thermodynamic input during the course of kinetic modelling can be provided by the Thermo-Calc software program [41]. This method of direct coupling of thermodynamics and kinetics has demonstrated the advantages of producing a more generalised approach to phase transformations [15].

2.4 First-principles calculations

2.4.1 General ideas

Nowadays, classical molecular dynamics has become a very sophisticated tool to investigate many-body condensed matter systems. The reign of classical molecular dynamics and electronic structure methods was extended greatly by a family of techniques that is referred to here as ‘first-principles’; other names that are currently in use for such methods are for instance *ab* initio molecular dynamics, on-the-fly, direct, extended Lagrangian, density functional, quantum chemical, Hellmann-Feynman, Fock-matrix, potential-free, or just quantum molecular dynamics amongst others [56].

The basic principle underlying all first-principles calculations methods is to describe the forces acting on the nuclei using electronic structure calculations. The parameters required by classic molecular dynamics include predefined potentials, force fields, either based on empirical data or on independent electronic structure calculations. Traditionally the route followed in molecular dynamics is determining the potentials in advance, in which the full interaction is typically broken up into two-body and many-body contributions, long-range and short-range terms, electrostatic and non-electrostatic interactions, and so on [56].

After decades of intense research, very elaborate interaction models, including the nontrivial aspects of representing these potentials analytically, were devised [57-61]. In spite of their overwhelming success, the need to devise a fixed predefined potential implies serious drawbacks: among the most significant are systems in which (i) too many parameters represent different interatomic interactions due to different atom or molecule types and/or (ii) ‘chemically complex’ - the electronic structure and the chemical bonding pattern changing qualitatively in the simulations; (iii) changing a single species provokes typically enormous efforts to parameterise the new potentials if a specific system is understood after elaborate development of satisfactory potentials, [62, 63]. As a result, systematic studies are a *tour de force* if no suitable set of consistent potentials is already available [56].

2.4.2 Basic definitions

In first-principles calculations, some important basic definitions need be introduced.

(i) Supercell. A unit cell serves as representative unit for a periodically repeated system, such as a crystalline structure [64]. First-principles calculations are usually carried out within several unit cells, which are taken as a supercell.

(ii) Plane wave basis. Plane wave is one of the basis sets for the expansion of the valence orbitals, charge densities and potentials. Several immediate advantages of using a plane wave basis have been described by Hafner [65].

(iii) Cutoffs and **k**-points. In practice the Brillouin zone has to be approximated by a finite sum over a set of **k**-points [56]. There are several schemes available to choose the integration points systematically, including the most efficient ‘special **k**-point’ [66-68]. The plane wave (energy) cutoff E_{cut} is an arbitrary maximum value of energy in order to determine the precision of the calculation.

(iv) Pseudopotentials. The core electrons are replaced by pseudopotentials in order to minimise the size of the plane wave basis which is necessary for calculations involving many atoms. The pseudopotentials represent the long-range interactions of the core correctly, and avoid an explicit treatment of the strongly bound and chemically inert core electrons [65].

2.4.3 Calculation of the energy

The total energy E_{tot} is required to be one of the preconditions of molecular dynamics calculations with interaction potentials derived from density functional theory. It can be calculated as a sum of different individual terms including kinetic E_{kin}, external (local pseudopotential $E_{\mathrm{loc}}^{\mathrm{PP}}$, and nonlocal pseudopotential $E_{\mathrm{nloc}}^{\mathrm{PP}}$), exchange E_{XC} and correlation, and electrostatic energy E_{ES}, *via*

$$E_{\mathrm{tot}} = E_{\mathrm{kin}} + E_{\mathrm{loc}}^{\mathrm{PP}} + E_{\mathrm{nloc}}^{\mathrm{PP}} + E_{\mathrm{XC}} + E_{\mathrm{ES}} \quad \textbf{(3)}$$

where each energy term will be discussed in the next chapter.

2.4.4 Applications

Applications of first-principles calculations are particularly widespread in physics, chemistry, and more recently also in biology, for example, crystal structure and phase stability [69, 70], mechanical properties [71-73], dynamical properties [74, 75], liquids and amorphous materials [76], magnetism and magnetic nanostructures [77], semiconductors and insulators [78], surfaces, interfaces and thin films [79], adsorption, chemical reaction, and catalysis [80, 81].

2.5 Phase-field simulation

2.5.1 General idea

The phase-field method has recently emerged as a powerful tool for modelling and predicting mesoscale morphological and microstructure evolution in materials [82], which can be coupled with the fundamental thermodynamic and kinetic information. The phase-field method employs a function of position and time ϕ which is called the phase-field variable, to express which phase the material is, liquid or solid – no gas phase is under consideration. This variable can be used to describe interfaces between liquid and solid, or between solids. The change of the phase-field variable is smooth but highly localised between fixed values that represent solid(s) and liquid [83]. Therefore location of an interface is treated as part of the unknown solution, and applying boundary conditions at the interface can be avoided by employing the phase-field method [83].

To model solidification of a single-phase material, a number of approximations are needed to employ the phase-field variable to describe the liquid-solid transition. One possible physical interpretation of the phase-field variable is given by Mikheev & Chernov [84], as shown in Fig. 9. The interfacial region is represented by a damped wave, and also its motion during solidification can be seen. The wave itself depicts the probability of finding an atom at a particular location. Details can also be found in the reference by Boettinger *et al.* [83].

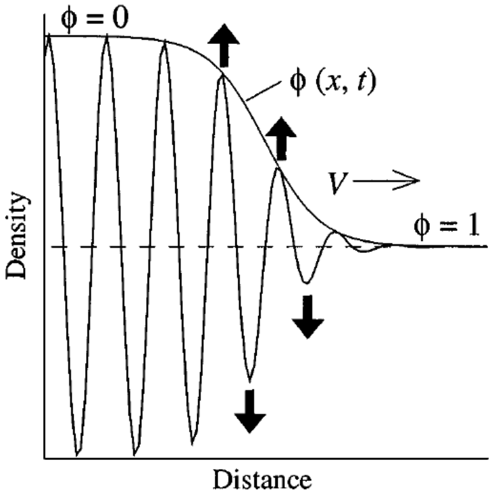

Figure 9: Schematic representation of a possible physical interpretation of the phase-field variable ϕ [84]. The phase-field variable ϕ is a function of distance x and time t.

2.5.2 Phase-field models

Phase-field models can be divided into various related categories: those in which a single scalar order parameter, or multiple order parameters, are used; those derived from a thermodynamic formulation, or from geometrical arguments; those best suited for large, or small, deviations from local equilibrium; those dealing with physical problems where the order parameter can easily, or not easily, be associated with a measurable quantity [83]. Usually the phase-field method itself reflects real physics while in some cases it should be considered only as a mere simulation.

Characteristics of the phase-field models have been summarised by Steinbach [85]: the principal one is the diffuseness of the interface between the two phases (diffuse interface models); the other one is that non-equilibrium states are addressed in general. This view of a ‘diffuse interface’ was first proposed by Van Der Waals [86], who stated that a diffuse interface is more natural than the assumption of a sharp interface from general thermodynamic considerations. As mentioned previously, the interface is described by the continuous transition of phase field variable ϕ between the two phases (see Fig. 9). Additionally, the phase-field variable is treated as an independent state variable, which means it distinguishes between different states of a material that may be identical in all other state variables [85].

Here some phase-field models are summarised. Ginzburg & Landau [87] used the independent phase-field variable (order parameter) to expand the thermodynamic state functions and their gradients in the phase transitions. Spinodal decomposition was investigated using a (discrete) field variable in space and time by Hillert [88]. Also for the spinodal decomposition, the continuous variable and the alloy concentration were taken into account by Cahn & Hilliard [89, 90]. In order to obtain an appropriate value for the thickness of the interface, a pragmatic view was adopted, that the scale of the diffuseness of the phase field is below the microstructure scale of interest by Steinbach [85].

2.5.3 Multi-phase-field method

The so-called multi-phase-field model was first developed in order to solve the problem in which there are an arbitrary number of different phases or different grains with distinct orientations of the same phase [91, 92]. Fan & Chen [93, 94] later proposed a similar model to the multi-phase-field model, and Kobayashi & Warren [95] also developed a model where the grain orientation is treated as an order parameter to allow simulation of diverse situations, *e.g.* solidification, grain rotation and grain growth in a multi-grain structure. The free energy F of the bulk Ω is generally described by separating different physical phenomena, interfacial, chemical and elastic energy [85], consistent with

$$F = \int_{\Omega} f^{\text{intf}} + f^{\text{chem}} + f^{\text{elast}} \quad \textbf{(4)}$$

Based on the above multi-phase-field concept, MICRESS (MICRostructure Evolution Simulation Software) [96] has been developed since 1995. This software enables the calculation of microstructure formation in time and space during phase transformations, which can be used especially in metallurgical systems.

2.5.4 Applications

As a mature method dealing with nearly realistic cases, the phase-field approach has attracted more and more attention by both scientific groups and industrial users. Recently, it has been applied to diverse applications including solidification [97], as well as complex solid phase transformations, [98, 99] with dislocations and so forth being considered (dislocation-solute interactions, dislocation dynamics) [82]. The development of this method and the relative software or codes is being carried out and the calculation will take into account more factors and parameters in the future.

Chapter 3 Methodology

3.1 Introduction

Nowadays, modelling has become a very efficient method for use in both academic and industrial fields. In the present work, several modelling methods have been used, *e.g.* CALPHAD (Section 2.3), First-Principles (Section 2.4), and Phase-field (Section 2.5). As these modelling methods concern different length scales, a framework is necessary, under which the simulations can be carried out. The framework of the present work will be described in this chapter. Also the models and simulation procedures used in each method are to be considered.

3.2 The framework of multi-scale modelling

Fig. 10 illustrates the framework of the multi-scale modelling employed within the present work. The core of the work is concerned with thermodynamic modelling. One main objective concerns the optimisation of a thermodynamic database for phase diagram calculation using the CALPHAD approach, with particular focus on the ordered B2 phase in the Ti-Al-Cr-V alloy. This procedure consists of three main steps: (i) the assessment of the available experimental or theoretical information, (ii) the selection of the corresponding thermodynamic model for each phase, and (iii) the optimisation of the set of thermodynamic parameters.

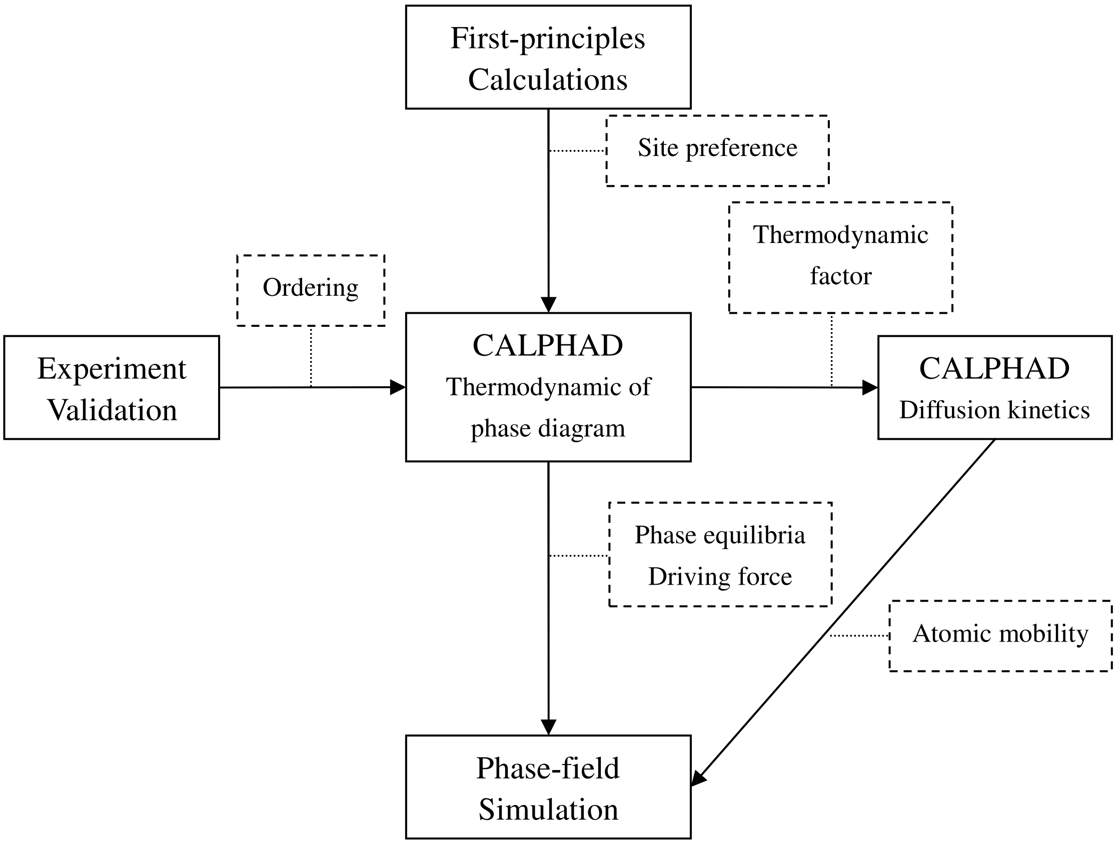

Figure 10: The framework of the multi-scale modelling of the present work.

In order to obtain a better thermodynamic model of the ordered B2 phase reflecting the proper physical principles, first-principles calculations are carried out to provide information concerning the tendency of the site occupation by point defects. In the Ti-Al binary system, the calculation concerns particularly the pressure of the anti-site defects or the substitutional vacancies. Although other useful information can be produced by first-principles calculations, such as heats of formation, heats of transformation, elastic and magnetic properties [100], the present work requires particularly the structural energy as input to the thermodynamic calculations needed for the CALPHAD method.

After obtaining a trial thermodynamic database, experimental validation is ideally required to confirm its accuracy. Since the occurrence of B2-type ordering in the Ti-Al binary system lacks strong experimental support, two samples for which compositions fall into the predicted single phase region were examined using transmission electron microscopy. Also, the effect of ordering on the kinetics of α precipitation from β matrix in the Ti-Al-Cr-V quaternary system is to be investigated using differential scanning calorimetry.

Still within the concept of CALPHAD methodology, the kinetic database of diffusion in the Ti-Al-V ternary system is optimised, making use of thermodynamic factors from the thermodynamic database. This part of the work is of much interest and importance because of its key role as one of the pre-conditions for many other modelling methods, as well as its application in processing, *e.g.* casting, welding, coating and so on.

As a meaningful extension of the CALPHAD calculations, quantitative simulations of microstructure evolution in Ti-6Al-4V are then carried out, using calculations from the CALPHAD approach such as phase equilibrium, driving force and atomic mobility. The aim is to provide clues concerning the mechanism of the formation of the Widmanstätten α microstructure.

Each sub-model in the framework provides necessary information which is needed for the present work. First-principles calculations indicate 'WHAT is the proper thermodynamic model reflecting reality'; the thermodynamic modelling answers 'WHICH is the stable phase(s) at certain temperature and composition fields'; the kinetic optimisation deals with 'HOW fast the atoms diffuse'; and the phase-field simulation investigates ‘WHEN and WHERE should be the phase, grain, or interface from under certain conditions’. By integrating those sub-models appropriately, multi-scale modelling becomes a powerful tool.

3.3 Modelling methods

3.3.1 Thermodynamic models

A solid solution model is used for the bcc and hcp phases $(\mathrm{Al,Cr,Ti,V,Va})_1$. As defined in Section 2.3.1, the Gibbs energies are expressed by

$$G = G^{\mathrm{srf}} + G^{\mathrm{phys}} + G^{\mathrm{id}} + G^{\mathrm{ex}} \tag{5}$$

The first term, representing an unreacted mixture of the constituents of the phase, is calculated in the present work by

$$G^{\mathrm{srf}} = \sum_i x_i {}^{\circ}G_i \tag{6}$$

where x_i is the mole fraction of the species i (i=Al,Cr,Ti,V,Va); ${}^{\circ}G_i$ stands for the lattice stability, and the generally accepted values are taken from Dinsdale [101]. The second term in Eq. (5) is neglected here as no physical effect like a magnetic transition is under consideration. The third term of the configurational entropy is expressed as

$$G^{\mathrm{id}} = RT\sum_i x_i \ln x_i \tag{7}$$

and the last one is the excess Gibbs energy determined by the Redlich-Kister polynomial [102]

$$G^{\mathrm{ex}} = \sum_i \sum_{j>i} x_i x_j \sum_{\nu} (x_i - x_j)^{\nu}\, {}^{\nu}L_{ij} + \sum_i \sum_{j>i} \sum_{k>j} x_i x_j x_k L_{ijk} \tag{8}$$

in which L are the ν-th order interaction parameters between i and j or among elements i, j

and *k* (*i*,*j*,*k*=Al,Cr,Ti,V,Va); these parameters are optimised in the present work. Note the quaternary parameters are not used as their contribution to the Gibbs energy can be considered small.

The thermodynamic model for the ordered α_2 phase is $(\mathrm{Al,Cr,Ti,V})_{0.75}$:$(\mathrm{Al,Cr,Ti,V})_{0.25}$. The form of the Gibbs energy is as given in Eq. (5), but the descriptions of the three terms are different from those in Eqs. (6-8). The compound energy formalism [103] is used, as described in Hillert & Staffanson [104]. The method is based on an analytical expression for the Gibbs energy using terms of increasing powers of the site fractions (*y*), consistent with

$$G^{\mathrm{srf}} = \sum_i \sum_j y_i^1 y_j^2 \, {}^{\circ}G_{i:j} \tag{9}$$

$$G^{\mathrm{id}} = RT\left(\frac{3}{4}\sum_i y_i^1 \ln y_i^1 + \frac{1}{4}\sum_j y_j^2 \ln y_j^2\right) \tag{10}$$

$$G^{\mathrm{ex}} = \sum_i \sum_{j>i} \sum_k y_i^1 y_j^1 y_k^2 L_{i,j:k} + \sum_i \sum_{j>i} \sum_k y_k^1 y_i^2 y_j^2 L_{k:i,j} + \sum_i y_i^1 y_j^1 y_k^1 y_i^2 L_{i,j,k:i} + \sum_i y_i^1 y_i^2 y_j^2 y_k^2 L_{i:i,j,k} \tag{11}$$

where ${}^{\circ}G_{i:j}$ are the mole Gibbs energies of hypothetical end-member compounds; the site fraction *y* are the mole fractions of atoms within the individual sublattices; the superscripts of the site fractions (y^1, y^2) refer to the first or the second sublattice, respectively; *L* are interaction parameters optimised in the present work; *i,j,k* represent Al, Cr, Ti, V or Va.

A two-sublattice thermodynamic model for the ordered B2 (β_2) phase is given as $(\mathrm{Al,Cr,Ti,V,Va})_{0.5}$:$(\mathrm{Al,Cr,Ti,V,Va})_{0.5}$. The mole Gibbs energy is described by the method proposed by Dupin & Ansara [40], in which the Gibbs energy of the ordered B2 phase is obtained by adding the contribution of ordering to the Gibbs energy of the disordered A2 (β) phase, so that

$$G^{\mathrm{B2}} = G^{\mathrm{A2}} + G^{\mathrm{ord}}(y_i^1, y_i^2) - G^{\mathrm{ord}}(x_i, x_i) \tag{12}$$

where G^{A2} is the Gibbs energy of the disordered A2 phase; the difference between the latter two terms is the Gibbs energy due to ordering which needs to be accounted for, and can be calculated using the compound energy formalism [103]. When $y_i^1 = y_i^2 = x_i$, Eq. (12) corresponds to the disordered energy and $G^{\mathrm{B2}} = G^{\mathrm{A2}}$.

3.3.2 Models for diffusivity

For the crystalline phases, the ternary interdiffusion coefficient matrix is arrived at by choosing one element to be dependent on the other two [105], thus

$$D_{kj}^{n} = \sum_i (\delta_{ik} - x_k) x_i M_i \left(\frac{\partial \mu_i}{\partial x_j} - \frac{\partial \mu_i}{\partial x_n} \right) \tag{13}$$

where n, k, j are the dependent, the diffusing and the gradient element, respectively. The terms x_i, μ_i, and M_i are the mole fraction, chemical potential and mobility of element i, respectively. The term δ_{ik} is the Kronecker delta ($\delta_{ik} = 1$ if $i = k$, otherwise $\delta_{ik} = 0$).

3.3.3 Models for atomic mobility

According to Jonsson [106], the atomic mobility in a multicomponent phase can be expressed by

$$M_B = M_B^{\circ} \exp\left(-\frac{Q_B}{RT} \right) \frac{1}{RT} \tag{14}$$

where M_B° is the frequency factor and Q_B is the activation enthalpy. The frequency factor is calculated by

$$M^{\circ}_{B} = \exp(\Theta_{B}) \tag{15}$$

Both Θ_B and Q_B depend in the general case on the composition, temperature and pressure. In the spirit of the CALPHAD approach [34], the dependence on composition of $\Phi_B(\Theta_B$ or Q_B) is described with a Redlich-Kister polynomial according to

$$\Phi_{B} = \sum_{i} x_{i}\Phi^{i}_{B} + \sum_{i}\sum_{j>i} x_{i}x_{j}\left[\sum_{r=0}^{m} {}^{r}\Phi^{i,j}_{B}[x_{i}-x_{j}]^{r}\right] + \sum_{i}\sum_{j>i}\sum_{k>j} x_{i}x_{j}x_{k}\left[\sum_{s} v^{s}_{ijk}\, {}^{s}\Phi^{i,j,k}_{B}\right] \tag{16}$$

where the parameters are obtained by

$$v^{s}_{ijk} = x_{s} + \frac{1-x_{i}-x_{j}-x_{k}}{3} \tag{17}$$

3.3.4 Models for first-principles calculations

As described in Section 2.4.3, the total energy of the bulk E_{tot} is calculated by Eq. (3), so that $E_{\mathrm{tot}} = E_{\mathrm{kin}} + E^{\mathrm{PP}}_{\mathrm{loc}} + E^{\mathrm{PP}}_{\mathrm{nloc}} + E_{\mathrm{XC}} + E_{\mathrm{ES}}$. Each term in this equation can be calculated by

$$E_{\mathrm{kin}} = \sum_{\mathbf{k}} \omega_{\mathbf{k}} \sum_{i}\sum_{\mathbf{G}} \frac{1}{2} f_{i}(\mathbf{k})\left|\mathbf{G}+\mathbf{k}\right|^{2}\left|c_{i}(\mathbf{G},\mathbf{k})\right|^{2} \tag{18}$$

$$E^{\mathrm{PP}}_{\mathrm{loc}} = \sum_{I}\sum_{\mathbf{G}} \Delta V^{\mathrm{loc}}_{I}(\mathbf{G}) S_{I}(\mathbf{G}) n^{*}(\mathbf{G}) \tag{19}$$

$$E^{\mathrm{PP}}_{\mathrm{nloc}} = \sum_{\mathbf{k}} \omega_{\mathbf{k}} \sum_{i} f_{i}(\mathbf{k}) \sum_{I}\sum_{\alpha,\beta\in I} (F^{\alpha}_{I,i}(\mathbf{k}))^{*}\, \omega^{I}_{\alpha\beta} F^{\beta}_{I,i}(\mathbf{k}) \tag{20}$$

$$E_{\mathrm{XC}} = \Omega \sum_{\mathbf{G}} \varepsilon_{\mathrm{XC}}(\mathbf{G}) n^{*}(\mathbf{G}) \tag{21}$$

$$E_{\mathrm{ES}} = 2\pi\Omega \sum_{\mathbf{G}\neq 0} \frac{\left|n_{\mathrm{tot}}(\mathbf{G})\right|^{2}}{G^{2}} + E_{\mathrm{ovrl}} - E_{\mathrm{self}} \tag{22}$$

where E_{kin}, $E^{\mathrm{PP}}_{\mathrm{loc}}$, $E^{\mathrm{PP}}_{\mathrm{nloc}}$, E_{XC} and E_{ES} are kinetic energy, external energy (local pseudopotential), external energy (nonlocal pseudopotential), exchange and correlation energy, and electrostatic energy, respectively; the term **k** refers to **k**-points; $\omega_{\mathbf{k}}$ are the weights of the integration **k**-points; the function *f* represents the plane wave function; *i* and *I* refer to electrons and nuclei, respectively; **G** are the reciprocal space vectors; *c* are complex numbers; ΔV^{loc} is the local potential; S_I are the structure factors; the function *n* refers to charge density function; the superscript * denotes orthonormalisation; the function *F* refers to the overlap between the projectors of the nonlocal pseudopotential and the Kohn-Sham orbitals; Ω is the volume of the unit cell; the $\varepsilon_{\mathrm{XC}}$ function is the combined exchange-correlation function; E_{self} and E_{ovrl} are the electrostatic energies induced by the nucleus itself and other nuclei, respectively (for details, see [56]).

3.3.5 Multi-phase-field model

The so-called multi-phase-field model [85, 92, 107] which is implemented in the MICRESS [96] software was applied in the present work to the simulation of microstructure evolution in the Ti-6Al-4V alloy. The multi-phase-field equations are described as [108]

$$\dot{\phi}_\alpha = -\sum_{\beta=1,\ldots,N} \frac{\pi^2}{8\eta N} \mu_{\alpha\beta} \left(\frac{\delta F}{\delta \phi_\alpha} - \frac{\delta F}{\delta \phi_\beta} \right) \tag{23}$$

where η, $\mu_{\alpha\beta}$, and *N* represent the interface width treated to be equal everywhere, the interfacial mobility for each pair of phases, and the local number of phases, respectively.

The diffusion equations for a multicomponent system can be given as [109]

$$\dot{c}^i = \nabla \left(\sum_{\alpha=1}^{N} \phi_\alpha M_\alpha^{ij} \nabla \frac{\delta F}{\delta c_\alpha^j} \right) = \nabla \left(\sum_{\alpha=1}^{N} \phi_\alpha D_\alpha^{ij} \nabla c_\alpha^j \right) \tag{24}$$

where D_{α}^{ij} is the matrix of diffusion coefficients.

The principle of Gibbs energy minimisation is used to derive the phase-field ϕ_{α}(0-1) and concentration c^i of component *i* of a multicomponent material. Two constraints apply, consistent with

$$\sum_{\alpha=1,\dots,N}\phi_{\alpha}=1 \tag{25}$$

$$\sum_{\alpha=1,\dots,N}\phi_{\alpha}c_{\alpha}^{i}=c^{i} \tag{26}$$

As described in Eq. (4), the global free energy *F* is integrated from two parts – the interfacial energy density f^{intf} and the chemical energy density f^{chem} (the elastic energy f^{elast} is not taken into account in the present work), so that

$$F=\int_{\Omega}f^{\mathrm{intf}}+f^{\mathrm{chem}} \tag{27}$$

in which the two terms are expanded in the phase-field variables, consistent with

$$f^{\mathrm{intf}}=\sum_{\alpha,\beta=1,\dots,N,\alpha\beta}\frac{4\sigma_{\alpha\beta}}{\eta_{\alpha\beta}}\left(-\frac{\eta_{\alpha\beta}^{2}}{\pi^{2}}\nabla\phi_{\alpha}\cdot\nabla\phi_{\beta}+\phi_{\alpha}\phi_{\beta}\right) \tag{28}$$

$$f^{\mathrm{chem}}=\sum_{\alpha=1,\dots,N}\phi_{\alpha}f_{\alpha}\vec{c}_{\alpha}+\tilde{\mu}^{i}\left(\vec{c}-\sum_{\alpha=1,\dots,N}\phi_{\alpha}c_{\alpha}^{i}\right) \tag{29}$$

where $\sigma_{\alpha\beta}$ is the interfacial energy between α phase and β phase, and the term $\vec{c}_{\alpha}$ indicates the independence of the bulk free energy f_{α} on the phase concentrations c_{α}^{i}. The chemical potential $\tilde{\mu}^{i}$ of the component *i* can be estimated from the chemical free energy density *g* and the phase concentration c^i [92], consistent with

$$\tilde{\mu}^{i}=\frac{\partial g}{\partial c^{i}} \tag{30}$$

3.4 Simulation procedure

3.4.1 Thermodynamic optimisation

In order to obtain a thermodynamic database for the Ti-Al-Cr-V quaternary system using the CALPHAD method, the following routes are followed: (i) collecting the information concerning the lattice stability of the four elements, Ti, Al, Cr, V; (ii) optimising the binary thermodynamic parameters for the six binary systems, Ti-Al, Ti-Cr, Ti-V, Al-Cr, Al-V, Cr-V; (iii) extrapolating to the four ternary systems, Ti-Al-V, Ti-Al-Cr, Ti-Cr-V, Al-Cr-V; (iv) optimising the ternary thermodynamic parameters for the three ternary system; (v) extrapolating to the quaternary system, Ti-Al-Cr-V. This route is illustrated in Fig. 11. It should be pointed out that the optimisation of a ternary system is not always straightforward, because the ternary database greatly depends on the three constitutional binary systems. Take the Ti-Al-V ternary system for example; in order to derive an appropriate database for this system, high qualities are needed for the databases of the three binary systems (Ti-Al, Ti-V, and Al-V).

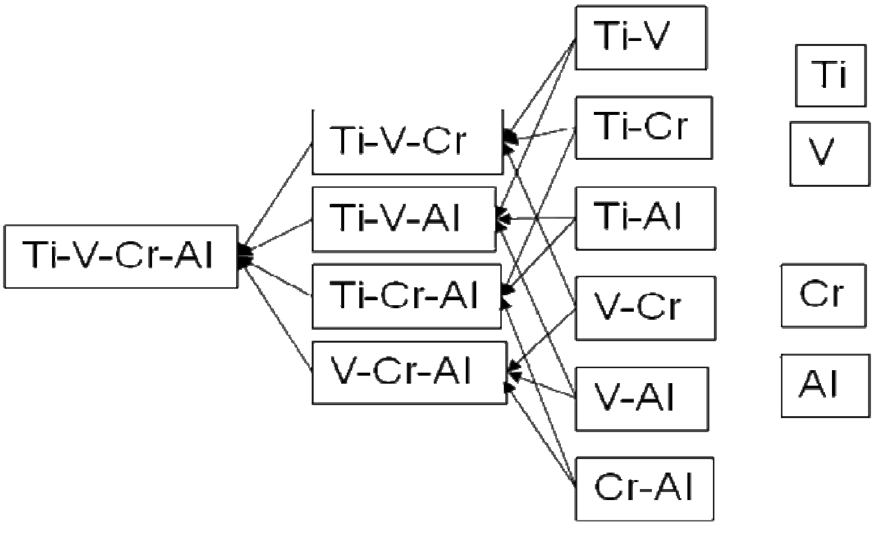

Figure 11: Illustration of the extrapolation to the Ti-Al-Cr-V quaternary system.

The optimisation of the B2 phase in the Ti-Al binary system is taken as an example to illustrate the optimisation procedures. Optimisations of the other systems follow in a similar way. The thermodynamic parameters were optimised in the Parrot engine of the Thermo-Calc software package [41]. The parameters needed for the phases in the binary Ti-Al system were placed into the TDB file which stores the database. The assessed experimental data for the two peritectoid reactions were input into the POP file for validation of the calculated results. The error range of the temperature of the peritectoid reactions was taken to be 10°C, and that of the composition of each phase (except the B2 phase) 1at.%. The PAR file was set in the Parrot engine of Thermo-Calc for the procedure of optimisation. Each parameter was given an initial value. The experimental data were compiled and given weights according to the assessment in the ED_EXP module, a sub-module of Parrot module. The parameters were optimised by trial/error and the least square method once again until the calculated values of the selected data were within the error range of the experimental values.

3.4.2 Atomic mobility optimisation

The ternary parameters in the mobility database of Ti-Al-V system were optimised in Parrot engine of the DICTRA software package [41]. Needed for the optimisation, the thermodynamic database of the bcc phase was appended first to allow estimation of the thermodynamic factor. The procedure is similar to the thermodynamic optimisation, following the familiar routes of CALPHAD. The parameters were also placed into the

TDB file. The interdiffusion coefficients were input into the POP file, and taken as experimental criteria. An error range of 2% was given. The PAR file was created for the optimisation process. The parameters were again optimised using the Parrot module. The optimised parameters were then used to reproduce the concentration profiles and the diffusion paths in the DIC module.

3.4.3 First-principles calculations

The energies of various sorts of point defects were calculated using a supercell approach, in which one defect was placed in a large supercell (54 atoms). The calculations were performed by the pseudopotential method [110] in the VASP software [65], where the potpaw_GGA pseudopotentials were used. The valence configurations used for Ti are 4s3d, and those for Al are 3s3p. All the atoms were fully relaxed to the equilibrium positions. The other settings included plane-wave energy cutoff (450eV), k-point meshes for Brillouin zone (10×10×10) and spin polarization. The site occupation of point defects in the Ti-Al binary system was assessed by using the complex defect formation energy, following [111].

3.4.4 Phase-field simulation

The phase-field simulations were performed to simulate the phase transformation of β to α during the slow cooling in Ti-6Al-4V, using multi-phase-field model implemented in the MICRESS software [96]. A driving file was constructed containing those parameters of the system under analysis and also those to be optimised such as interfacial mobility, interfacial energy and so on. The output files were visualised using the DP_MICRESS function, and compared with the experiments. Once a satisfactory fit with experiments was found, analysis of the mechanism of the microstructure evolution was undertaken. Details are given in chapter 7.

3.5 Experimental method

In order to elucidate the effect of Al on the ordering reactions in the high strength, high toughness titanium alloys, a number of (1 kg bulk) ingots with compositions of Ti-25V-15Cr-xAl (x=0,2,4,6,8 in weight percent) were cast, and then forged at 1050°C to improve their homogeneity, building on the work of Li *et al.* [9]. Differential scanning calorimetry analysis was carried out using a Netzsch DSC404 calorimeter to determine the temperatures of all the phase transformations from room temperature to 1000°C. The measurements were performed under a flow of high purity argon gas. A Pt-Rh crucible was used as the container, and the samples were placed inside it on a thin foil of tungsten to prevent any chemical reaction between the crucible and the specimen. Heating and cooling rates of 10°C/min were employed.

As a validation of the thermodynamic modelling, not only the above DSC experiments were considered, but also some samples of the Ti-Al binary system and the Ti-Al-V ternary were examined using transmission electron microscopy. Three ingots for which the compositions within the single B2 phase region predicted (Ti-23Al, Ti-20Al and

Ti-10Al-35V in wt%) were obtained using an arc melting furnace. The binary and ternary samples were heat treated at 1200°C and 800°C respectively for 5 hours, followed by quenching in iced water. Some slices of the annealed samples were cut using electro discharge machining. These samples were then prepared for transmission electron microscopy by electrochemical thinning in the solution which consisted of 5vol.% of perchlonic acid, 35vol.% of butanol, and 65vol.% of Methanol. Transmission electron microscopy was carried out on a Jeol 2100 transmission electron microscope.

3.6 Summary

In this chapter, the modelling and experimental methods used in the present work are summarised. Firstly the framework of multi-scale modelling has been given, followed by all the models used in the thermodynamics, atomic mobilities, first-principle calculations and the phase-field simulation. The simulation procedures in diverse modelling methods have been discussed. Finally the experimental validation of the thermodynamic database has been described.

Chapter 4 First-principles calculations on point defects

4.1 Introduction

Nowadays, first-principles calculations are a common way to provide the CALPHAD method with important data concerning crystal structure, thermodynamic properties, and so forth. In this chapter, first-principles calculations are employed before the thermodynamic optimisation of the Ti-Al system in order to obtain some useful information. The results of first-principles calculations are used as pre-conditions for the phase diagram calculations.

In recent thermodynamic descriptions of the Ti-Al binary system, the B2 phase is modelled using either a two-sublattice model $(\mathrm{Al,Ti})_{0.5}:(\mathrm{Al,Ti})_{0.5}$, or a three-sublattice one $(\mathrm{Al,Ti})_{0.5}:(\mathrm{Al,Ti})_{0.5}:\mathrm{Va}_3$ which takes into account anti-site defects only [18, 112]. This treatment differs from a previously proposed thermodynamic model for the B2 phase $(\mathrm{Al,Ni,Va})_{0.5}:(\mathrm{Al,Ni,Va})_{0.5}$ in the Ni-Al binary system, which considers both anti-site defects and substitutional vacancies [40]. Since the thermodynamic model for the B2 phase should reflect sound physical principles, it is necessary to re-consider the model of the B2 phase on the basis of its known crystal defect structure.

Experimental studies of point defects in the B2 phase in the Ti-Al systems are hampered by the fact that bcc phase is not stable on the Al-rich side of the system. First-principles calculations are one way to overcome this limitation and to provide useful hints about the substitutional vacancy. Of course, results are limited, as calculation can only be done for the ground state. In order to overcome this limitation Hagen & Finnis [111] developed a method to study the point defects in the ordered alloys at finite temperatures which was then successfully applied to the B2 phase in the Ni-Al system. This same method was used in the present work to calculate the concentration of different point defects located in different sites, the results of which were used to improve the thermodynamic model in the CALPHAD assessment of the Ti-Al binary system.

4.2 The site preference of point defects in B2 TiAl alloy

In order to calculate the energies of formation of different point defects, and thus to determine the thermodynamic model for the ordered B2 phase, the total energy E_{pure} of the perfectly stoichiometric TiAl was calculated first (a 3×3×3×2 super cell is used). After that the deviation from stoichiometry was taken into account by introducing four different point defects - one vacancy in Ti sublattice of energy E_{VaTi}, one Al atom in Ti sublattice E_{AlTi}, one vacancy in Al site E_{VaAl}, and one Ti atom in Al site E_{TiAl}. All calculations were performed in the ground state, *i.e.*, at zero temperature (T=0) and zero pressure (p=0). With these energies, it is still not possible to determine the preference of any sort of point defect, since it is not appropriate to simply compare the difference between the cases of substitutional vacancy and anti-site defect. As can be seen in Fig. 12, the total numbers of atoms in these two cases are not the same; therefore the total energy in the case with more atoms is lower, which indicates greater stability. In order to overcome this shortcoming, the enthalpies of formation of the point defects are calculated by using the rescaled total energies.

Defining H_{ik} (note: in this work the subscript ik represents atom/vacancy i=Al,Ti,Va in sublattice k=Al,Ti) as the enthalpy of formation of an alloy with respect to the energy of the standard states of the pure components (per atom), e_{TiTi} and e_{AlAl} (hcp Ti and fcc Al) can be written,

$$\begin{aligned}
H_{\mathrm{VaAl}} &= (E_{\mathrm{VaAl}} - 27e_{\mathrm{TiTi}} - 26e_{\mathrm{AlAl}})/53 \\
H_{\mathrm{TiAl}} &= (E_{\mathrm{TiAl}} - 28e_{\mathrm{TiTi}} - 26e_{\mathrm{AlAl}})/54 \\
H_{\mathrm{VaTi}} &= (E_{\mathrm{VaTi}} - 26e_{\mathrm{TiTi}} - 27e_{\mathrm{AlAl}})/53 \\
H_{\mathrm{AlTi}} &= (E_{\mathrm{AlTi}} - 26e_{\mathrm{TiTi}} - 28e_{\mathrm{AlAl}})/54 \\
H_{\mathrm{pure}} &= (E_{\mathrm{pure}} - 27e_{\mathrm{TiTi}} - 27e_{\mathrm{AlAl}})/54
\end{aligned} \qquad \textbf{(31)}$$

Table 3: The calculated enthalpy of formation of the B2-TiAl compared to various sources.

Formation energy of the B2-TiAl (kJ/mol)	Sources
-26.9	Present work
-26.1	[113]
-28.0	[113]
-25.1	[114]
-25.9	[115]
-39.4	[116]
-37.2	[18]

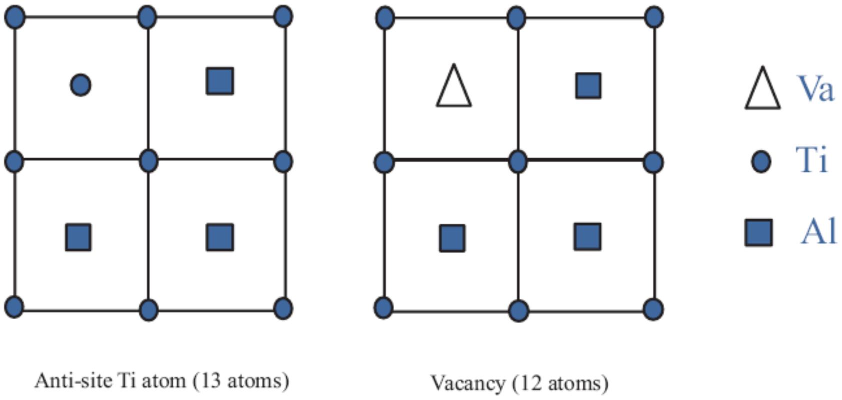

Figure 12: The comparison between two kinds of point defects.

The calculated enthalpy of formation of the B2-TiAl is listed in Table 3 compared to various sources. In Fig. 13, the calculated enthalpies of formation of the five compounds given above are plotted as four different branches. The point defects are sufficiently dilute in the calculations thus the enthalpies of formation of the alloys scale linearly with the atomic concentrations of the point defects (note: the concentrations in the present work refer to concentrations per site, or site fraction). These four branches can be divided into two sets, one on each side of the perfect stoichiometric composition, corresponding to substitutional alloys containing anti-site defects and structural vacancies respectively. Point defects with lower enthalpy of formation are unambiguously more stable. Thus for Ti-rich alloys, the anti-site Ti defect is more stable than the vacancy, while in Al-rich alloy, the vacancy on the Ti sublattice is slightly more stable than the anti-site Al defect. This indicates that the preferred type of point defect is different on the Ti and Al side of the stoichiometric composition, with antisite atoms on the Ti-rich side and vacancies on the Al-rich rich side. Some calculated enthalpies of formation are given in Table 4, such as those of isolated point defects, complex concentration-conserving defects and interbranch excitation. For this purpose, the following expressions have been employed,

$$
\begin{aligned}
H^{F}_{\mathrm{VaAl}} &= 53\cdot(H_{\mathrm{VaAl}} - H_{\mathrm{pure}}) \\
H^{F}_{\mathrm{TiAl}} &= 54\cdot(H_{\mathrm{TiAl}} - H_{\mathrm{pure}}) \\
H^{F}_{\mathrm{VaTi}} &= 53\cdot(H_{\mathrm{VaTi}} - H_{\mathrm{pure}}) \\
H^{F}_{\mathrm{AlTi}} &= 54\cdot(H_{\mathrm{AlTi}} - H_{\mathrm{pure}})
\end{aligned}
\qquad \textbf{(32)}
$$

It is also noteworthy that since the enthalpy of formation of the interbranch Al defect is small, a competition between triple and interbranch Al defects on the Al-rich side can be expected (this enthalpy of formation is also affected by the calculation errors and atoms relaxations). Nevertheless, considering the present calculations, constitutional vacancies need be taken into account in the CALPHAD optimisations; this is confirmed by predicting concentrations of the constitutional defects which follows.

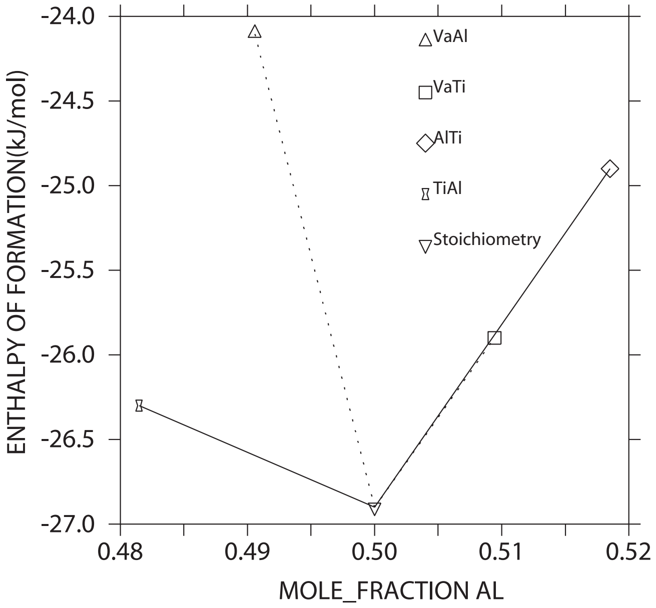

Figure 13: The enthalpies of formation of five alloys.

Table 4: The enthalpies of formation of isolated defects, complex concentration-conserving defects, and interbranch excitations in TiAl.

Name	Designation or quasichemical reaction	H_{ik}^{F} / eV
	Intrinsic point defects	
Ti in Al	TiAl	0.38
Vacancy in Al	VaAl	1.54
Al in Ti	AlTi	1.15
Vacancy in Ti	VaTi	0.55
	Concentration-conserving defect complexes	
Triple Ti (TT)	0→2VaTi+TiAl	1.49
Divacancy (DV)	0→VaAl+VaTi	2.10
Volume (E)	0→TiAl+AlTi	1.53
Triple Al (TA)	0→2VaAl+AlTi	4.23
	Interbranch excitation	
Interbranch Ti	TiA→2VaAl	2.70
Interbranch Al	2VaTi→AlTi	0.04

4.3 Vacancies at finite temperature

In this section, the concentrations of substitutional vacancies at finite temperatures are evaluated. The concentrations of point defects are determined by using the results of first-principles calculations.

A linear relationship between the enthalpy of formation of an alloy H_{ik} and the concentrations of the point defects x_{ik} (i=Al,Ti,Va, k=Al,Ti) consistent with,

$$H_{ik} = E_{\text{pure}} + \sum_i \sum_k H_{ik}^F x_{ik} \tag{33}$$

where E_{pure} corresponds to the total energy of an alloy without point defects, and H_{ik}^F (i=Al,Ti,Va, k=Al,Ti) is the enthalpy of formation of one point defect, either anti-site defect or substitutional vacancy. In order to introduce temperature dependency, entropy needs to be taken into account; for the sake of simplicity only configurational entropy of the alloy is considered, such that

$$S = k\left((1 + x_{Va})\ln\left(\frac{1 + x_{Va}}{2}\right) - \sum_i \sum_k x_{ik} \ln x_{ik} \right) \tag{34}$$

Note that phonon calculations (vibrational entropy) can affect the calculations of vacancy concentrations, especially at elevated temperatures; but it is beyond the present work because the calculated results will only illustrate roughly the defect concentrations compared to each other, and the phonon calculations do not have any influence on the site preference (major objective of this chapter). The equilibrium concentrations of the point defects are then calculated by combining minimisation of the Gibbs free energy with mass-balance constraints, consistent with

$$\begin{aligned}
&x_{\mathrm{AlAl}} + x_{\mathrm{TiAl}} + x_{\mathrm{VaAl}} = 1 \\
&x_{\mathrm{TiTi}} + x_{\mathrm{AlTi}} + x_{\mathrm{VaTi}} = 1 \\
&x_{\mathrm{AlAl}} + x_{\mathrm{AlTi}} = x_{\mathrm{Al}} \\
&x_{\mathrm{TiTi}} + x_{\mathrm{TiAl}} = x_{\mathrm{Ti}}
\end{aligned} \qquad \mathbf{(35)}$$

where x_{Al} and x_{Ti} are the total mole fractions of Al and Ti in the alloy, respectively. An analytical solution of this model, as derived in the references [111, 117], is used in the present work. This yields the concentrations of point defects as functions of alloy composition and temperature.

The predicted concentrations of various point defects at 627°C are plotted against the mole fraction of Al in Fig. 14. It becomes clear that substitutional vacancies are the major point defects on the Al-rich side. On the Ti-rich side the major point defects are anti-site Ti atoms, but the concentration of substitutional vacancies on the Ti sublattice is still relatively high. Higher concentrations of vacancies can be expected at higher temperatures than 627°C. The high concentration of substitutional vacancies is consistent with the experimental results, which indicates that ordering raises the vacancy concentration [7, 8]. These results also illustrate the importance of including substitutional vacancies into the thermodynamic model for the B2 phase.

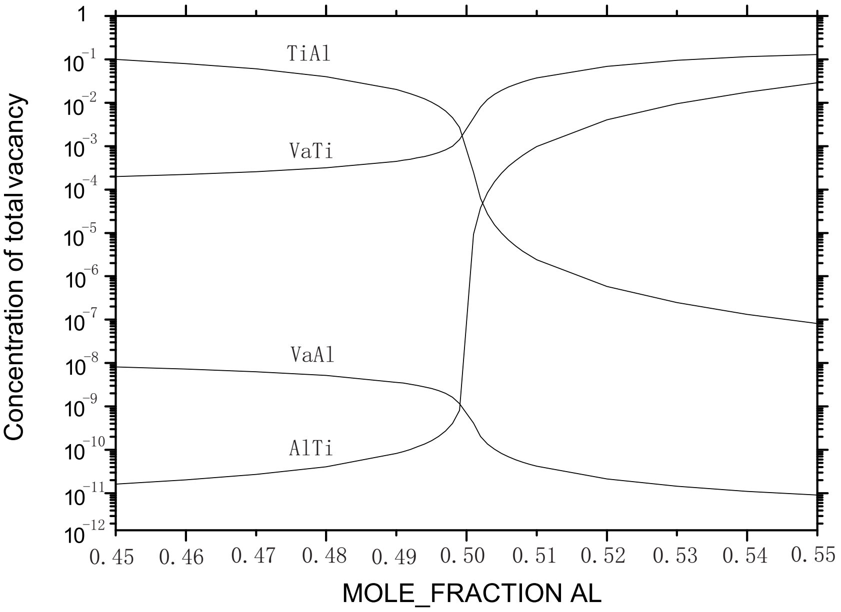

Figure 14: The calculated concentrations of total point defects at 627°C: Ti anti-site defect (TiAl), Al anti-site defect (AlTi), Ti vacancy (VaTi) and Al vacancy (VaAl).

It is also interesting to separate structural from thermal point defects. Structural point defects are induced by deviation from the exact stoichiometry. They are present at both 0K and finite temperatures, while thermal point defects are present only at finite temperatures. In the following, only the major point defects obtained in Fig. 14 are considered (anti-site Ti defects on the Al sublattice and vacancies on the Ti sublattice). The concentrations of the thermal defects x_{ik}^{t} (*i*=Al,Ti,Va, *k*=Al,Ti) can be obtained as described by Lozovoi *et al.* [117]:

$$x_{ik}^{t} = x_{ik} - x_{ik}^{0} \qquad \textbf{(36)}$$

where x_{ik} and x_{ik}^{0} (*i*=Al,Ti,Va, *k*=Al,Ti) are the concentrations of various types of point defects at finite temperature and 0K, respectively. At 0K two cases need be considered, depending on which is the dominant point defect on the sublattice under consideration:

1. anti-site defect $\quad x_{ik}^{0} = 2x_{i} - 1 \qquad$ **(37)**

2. substitutional vacancy $x_{ik}^{0} = 1-(1-x_i)/x_i$ **(38)**

in which x_i (*i*=Al,Ti,Va) is the total mole fraction of *i* atoms in the *i*-rich alloy.

The calculated concentrations of thermal defects are shown in Fig. 15. Interestingly vacancies in the Ti sublattice are the main point defects on the Ti-rich side, at an increasing concentration towards the stoichiometric composition, *i.e.* increasing Al alloy compositions. Similar behaviour is observed for anti-site Ti, but at lower defect concentrations. Above the stoichiometric composition (>50at.%Al) the concentration of Ti vacancies drops steeply and thermal Ti vacancies are absent at any higher Al compositions. Similar behaviour is also found in the Ni-Al system, where it is attributed to the interbranch Al excitation 2VaNi→AlNi (2VaTi→AlTi in the present work, see Table 4) [117]. Also the concentration of thermal vacancies on the Ti sublattice is very large. This is due to small difference of the enthalpies of formation between vacancies and anti-site Al on the Ti sublattice, and it can be affected by the calculation errors and atoms relaxations. Anti-site Al atoms are the dominant thermally-induced point defects on the Al-rich side of the stoichiometry. Anti-site Ti is predicted at similar concentration close to the stoichiometric composition, but quickly drops to much lower values at higher Al alloy compositions.

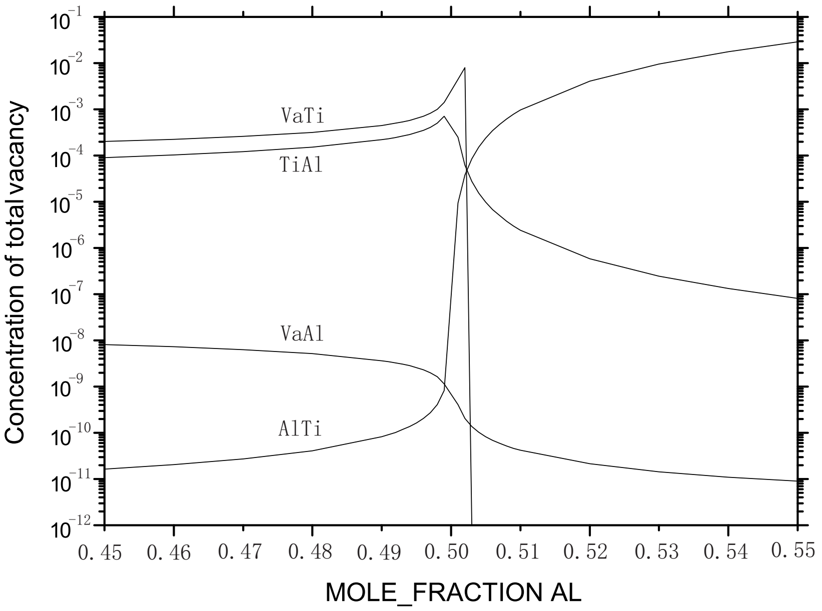

Figure 15: The calculated concentrations of thermal defects at 627°C: Ti anti-site defect (TiAl), Al anti-site defect (AlTi), Ti vacancy (VaTi) and Al vacancy (VaAl).

4.5 Summary

To summarise, the enthalpies of formation of different point defects in the B2 phase of the Ti-Al system have been calculated using first-principles calculations. A preference for point defects has been predicted: Ti anti-site defects in the Al sublattice and vacancies in the Ti sublattice. The concentrations of various types of point defects were calculated at finite temperatures using first-principles calculations. The calculations of the site preference provide valuable information which is useful for the CALPHAD assessment.

Chapter 5 Thermodynamic modelling of Ti- Al-Cr-V system

5.1 Introduction

In order to model the Ti-Al-Cr-V quaternary system, thermodynamic descriptions of the constitutional binary and ternary systems are required as a basis of extrapolation. Building a database for these six binary systems, four ternary systems and lastly the quaternary system is a huge and complicated piece of work. Fortunately, a database of parameters for the Ti-Al-Cr-V system is available from CompuTherm LLC [118], and it is this which is built upon here. However, this database lacks information concerning the ordered B2 phase. Therefore the parameters of the B2 phase need to be added to complete the database for the quaternary system, at the same time keeping the phase equilibria consistent with the known experimental information.

In light of first-principles calculations, the substitutional vacancy should in principle be present in the B2 phase, which indicates that it is necessary to make some alterations of the model of the disordered A2-bcc phase used by the database [118], from $(Al,Ti,V)_1$ to $(Al,Ti,V,Va)_1$. This change in the treatment of the A2 phase represents a significant amount of work.

Thus in the present work, two ways were used to model the phase equilibria in the system. In the first, the initial CompuTherm database was retained, so that the substitutional vacancies are excluded; the advantage of this is that the database can still be used. In the second, the substitutional vacancies are considered, but the modelling work is limited to the Ti-Al-V ternary system. In this chapter, the thermodynamic information of the Ti-Al-Cr-V system was provided *via* three main procedures: the assessment of the experimental data of phase equilibria, the chosen models for the phases, and the optimisation of the thermodynamic parameters.

5.2 Assessment of the phase equilibria

5.2.1 Binary systems

There are two binary systems involving the B2 ordering - Ti-Al and Al-Cr. One of the most widely accepted Ti-Al phase diagrams was assessed by Murray [119], which was updated twice by Okamoto [120, 121]. In this version of the phase diagram, no ordered B2 phase was suggested, and the alpha phase was stable in two regions with only a narrow ‘path’ between them (Fig. 16). It is debatable whether this very narrow regime of alpha phase is actually stable or not. Moreover, many phase boundaries were approximated as dashed lines, due to lack of experimental data. This binary system was later re-assessed by Raghavan [122], in which a region for the ordered B2 phase was included and the calculated α/β boundary had an unusual curvature in the temperature range of 1150-1250°C [16]. This kind of behaviour can only occur due to some specific physical effect, *e.g.* the order-disorder transformation [17]. Recently, two additional solid-state reactions involving the β phase were included in the phase diagram (Fig. 17) [123], namely the reactions $\beta+\alpha=\alpha_2$ at 1200±10°C and $\beta+\alpha_2=\alpha$ at 1170±10°C, taking account of the α/β boundary [16, 124]. The occurrence of these two reactions has been attributed to be the appearance of the ordered B2 phase, on account of the unusual curvature of the α/β boundaries and the small change of the slope of the calorimetry curves at these temperatures.

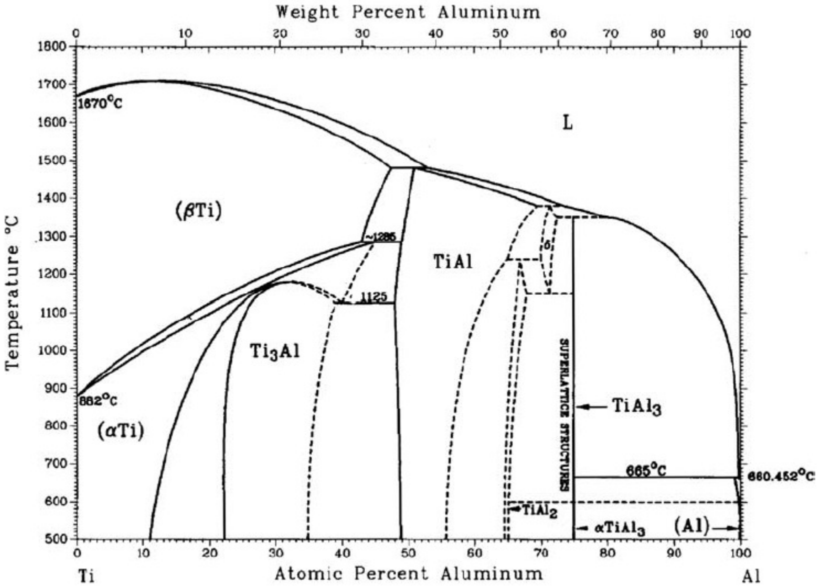

Figure 16: An assessed Ti-Al binary phase diagram [119].

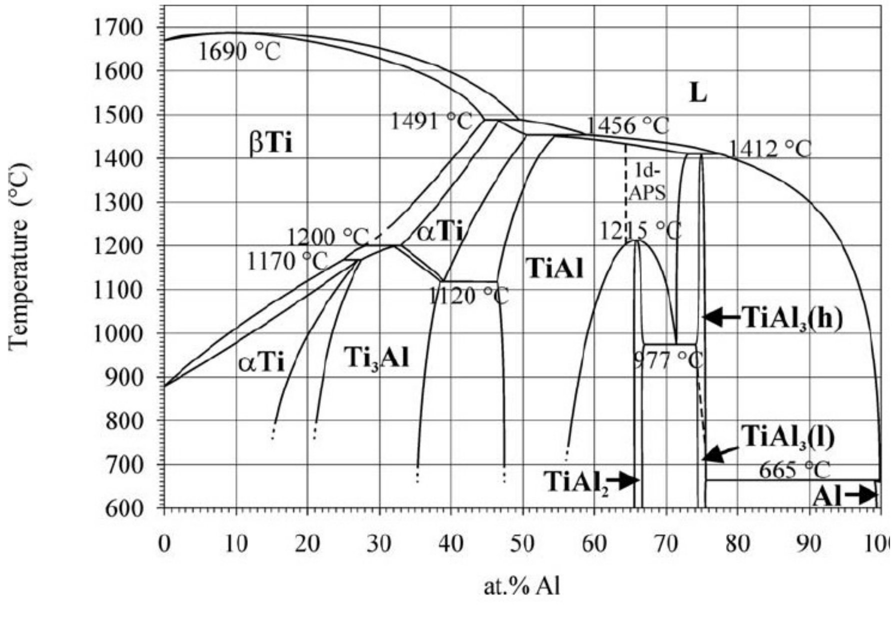

Figure 17: An assessed Ti-Al binary phase diagram [123].

The phase diagram of the Al-Cr system (Fig. 18) was presented in the assessment work by Murray [125], in which information concerning the invariant reactions were given. Yet some phase relations in the Cr-rich part were missing. In the later work by Okamoto [126], the Al-Cr system was re-assessed (Fig. 19). Some invariant reactions and the existence of some intermetallic compounds were adjusted, whilst the second-order transition involving the A2-B2 phases [19] was added into the phase diagram. The phase diagrams of the remaining binary systems are presented in Figs. 20-23, including Ti-V [127], Ti-Cr [128, 129], Cr-V [130] and Al-V [131].

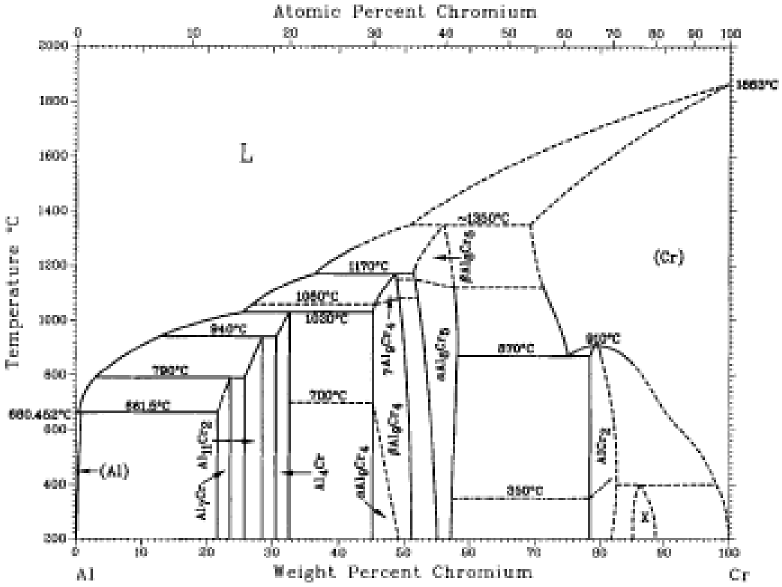

Figure 18: An assessed Al-Cr binary phase diagram [125].

5.2.2 Ternary systems

Among the four constitutional ternary systems, there has been so far no experimental information about the Al-Cr-V system. The other three have been described in the following way.

The Ti-Al-V ternary system was assessed by Hayes [132], who presented a schematic liquidus projection, a partial reaction scheme, isothermal sections at 1400°C, 1200°C, 1100°C, 1000°C and 800°C, and partial isothermal sections for Ti-rich alloys at 900°C, 800°C, 700°C and 600°C. Some more phase equilibria were updated in the recent assessment by Raghavan [133]. A schematic liquidus projection near the Al corner and two full isothermal sections at 900°C and 600°C were added, in which the ordered B2 phase found by Ahmed [23] was adopted.

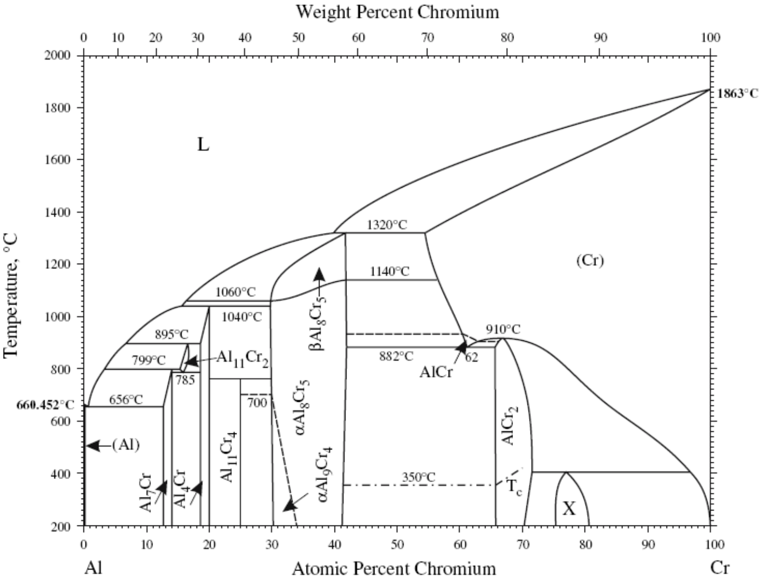

Figure 19: An assessed Al-Cr binary phase diagram [126].

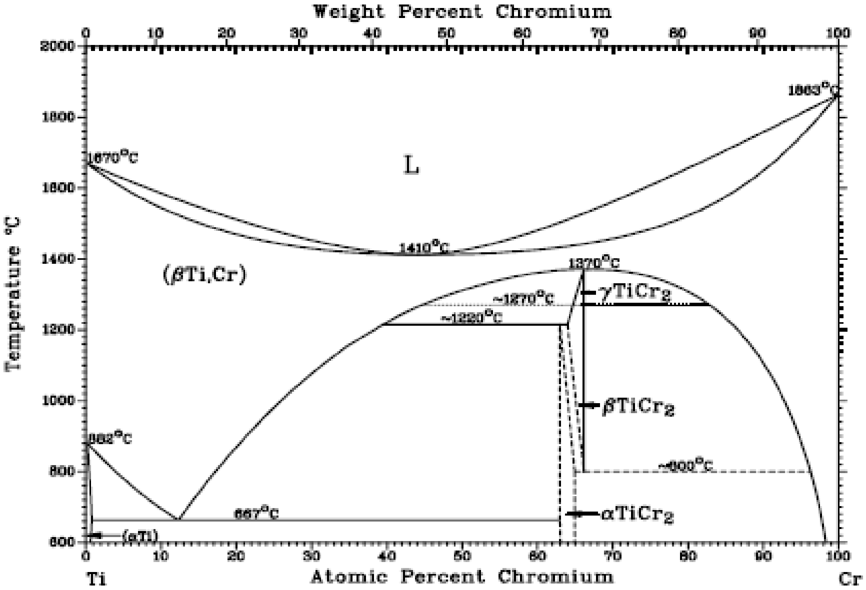

Figure 20: An assessed Ti-Cr binary phase diagram [128, 129].

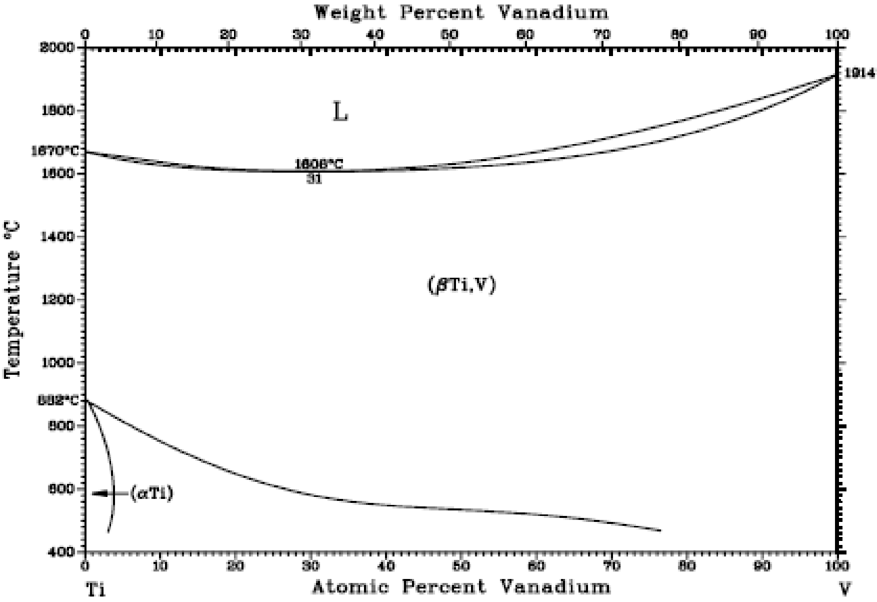

Figure 21: The assessed Ti-V binary phase diagram Ti-V [127].

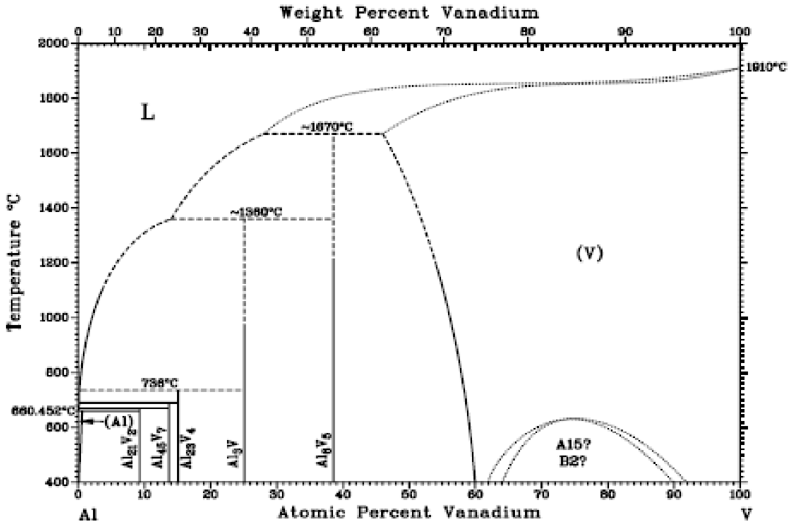

Figure 22: An assessed Al-V binary phase diagram [131].

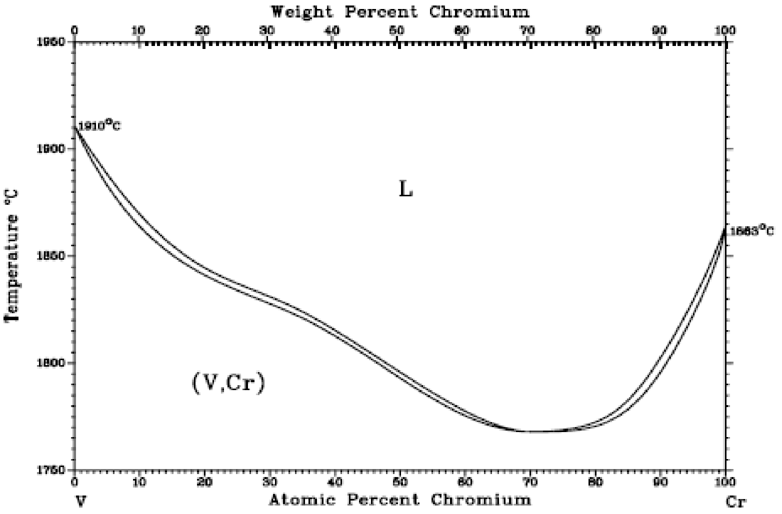

Figure 23: An assessed Cr-V binary phase diagram [130].

In the review of the Ti-Al-Cr ternary system [134], a partial reaction scheme and isothermal sections for Ti-rich alloys at 1200°C, 1100°C, 1000°C, 800°C and 600°C were published, based mainly on the results of [135]. Two full isothermal sections of much importance were included in the later assessment of Raghavan [136], which contained the phase equilibria between the ordered B2 phase and other phases, and the single phase region of the ordered B2 phase.

In the Ti-Cr-V ternary system, experiments were completed before 1970; these have been summarised by Enomoto [137]. The phase relationships at several temperatures were defined simplistically in terms of the three terminal binary systems, due to the absence of any ternary compound found in this ternary system.

5.3 Choice of models

In the first way mentioned in the Section 5.1, the thermodynamic model of the ordered B2 phase (excluding substitutional vacancies) is consistent with the formula $(Al,Cr,Ti,V)_{0.5}$:$(Al,Cr,Ti,V)_{0.5}$. The Gibbs energy of the ordered B2 phase is obtained by adding the contribution of ordering to the Gibbs energy of the disordered A2 phase, consistent with the details discussed in the Section 3.3.1.

In the second case, a much more complicated treatment is required since the model for the disordered A2 phase has been changed. In the Ti-Al-V ternary system under consideration, the formulae of the thermodynamic models of phases in the Ti-rich part are:

A2-bcc (β) $(Al,Ti,V,Va)_1$

B2-bcc (β_2) $(Al,Ti,V,Va)_{0.5}$: $(Al,Ti,V,Va)_{0.5}$

hcp (α) $(Al,Ti,V)_1$

Ti_3Al (α_2) $(Al,Ti,V)_{0.75}$:$(Al,Ti,V)_{0.25}$

Many parameters in the expression for the excess Gibbs energy (Section 3.3.1) need be modified accordingly, as will be discussed in detail in Section 5.5.

5.4 The Ti-Al-Cr-V system excluding substitutional vacancy

With the CALPHAD approach, a set of self-consistent thermodynamic parameters for the ordered B2 phase was obtained – see Table 5 – using the two sublattice model and experimental data previously assessed. The relative systems were well reproduced by these parameters.

Table 5: Thermodynamic parameters of the B2 phase in the Ti-Al-Cr-V quaternary system. G(Bcc_B2,Al:Ti;0) refers to the 0th order of interaction parameter (as mentioned in Section 3.3.1) between Al and Ti in the B2 phase; other parameters refer to interaction parameters in a similar way.

Thermodynamic parameters	Value/Jmol^{-1}
G(BCC_B2,AL:TI;0)	-11640+4.9*T
G(BCC_B2,TI:AL;0)	-11640+4.9*T
G(BCC_B2,AL:V;0)	-4000+10*T
G(BCC_B2,V:AL;0)	-4000+10*T
G(BCC_B2,AL:CR;0)	-1000-3.63+T
G(BCC_B2,CR:AL;0)	-1000-3.63*T
G(BCC_B2,AL:AL,TI;0)	5800
G(BCC_B2,AL,TI:AL;0)	5800
G(BCC_B2,AL:AL,TI;1)	-1200
G(BCC_B2,AL,TI:AL;1)	-1200
G(BCC_B2,TI:AL,TI;0)	9500
G(BCC_B2,AL,TI:TI;0)	9500
G(BCC_B2,TI:AL,TI;1)	-5000
G(BCC_B2,AL,TI:TI;1)	-5000
G(BCC_B2,AL:AL,V;0)	4000-10*T
G(BCC_B2,AL,V:AL;0)	4000-10*T
G(BCC_B2,V:AL,V;0)	4000-10*T
G(BCC_B2,AL,V:V;0)	4000-10*T
G(BCC_B2,AL:AL,CR;0)	1000+3.63*T
G(BCC_B2,AL,CR:AL;0)	1000+3.63*T
G(BCC_B2,CR:AL,CR;0)	1000+3.63*T
G(BCC_B2,AL,CR:CR;0)	1000+3.63*T
G(BCC_B2,TI:AL,V;0)	4000-10*T
G(BCC_B2,AL,V:TI;0)	4000-10*T
G(BCC_B2,TI:AL,CR;0)	-28600+12.9*T
G(BCC_B2,AL,CR:TI;)	-28600+12.9*T

5.4.1 Ti-Al system

The phase diagram for the Ti-Al binary system which follows from this dataset is given in Fig. 24. The dashed line represents the order-disorder transformation between the A2 phase and the B2 phase. The transformation temperature is predicted to change from 1200°C to

1400°C as the composition changes from 20 to 40 at.%Al. The ordered B2 phase is stabilised to higher temperatures with an increase in Al content, consistent with the positive effect of Al in the tendency for ordering [9].

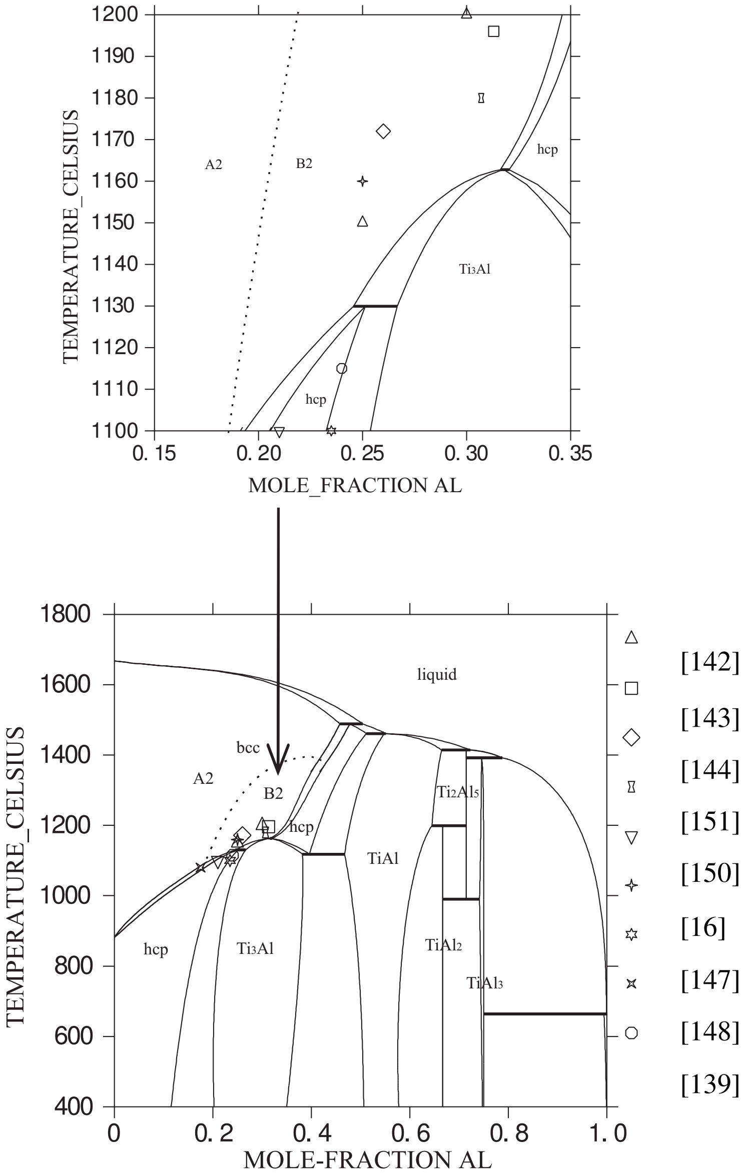

Figure 24: The calculated Ti-Al binary phase diagram versus different data.

With these optimised binary parameters, the two peritectoid reactions involving the ordered B2 phase – α+β→α2 and β+α2→α can be modelled and the predictions compared with reported experimental data, see Table 6. The calculated temperature of the first reaction is 1160°C, within the error range of 10°C set in the procedure of optimisation considering the congruent temperature of the α_2 phase calculated by the initial database [118] – 1164°C. The compositions of Al in the three related phases (β_2, α, α_2) were assessed to be ~28, 33, and 32 in at.% [123] based on the extrapolation of phase boundary data for α/β and α/α_2. Therefore the error range of the composition of β_2 was a little larger than for the other phases since it was extrapolated to be about 28at.%Al in the assessment. The calculated values were 31.9, 32.4 and 32 in at.%, which are reasonable.

Table 6: Calculated results of the invariant reactions involving B2 phase in the Ti-Al binary system compared with experimental or assessed data.

Invariant reaction	T/°C	x(Al)/at.%			Ref.
		β	α	α_2	
$\beta+\alpha\rightarrow\alpha_2$	~1250	-	-	-	[138]
	1215	-	-	-	[139]
	~1150	-	-	-	[140]
	~1135	-	-	-	[141]
	~1200	~29	35	30	[142]
	1196	28.7	32	31.3	[143]
	1200±10	~28	33	32	[123]
	1162	31.3	32.4	32	This work
		β	α_2	α	
$\beta+\alpha_2\rightarrow\alpha$	1272±8	23.9	28	26	[144-146]
	1100	15.5	25.3	23.5	[147]
	1080±20	15	22.5	17.5	[138, 148]
	1100	15.7	25.3	21	[149, 150]
	1180	18.7	26	~30.7	[151]
	1115	16	27	24	[139]
	~1150	24	26	25	[142]
	1160±10	21.5	26	25	[16]
	1170±10	25	27.5	27	[123]
	1124	24.7	26.8	26	This work

For the other peritectoid reaction, the calculated temperature is 1124°C. As the difference between the temperatures of these two reactions has been considered to be greater than 30°C in all previous research, the experimental data 1115°C [139] was given the most weight – within the optimisation error range, approximately 9°C different from the calculated 1124°C. The compositions of these phases (β_2, α_2, α) in the calculation were 24.7, 26.8 and 25.3 in at.%, all of which are lower in Al content than the assessed values 25, ~27.5 and 27 in at.% [123]. This difference is due to the change of temperature. The lower temperature favours the more stable ordered B2 phase, making the compositions move towards the Ti-rich side. However, the composition of alpha agrees well with the value of 25at.%Al given in [139].

In addition to the phase equilibria, the degree of ordering [15] is another key factor by which the accuracy of the thermodynamic optimisation can be assessed. The binary ordered B2 phase is theoretically considered to consist of two sublattices, one occupied by Al atoms and the other by Ti atoms. If the composition of the alloy is not stoichiometric, some excess atoms must become anti-site atoms or alternatively some sites would be occupied by vacancies. The expression of the degree of ordering has been defined in Section 2.2.1.

The ordered B2 phase was modelled here as $(Ti,Al)_{0.5}$:$(Ti,Al)_{0.5}$, so that any deviation from stoichiometry was accounted for by anti-site defects. The site fractions (Y in the figures) of Ti and Al in each sublattice at 1200°C were calculated and are as shown in Fig. 25 and Fig. 26. For the Ti-rich alloys in the composition range 53%Ti to 57%Ti, the Ti-rich sublattice is almost completely occupied by Ti atoms, which indicates a very high degree of ordering in the bcc phase. The excess Ti atoms exist as anti-site defects on the other sublattice. It is a similar case for the Al-rich side. Therefore, the model for the ordered B2 phase could be written as $Ti_{0.5}$:$(Ti,Al)_{0.5}$ for the Ti-rich alloys, and $(Ti,Al)_{0.5}$:$Al_{0.5}$ for the Al-rich ones. As mentioned in Section 2.2.1, the degree of ordering can be calculated by the difference of occupation probabilities of the element within the two sublattices. Taking the alloy Ti-50%Al for example, the degree of ordering is calculated by, Y(B2,Ti)-Y(B2,Ti#2), and is plotted against temperature as shown in Fig. 27. The degree of ordering decreases from 1 to 0 with increasing temperature in a reasonable way.

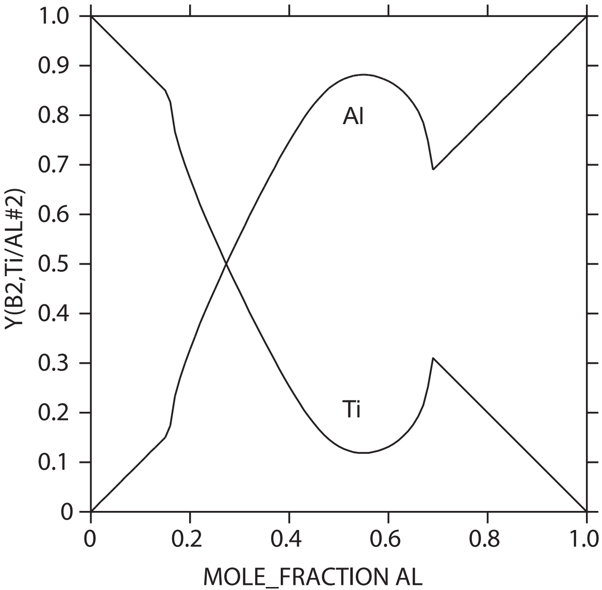

Figure 25: The site fraction of different atoms in the Al-rich sublattice, Y(B2,Ti/Al#2), in the binary Ti-Al system at 1473K. Note #2 refers to the Al-rich sublattice.

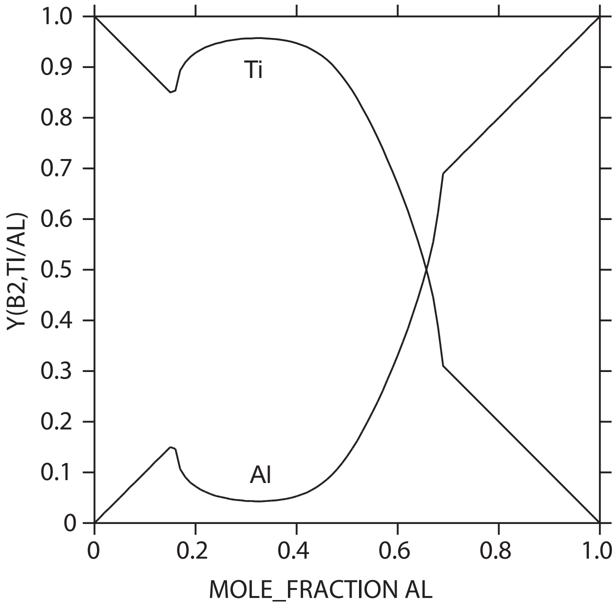

Figure 26: The site fraction of different atoms in the Ti-rich sublattice, Y(B2,Ti/Al), in the binary Ti-Al system at 1473K.

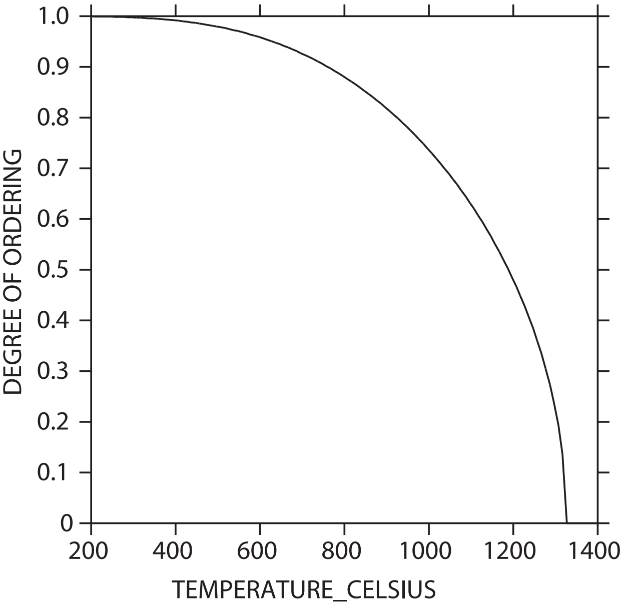

Figure 27: Degree of ordering for the Ti-50%Al alloy.

5.4.2 Al-Cr system

The calculated phase diagram of the Al-Cr system is given in Fig. 28. The dashed line again represents the order-disorder transformation. The single phase region of the ordered B2 phase is very small, which is consistent with the conclusion from the work of Helander and Tolochko [19].

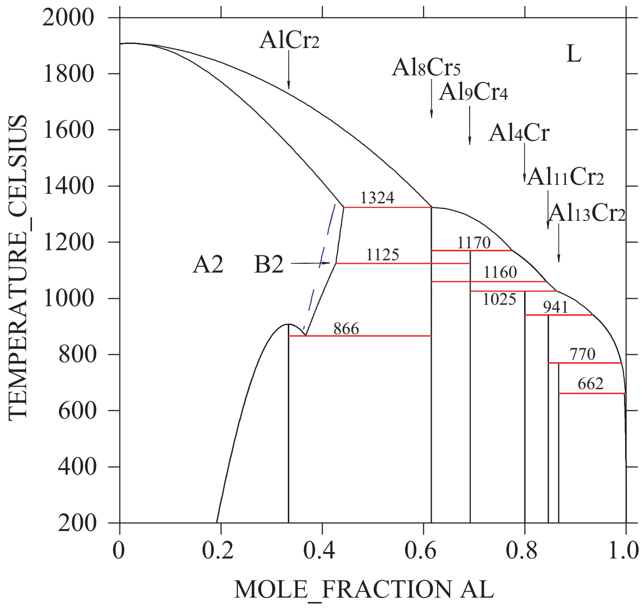

Figure 28: The calculated phase diagram of the Al-Cr binary system.

5.4.3 Ti- Al-V system

It is interesting to examine the effect of the additional ternary parameters for the ordered B2 phase (as listed in Table 5) on the isothermal sections in the Ti-Al-V system. Isothermal sections are reproduced in Figs. 29-33. Once again, the dashed lines represent the order-disorder transformation, and a single phase region of B2 is predicted to occur within the region delimited by the dashed line. As the temperature decreases, the order-disorder transformation line moves towards the V-rich corner, illustrating that the ordering temperature decreases with increasing V content [25].

On the predicted phase diagrams, the B2 phases found using transmission electron microscopy are given, *e.g.* at 1200°C in Fig. 29. Most calculated isothermal sections are consistent with the experimental data; there is only some deviation of the two-phase region (bcc+Ti_3Al) at the Ti-rich corner at some temperatures. It is considered that these deviations are caused mainly by errors in the initial database [118], which was not altered during the work reported here. As the calculated diagrams without the ordered B2 phase by the initial database fit the experiment of the bcc+Ti_3Al two-phase region (see Figs. 34-38), the phase boundaries between the ordered B2 phase and other phases move towards the side of the second phases, *i.e.* the B2 phase-field enlarges. The liquidus projection was calculated to be as shown in Fig. 39; the associated invariant reaction temperatures are listed in Table 7.

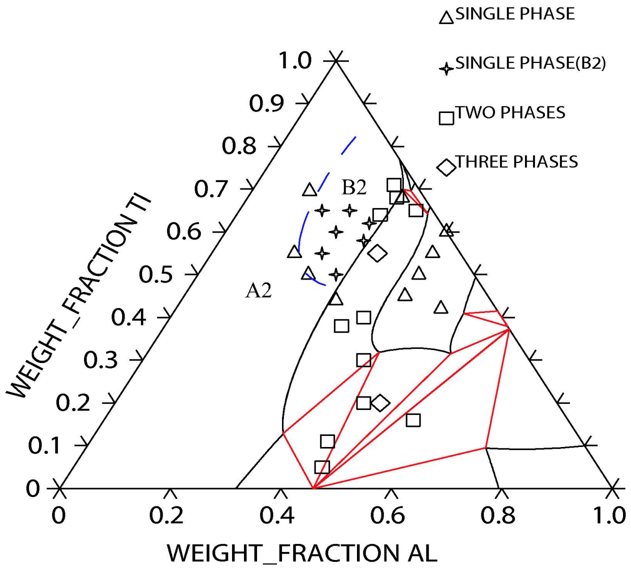

Figure 29: The isothermal section of the Ti-Al-V ternary system at 1200°C versus experimental data [23]. The experimental data of the B2 phase fall into the calculated B2 phase region.

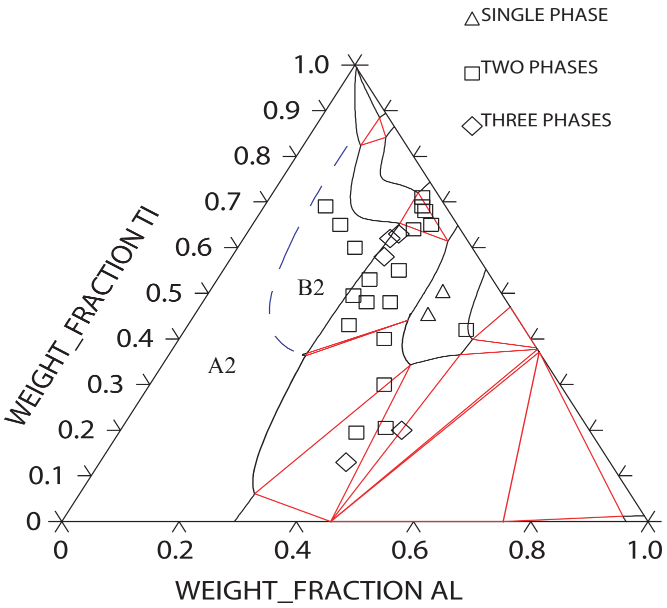

Figure 30: The isothermal section of the Ti-Al-V ternary system at 900°C versus experimental data [23]. The experimental data of bcc+Ti_3Al fall into the calculated B2 phase region which is due to the fact that no change was made for the A2 phase in the initial database [118].

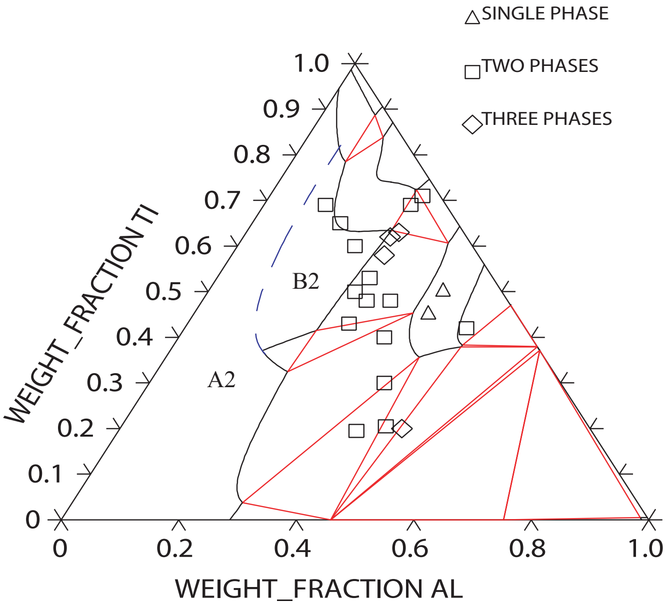

Figure 31: The isothermal section of the Ti-Al-V ternary system at 800°C versus experimental data [23]. The experimental data of bcc+Ti_3Al fall into the calculated B2 phase region which is due to the fact that no change was made for the A2 phase in the initial database [118].

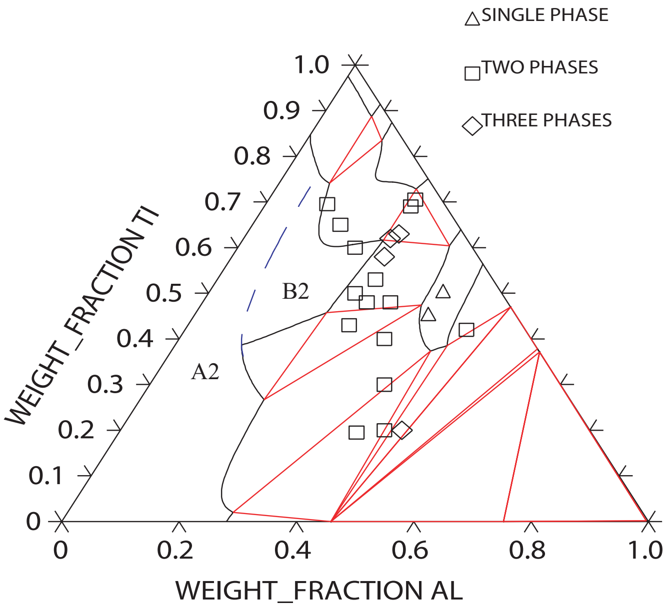

Figure 32: The isothermal section of the Ti-Al-V ternary system at 700°C versus experimental data [23]. The experimental data of bcc+Ti_3Al fall into the calculated B2 phase region which is due to the fact that no change was made for the A2 phase in the initial database [118].

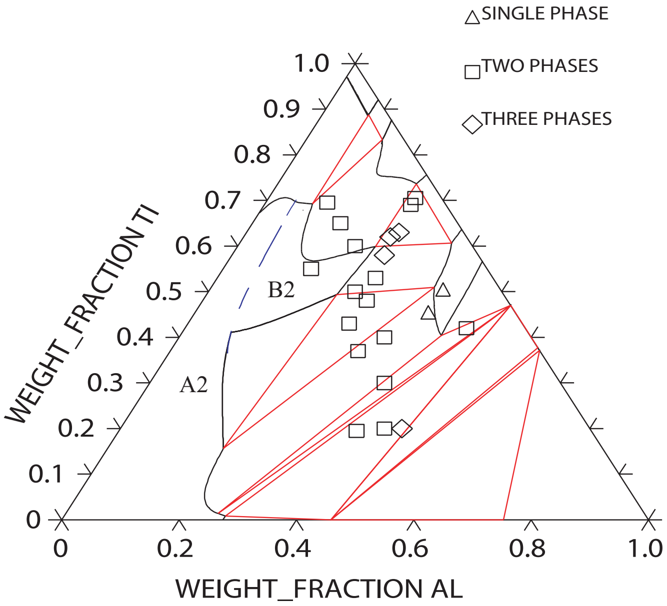

Figure 33: The isothermal section of the Ti-Al-V ternary system at 600°C versus experimental data [23]. The experimental data of bcc+Ti_3Al fall into the calculated B2 phase region which is due to the fact that no change was made for the A2 phase in the initial database [118].

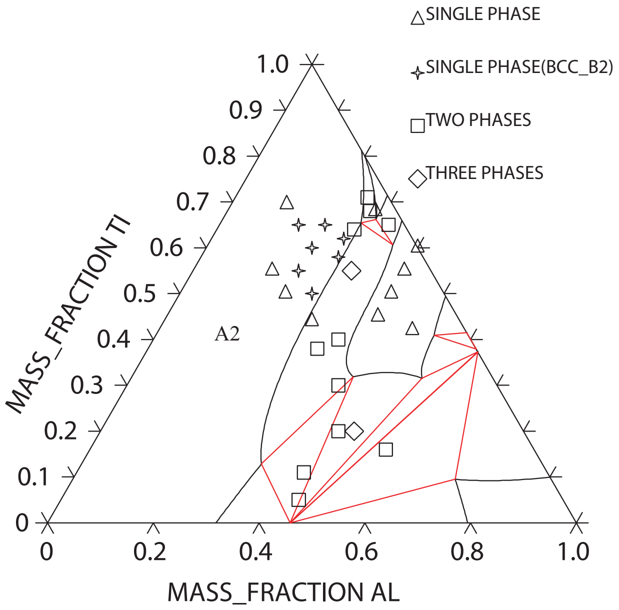

Figure 34: The isothermal section of the Ti-Al-V ternary system without the B2 phase at 1200°C versus experimental data [23]. The calculated bcc+hcp phase region fit the experimental data.

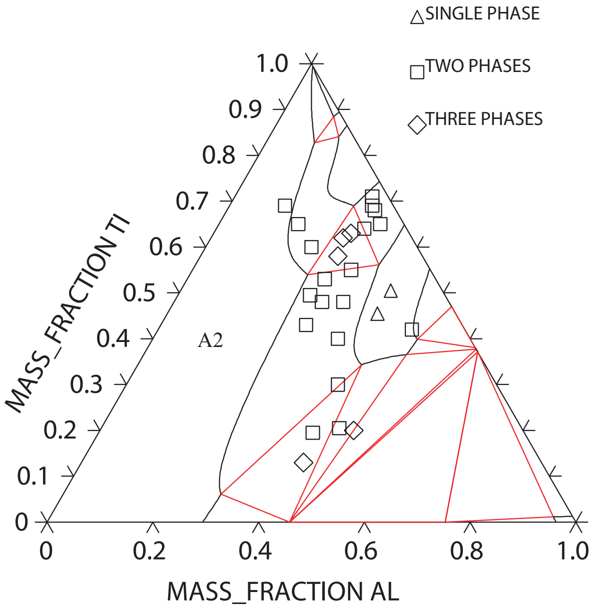

Figure 35: The isothermal section of the Ti-Al-V ternary system without the B2 phase at 900°C versus experimental data [23]. The calculated bcc+Ti_3Al phase region fit the experimental data.

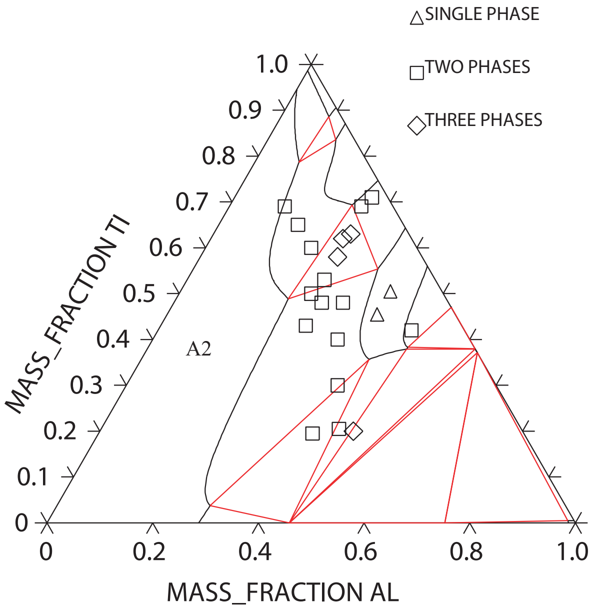

Figure 36: The isothermal section of the Ti-Al-V ternary system without the B2 phase at 800°C versus experimental data [23]. The calculated bcc+Ti_3Al phase region fit the experimental data.

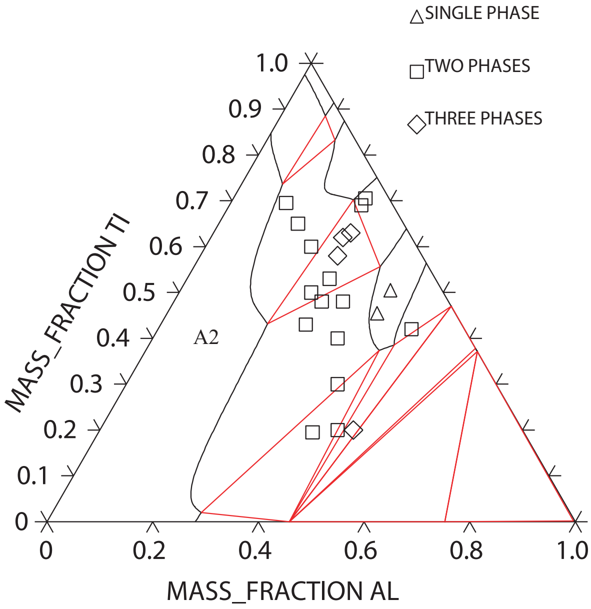

Figure 37: The isothermal section of the Ti-Al-V ternary system without the B2 phase at 700°C versus experimental data [23]. The calculated bcc+Ti_3Al phase region fit the experimental data.

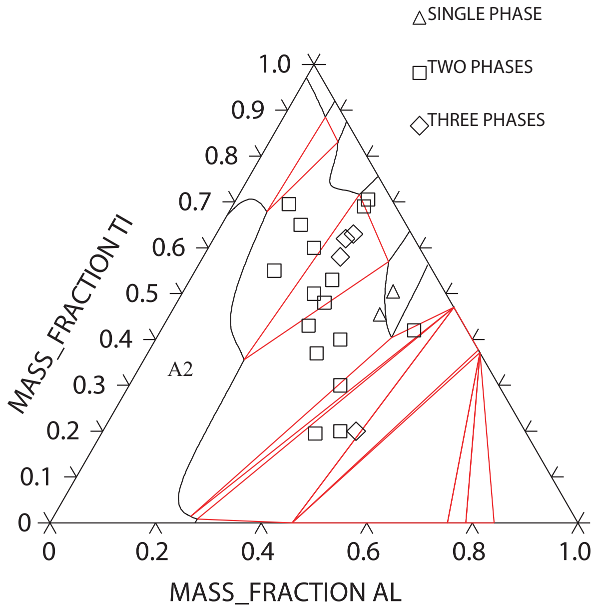

Figure 38: The isothermal section of the Ti-Al-V ternary system without the B2 phase at 600°C versus experimental data [23]. The calculated bcc+Ti_3Al phase region fit the experimental data.

Table 7: The calculated invariant reactions in the Ti-Al-V system.

Invariant reaction	Temperature / °C
L+B2→TiAl+hcp	1487
L+B2→TiAl+Al_8V_5	1407
L+Ti_2Al_5→$TiAl_3$+TiAl	1374
L+TiAl→$TiAl_3$+Al_8V_5	1205
L+Al_8V_5→$TiAl_3$+$Al_{23}V_4$	1035
L+$Al_{23}V_4$→$TiAl_3$+Al_7V	695
L+Al_7V→$TiAl_3$+$Al_{10}V$	672
L+$TiAl_3$+$Al_{10}V$→Al	666

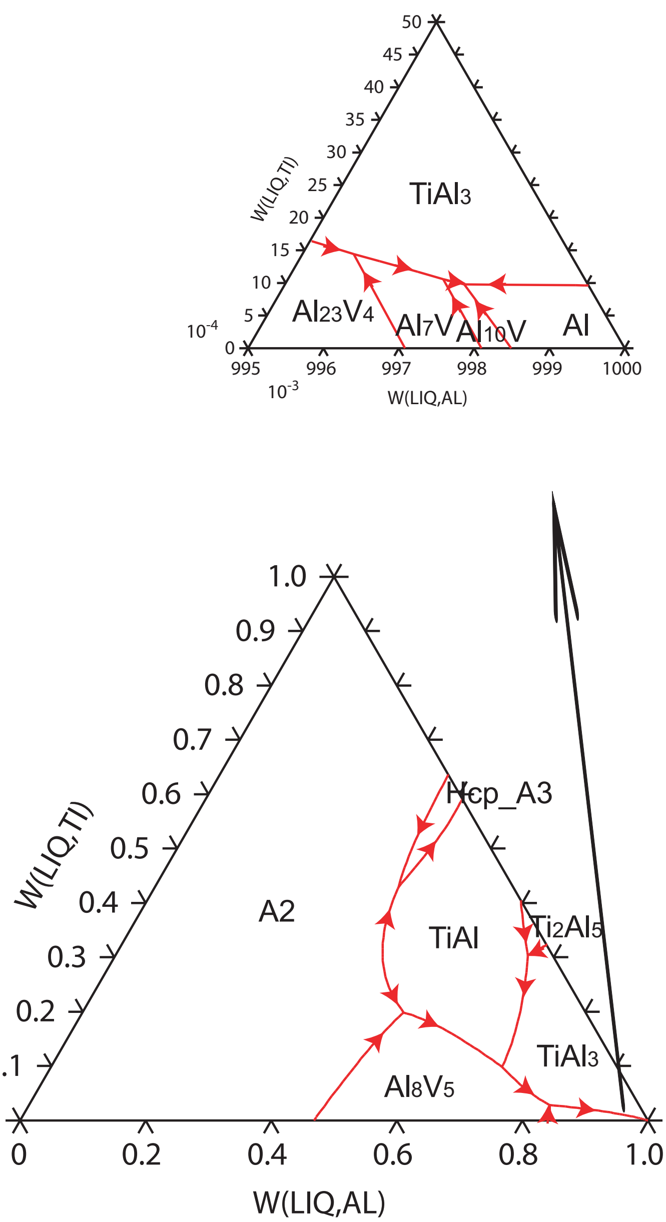

Figure 39: The calculated liquid projection of the Ti-Al-V ternary system.

5.4.4 Ti-Al-Cr system

The calculated isothermal sections of the Ti-Al-Cr system at 600°C, 800°C and 1000°C are given in Figs. 40-42, respectively. In the section at 600°C (Fig. 40), no B2 phase is stable and most of the phase relationships agree with the assessed diagram [136]. The absence of $L1_2$ phase in the section requires further improvement of the parameters of the $L1_2$ phase in the parent Ti-database [118] which is beyond the scope of the present work.

For the 800°C section, see Fig. 41, the isolated region in the centre of the diagram corresponds to the single phase region of the B2 phase. The phase equilibria between B2 and the other phases (such as TiAl and Ti_3Al) again show good agreement with the available experimental information, with two exceptions. In the experimental section in Fig. 41 it shows a schematic illustration of the B2 phase region according to a few terminal compositions; while the shape of the calculated B2 phase boundary is based on solubility of Al and Cr in Ti, and thus deviates from the schematic boundary of experiment. Additionally, the Al solubility in C14/C36 is too large, making the C14/C36 phase too stable; this has the effect of replacing the alpha-$TiCr_2$ (C15) in the phase equilibrium with the B2 and Ti_3Al phases.

In the isothermal section at 1000°C (Fig. 42), the calculated phase equilibria fit the experimental results very well. In the paper of Jewett and Dahms [152], there is a three phase equilibrium between C14, C36 and A2 in the sample ‘Alloy No. 2’ listed in the ‘Table – 1000°C quenched alloy compositions’, but from the ‘Figure – Partial 1000°C isothermal section of the Ti-Cr-Al system, showing the solubility and phase equilibria of the $Ti(Cr,Al)_2$ phase’, this equilibrium involves the B2 phase rather than A2. Using the thermodynamic calculation present here, it is the disordered A2 phase rather than the ordered B2 phase which appears. Therefore, as shown in Fig. 43, the A2-B2 transformation line suggested in [152] needs to be moved slightly towards the Al-rich side. Moreover, no three phase region of ‘B2+β-$TiCr_2$+γ-$TiCr_2$ (B2+C36+C14)’ is obtained; this is due to the nature of the thermodynamic model used to describe the Ti-Cr binary system. As the low-temperature stable C36 phase and the high-temperature stable C14 phase exhibit similar compositions, for simplicity both are modelled as the same phase here. Hence the three phase region ‘B2+C36+C14’ appears as a two phase region.

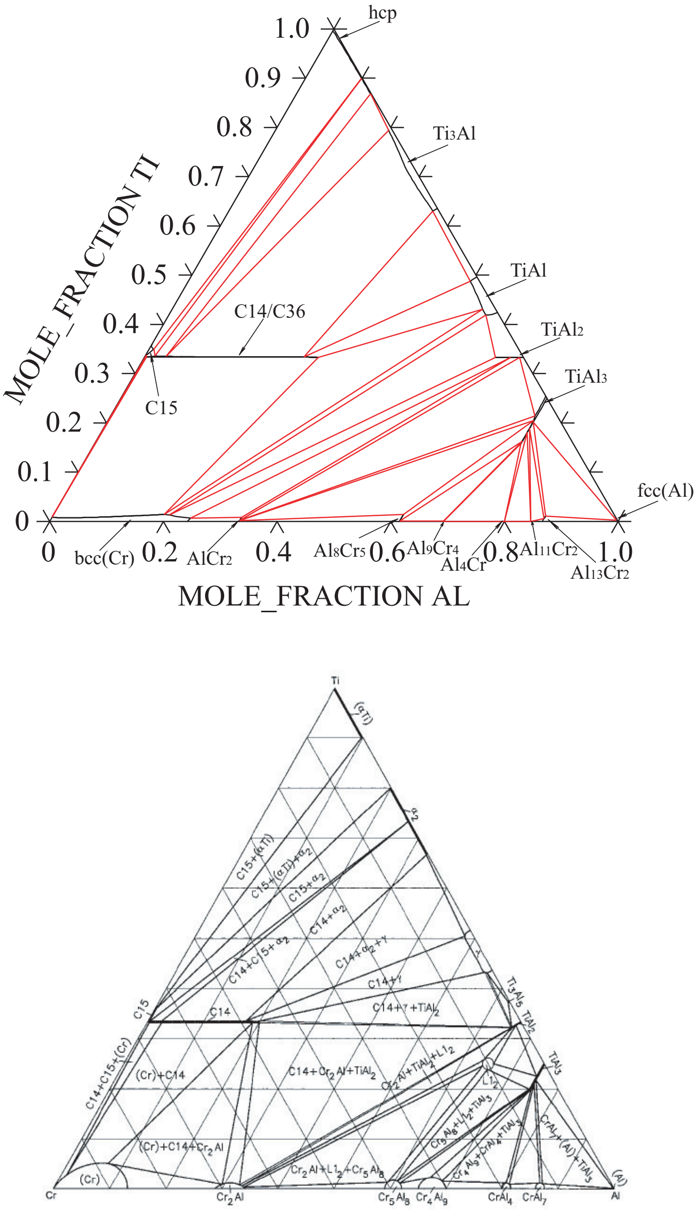

Figure 40: The calculated isothermal section (upper) of the Ti-Al-Cr system at 600°C and the assessed diagram (lower) [136].

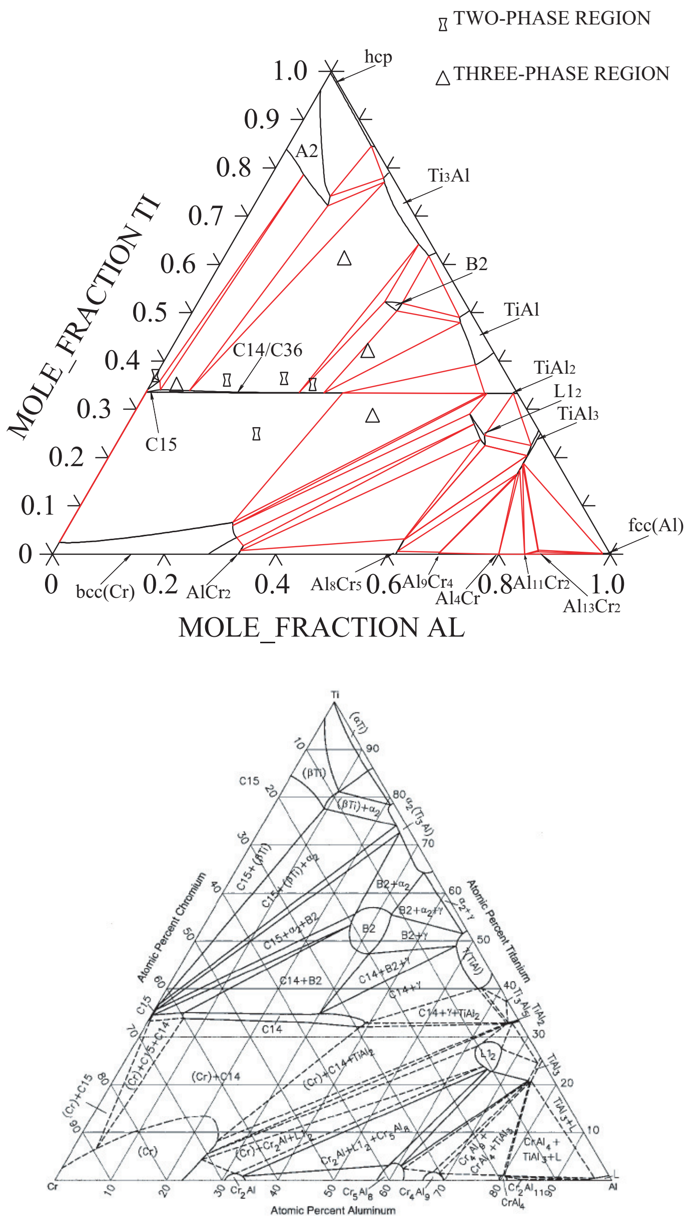

Figure 41: The calculated isothermal section (upper) of the Ti-Al-Cr system at 800°C and the assessed diagram (lower) [136].

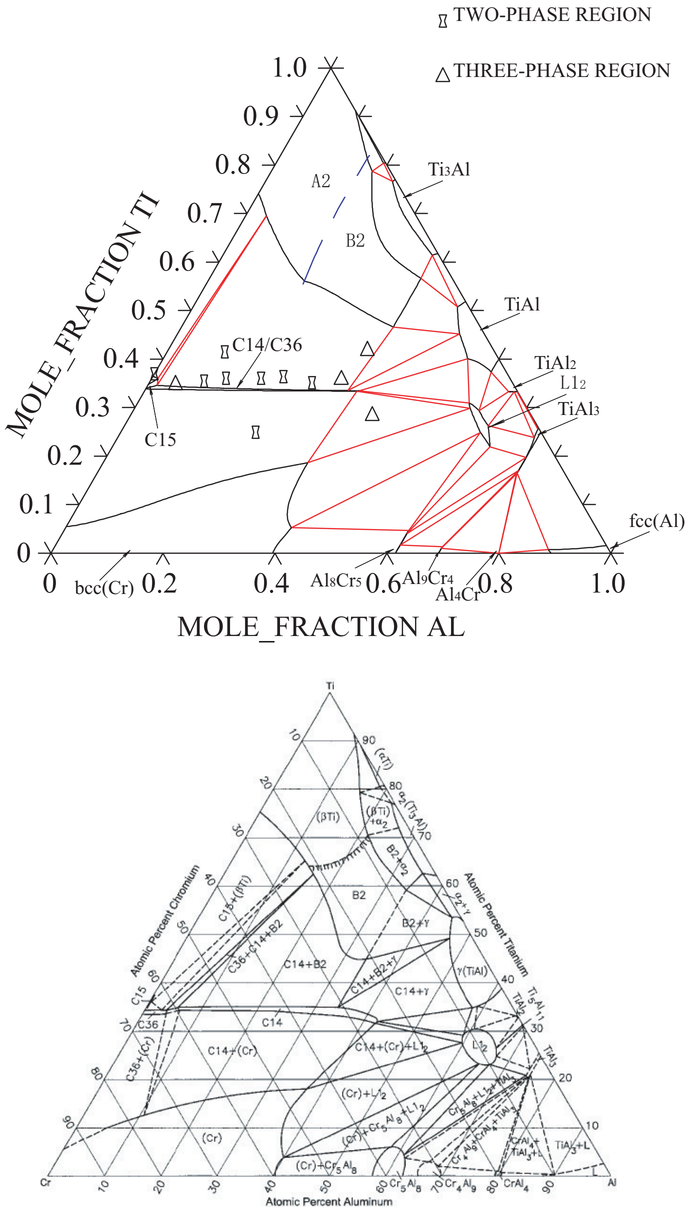

Figure 42: The calculated isothermal section (upper) of the Ti- Al-Cr system at 1000°C and the assessed diagram (lower) [136].

Additionally, the calculated liquidus projection of the Ti-Al-Cr system is shown in Fig. 44. The predicted invariant reactions are given in Table 8, and indicate that no B2 phase is stable at high temperatures.

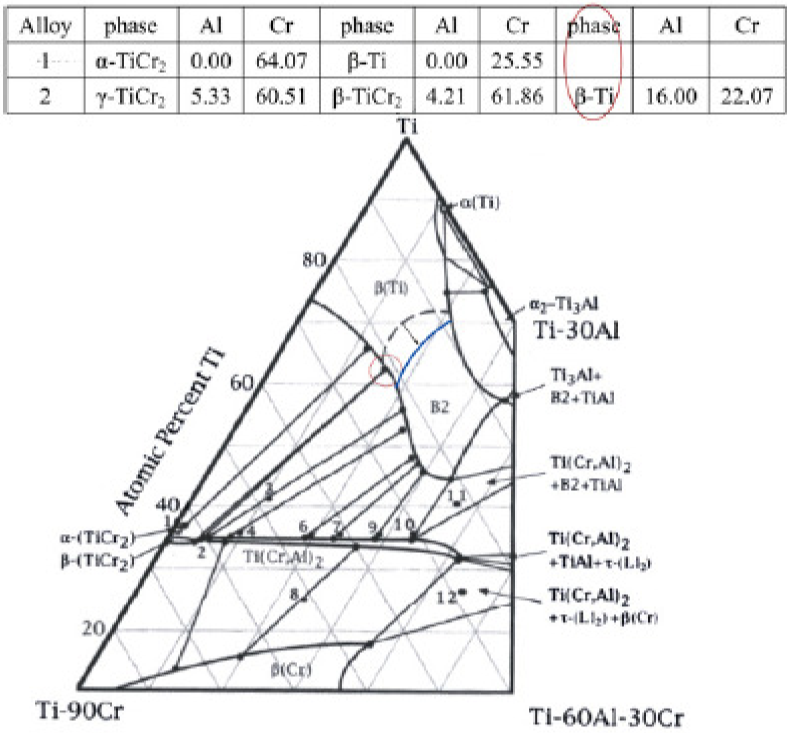

Alloy	phase	Al	Cr	phase	Al	Cr	phase	Al	Cr
1	α-$TiCr_2$	0.00	64.07	β-Ti	0.00	25.55			
2	γ-$TiCr_2$	5.33	60.51	β-$TiCr_2$	4.21	61.86	β-Ti	16.00	22.07

Figure 43: Illustration of the correction of the inconsistency in the phase equilibria in the isothermal section of the Ti-Al-Cr system at 1000°C [152].

Table 8: The calculated invariant reactions in the Ti-Al-Cr system.

Invariant reaction	Temperature / °C
$L+TiAl \rightarrow L1_2+Ti_2Al_5$	1356
$L+Ti_2Al_5 \rightarrow L1_2+Ti_3Al$	1337
L+hcp→bcc+TiAl	1328
$L+TiAl \rightarrow L1_2+bcc$	1318
$L \rightarrow Al_8Cr_5+L1_2+bcc$	1226
$L+L1_2 \rightarrow TiAl_3+Al_8Cr_5$	1184
$L+Al_8Cr_5 \rightarrow TiAl_3+Al_9Cr_4$_H	1154
$L+Al_9Cr_4$_H$\rightarrow TiAl_3+Al_9Cr_4$_L	1058
$L+Al_9Cr_4$_L$\rightarrow TiAl_3+Al_4Cr$	1016
$L+Al_4Cr \rightarrow TiAl_3+Al_{11}Cr_2$	938
$L+TiAl_3+Al_{11}Cr_2 \rightarrow Al_{13}Cr_2$	824
$L+TiAl_3+Al_{13}Cr_2 \rightarrow fcc$	664

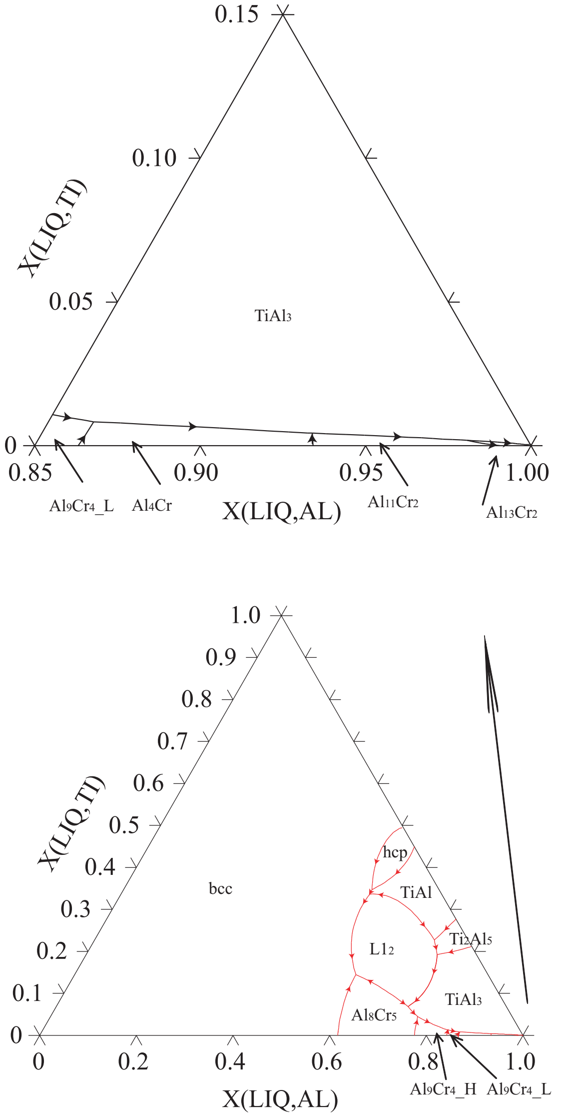

Figure 44: The calculated liquidus projection for the Ti-Al-Cr system.

5.4.5 Ti-Al-Cr-V system

Combining the constituent ternary assessments of the Ti-Al-V, Ti-Cr-V, Ti-Al-Cr and Al-Cr-V systems, phase equilibria in the quaternary Ti-Al-Cr-V system can be modelled by extrapolation. Some vertical sections are presented in Figs. 45-48 to analyse the influence of the Al addition on the formation of the ordered B2 phase. For example, the vertical section of Ti-32V-15Cr-xAl is shown in Fig. 46, for various values of weight composition x. The dashed line represents the order-disorder transformation, on which the transition temperature of the alloy with 5.6wt.%Al is 621°C, consistent with the experimental result of ~620°C given in [9]. From these series of figures, it can be seen that only for mean compositions greater than ~4wt.%Al – the precise value varying with V content – is the ordered B2 phase formed from the A2 phase (A2 – B2) above 500°C. This is consistent with the conclusions drawn from experiments [9] – 'An addition of over 4wt.%Al in the Ti-(20-37)V-15Cr-(0-7)Al alloys resulted in an ordered bcc (B2) structure'. In the region of less 4wt.%Al, the A2 phase transforms to the alpha phase first; any residual A2 phase could possibly transform to the B2 phase when the temperature goes below the A2-B2 transformation line, provided that this reaction is not kinetically hindered. Thus, as the A2-B2 transformation temperatures of those alloys with less 4wt.%Al are much lower than those with higher Al content, the B2 phases with less Al are not completely ordered. This explains why the diffuse maxima of the samples with 2wt.%Al are very weak, consistent with the conclusion of Loretto *et al.* [32], that the critical Al composition for the ordering is ~2wt.%.

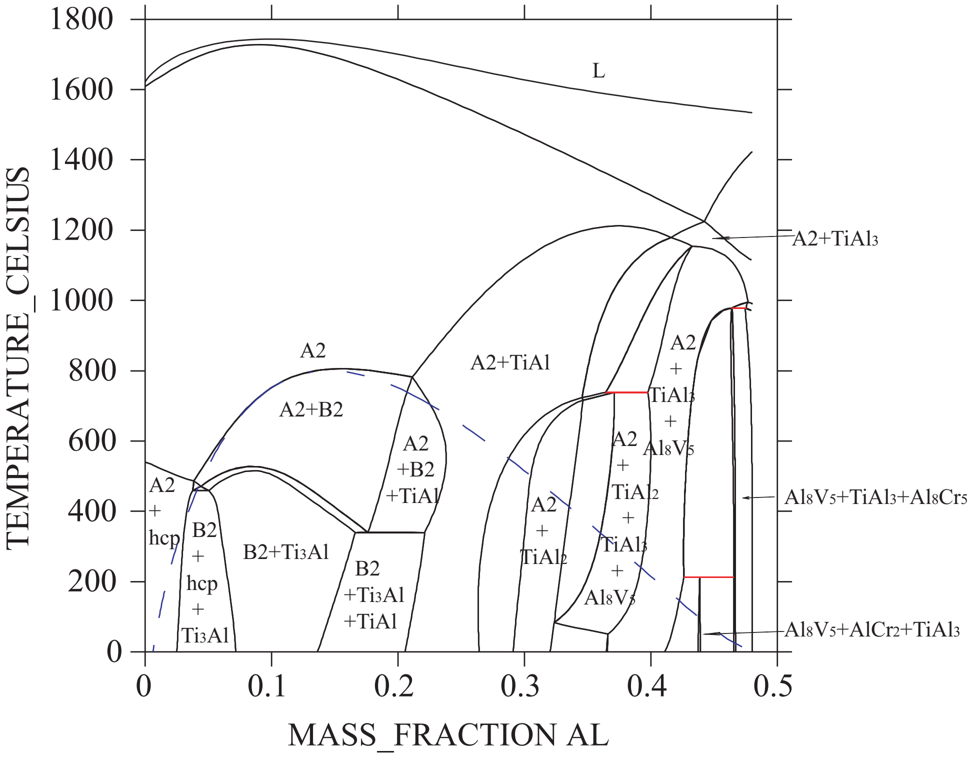

Figure 45: The calculated vertical section of Ti-37V-15Cr-*x*Al.

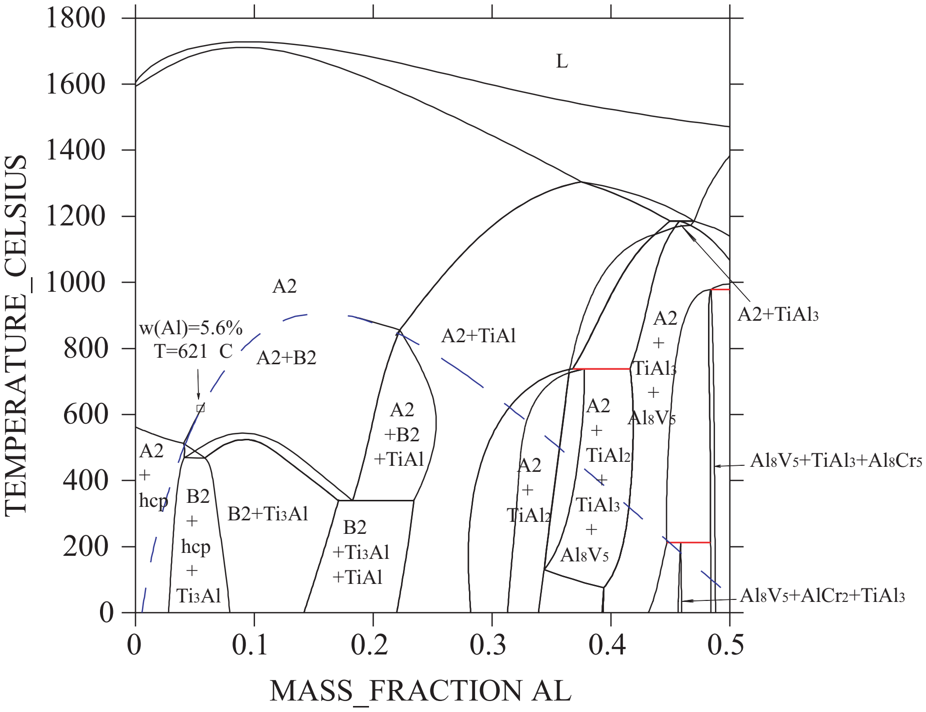

Figure 46: The calculated vertical section of Ti-32V-15Cr-*x*Al.

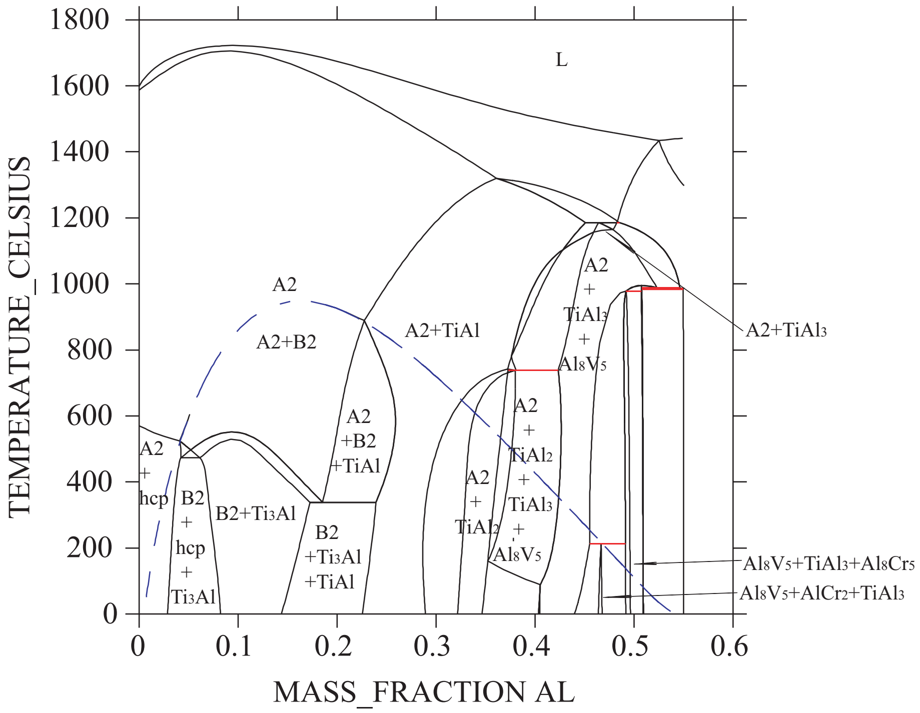

Figure 47: The calculated vertical section of Ti-30V-15Cr-*x*Al.

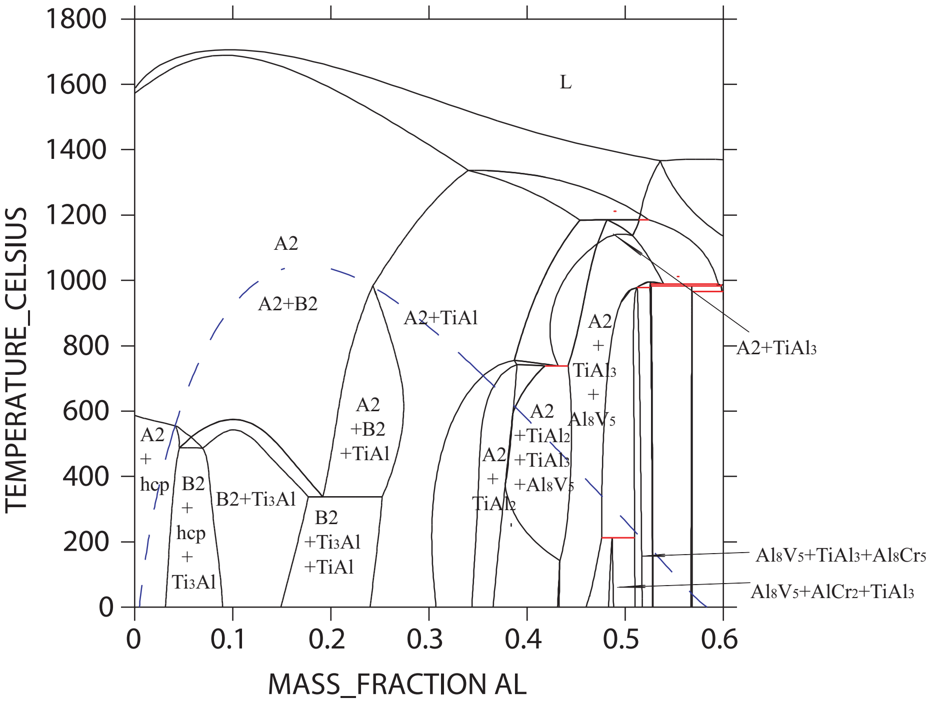

Figure 48: The calculated vertical section of Ti-25V-15Cr-*x*Al.

5.5 Ti-Al-V system including substitutional vacancies

5.5.1 Ti-Al binary system

The thermodynamic description of the Ti-Al binary system (Section 5.4.1) was revised based on the information on point defects (Chapter 4) presented in this work. The revised description is also based on a previously published assessment [118]. In order to reflect the influence of point defects, substitutional vacancies were added into the thermodynamic model of the ordered B2 phase – $(Al,Ti,Va)_{0.5}:(Al,Ti,Va)_{0.5}$, and the model for the corresponding disordered A2 phase therefore becomes $(Al,Ti,Va)_1$. These changes also affect the parameters of the α and α_2 phases, the revised parameters of these are given in Table 9 and the corresponding phase diagram is shown in Fig. 49. Furthermore, Table 10 shows the temperatures and compositions of the two relevant peritectoid reactions in comparison to those found in other sources. Besides a sounder physical description, a better consistency with experimental data of phase equilibria is observed.

Fig. 50 shows the calculated Ti-Al phase diagram without the ordered B2 phase. In this case the bcc-hcp does not show the peculiar bending as seen in Fig. 49, and the α_2 phase Ti_3Al forms congruently from the α(hcp) phase at 1164°C. The same diagram, calculated using the authors previous description is also shown, using dotted lines [153]. It can be seen that the temperature of congruent formation of α_2 has increased after the re-optimisation. Taking the B2 phase into account will cause the bcc-hcp two phase region to bend sufficiently to form the $\beta+\alpha\rightarrow\alpha_2$ peritectoid reaction. However, the maximum temperature of this reaction cannot be higher than the temperature of congruent formation of α_2. The introduction of point defects into the A2/B2 model and the re-optimisation of the Ti rich part of the phase diagram did increase the temperature of congruent α_2 formation sufficiently, to raise the temperature of the peritectoid reaction from 1160°C to 1198°C. This is in very good agreement with the most recent assessment of the Ti-Al phase diagram by Schuster & Palm [123].

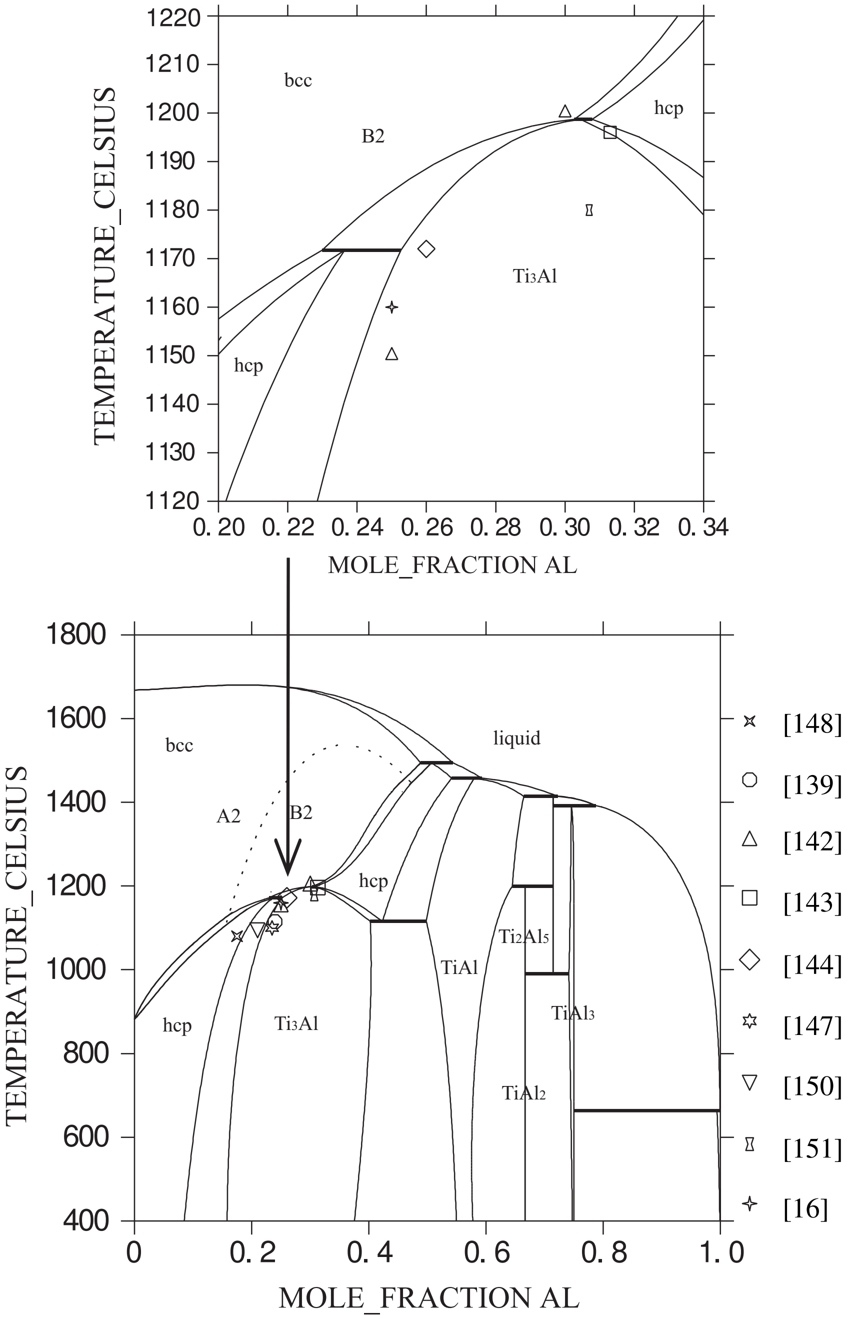

Figure 49: The calculated Ti-Al binary phase diagram and available experimental data.

Table 9: Thermodynamic parameters of the phase optimised in the Ti-Al-V ternary system. The same notations are used as those in Table 5.

Thermodynamic parameters	Value/$Jmol^{-1}$
α	
G(HCP_A3,AL,TI;0)	-128189+35.21*T
G(HCP_A3,AL,TI;1)	16034.9-12.18*T
G(HCP_A3,AL,V;0)	-95000+20*T
G(HCP_A3,AL,V;1)	-6000
G(HCP_A3,TI,V;0)	16500
G(HCP_A3,AL,TI,V;0)	13690.9-96.06*T
G(HCP_A3,AL,TI,V;1)	-81024+38.06*T
G(HCP_A3,AL,TI,V;2)	104295.8-96.27*T
β(A2)	
G(BCC_A2,AL,TI;0)	-121785+34.04*T
G(BCC_A2,AL,VA;0)	-95000+20*T
G(BCC_A2,AL,V;0)	-6000
G(BCC_A2,AL,V;1)	60000
G(BCC_A2,TI,V;0)	10500-1.5*T
G(BCC_A2,TI,V;1)	2000
G(BCC_A2,TI,V;2)	1000
G(BCC_A2,TI,VA;0)	150000
G(BCC_A2,V,VA;0)	150000
β(B2)	
G(BCC_B2,AL:TI;0)	-121785+34.0*T
G(BCC_B2,TI:AL;0)	-121785+34.0*T
G(BCC_B2,AL:VA;0)	5000-0.5*T
G(BCC_B2,VA:AL;0)	5000-0.5*T
G(BCC_B2,TI:VA;0)	26645-3.6*T
G(BCC_B2,VA:TI;0)	26645-3.6*T
G(BCC_B2,TI:AL,TI;0)	-8980
G(BCC_B2,AL,TI:TI;0)	-8980
G(BCC_B2,TI:AL,TI;1)	-3750
G(BCC_B2,AL,TI:TI;1)	-3750
G(BCC_B2,AL:TI,VA;0)	-75000
G(BCC_B2,TI,VA:AL;0)	-75000
α_2	
G(TI_3AL,AL:TI;0)	32363.6-8.258*T
G(TI_3AL,TI:AL;0)	-32363.6+8.258
G(TI_3AL,TI:V;0)	21500
G(TI_3AL,V:TI;0)	14000
G(TI_3AL,V:AL;0)	-6000-3*T

To be continued

Continued Table 9

G(TI$_3$AL,AL,TI:AL;0)	-71277.9+25.47*T
G(TI$_3$AL,AL,TI:TI;0)	-71277.9+25.47*T
G(TI$_3$AL,TI:AL,V;0)	-24435.5-0.45*T
G(TI$_3$AL,TI,V:AL,V;0)	8000-14.08*T

Table 10: Calculated results of the invariant reactions involving B2 phase in the Ti-Al binary system compared with experimental or assessed phase equilibria.

Invariant reaction	T/°C	*x*(Al)/at.%			Ref.
		β	α	α$_2$	
β+α→α$_2$	~1250	-	-	-	[138]
	1215	-	-	-	[139]
	~1150	-	-	-	[140]
	~1135	-	-	-	[141]
	~1200	~29	35	30	[142]
	1196	28.7	32	31.3	[143]
	1200±10	~28	33	32	[123]
	1162	31.3	32.4	32	Section 5.4.1
	1198	30.2	30.8	30.5	This work
		β	α$_2$	α	
β+α$_2$→α	1272±8	23.9	28	26	[144-146]
	1100	15.5	25.3	23.5	[147]
	1080±20	15	22.5	17.5	[138, 148]
	1100	15.7	25.3	21	[149, 150]
	1180	18.7	26	~30.7	[151]
	1115	16	27	24	[139]
	~1150	24	26	25	[142]
	1160±10	21.5	26	25	[16]
	1170±10	25	27.5	27	[123]
	1124	24.7	26.8	26	Section 5.4.1
	1172	23.0	25.3	23.6	This work

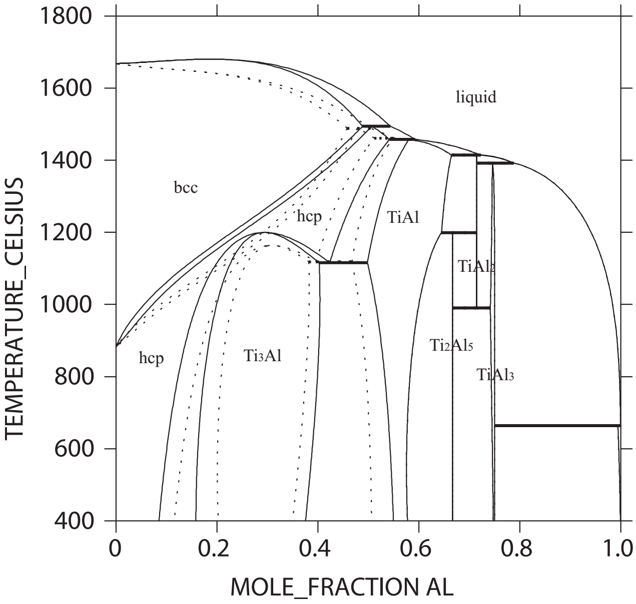

Figure 50: The comparison between the phase diagrams without B2 phase (Solid lines are the present work, dashed lines are from [118]).

Fig. 51 shows the vacancy concentration in the B2 phase versus temperature as obtained from CALPHAD calculations for Ti-30at.%Al. This alloy shows a B2 single phase region between 1210°C and 1490°C. An increases of the vacancy concentration with temperature is found up to about 1200°C followed by a decrease at higher temperatures. This is consistent with creation of vacancies due to increase of temperature, and their loss due to reduced degrees of ordering, which reflects greater opportunity of random arrangement of atoms in the crystal lattice. Calculations of vacancy concentrations using CALPHAD can be very helpful to explain vacancy-related effects at high temperatures - such as rapid precipitate growth in quenched alloys - especially when extrapolated to more complex alloys.

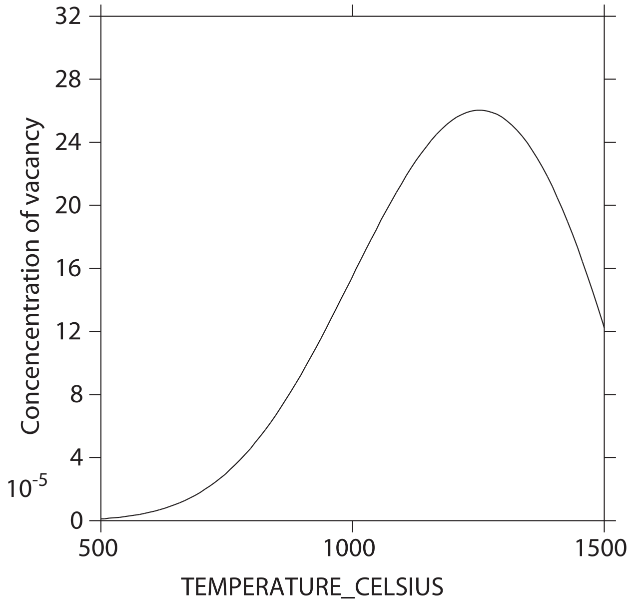

Figure 51: The calculated concentration of vacancy in Ti-30at.%Al alloy versus temperature from the present thermodynamic database.

5.5.2 Ti-Al-V ternary system

The Ti-Al-V ternary system has been thermodynamically re-optimised in order to provide the phase-field simulations which follow with essential information. The thermodynamic parameters of the newly optimised phases in the Ti-rich corner are listed in Table 9. Two isothermal sections (1200°C and 900°C) are calculated and compared with experimental data, see Fig. 52 and 53 respectively. Better agreement can be found in both sections than the results in the previous section, especially in the fitting of the phase equilibria involving the B2 phase.

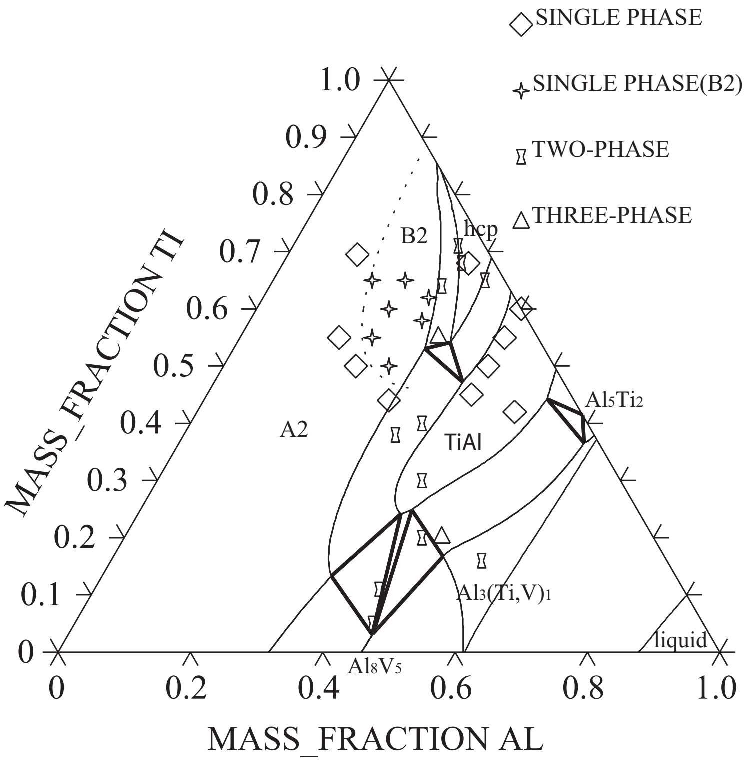

Figure 52: The calculated isothermal sections of Ti-Al-V system at 1200°C compared with experimental data [23].

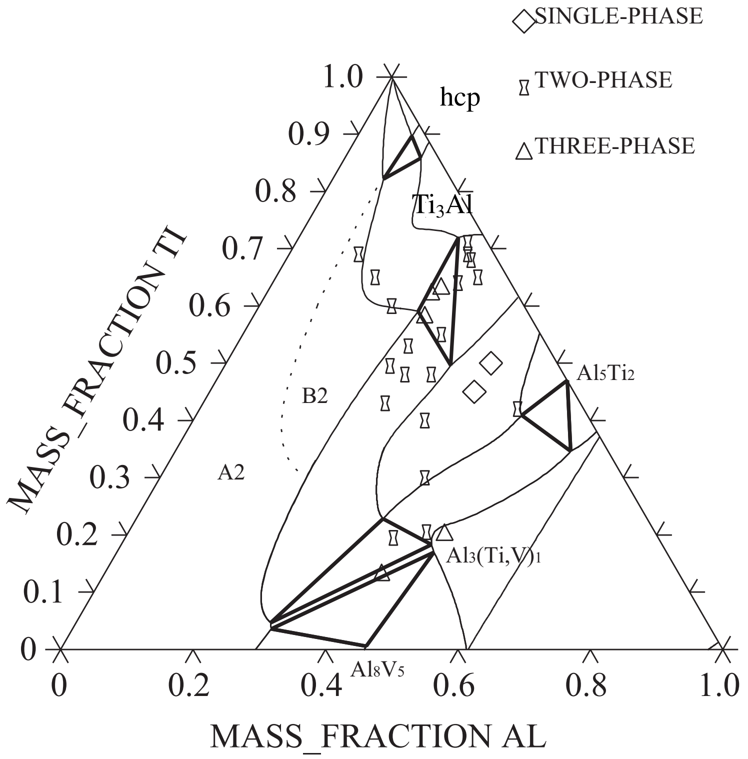

Figure 53: The calculated isothermal sections of Ti-Al-V system at 900°C compared with experimental data [23].

Moreover, as previously mentioned, the phase-field simulation is very sensitive to the temperature of β transus; so for this reason the calculated mole fractions of α and β phases in the Ti-6Al-4V alloy are plotted against temperature in Fig. 54. Note that oxygen can increase the temperature of the β transus, but this is not taken into account in the present work because oxygen is not included in the present database. The β transus is predicted to be 982°C, close to the experimental value. Obviously therefore it is suitable as a precondition of the simulation of the phase transformation. The phase fractions can be different from the experiment because of kinetic reasons; this will be discussed later in Section 7.3.1.

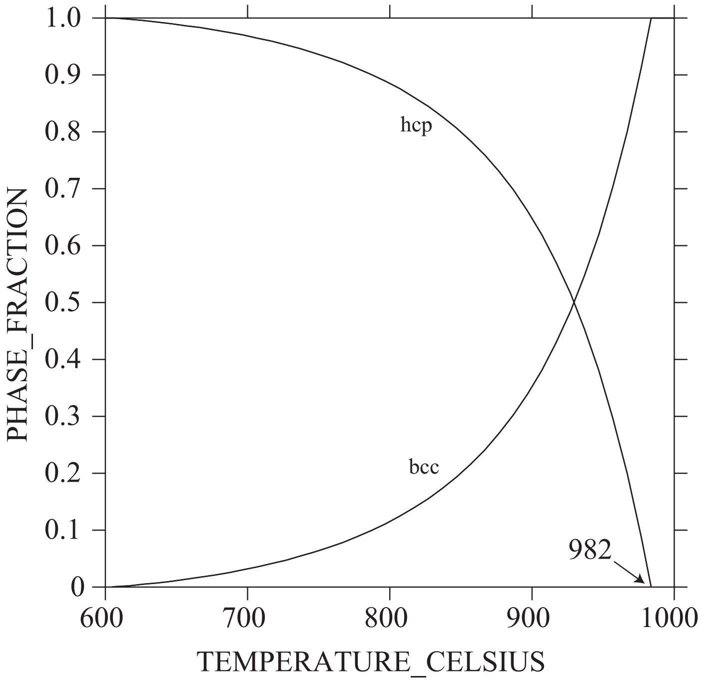

Figure 54: The calculated mole fractions of α and β phases of the Ti-6Al-4V alloy against temperature. Note β transus is at 982°C.

5.6 Experimental studies

Transmission electron microscopy and differential scanning calorimetry were used in the present work to verify the thermodynamic database and to assess the influence of ordering on the precipitation kinetics. As mentioned in Section 3.5, two Ti-Al binary alloy samples were annealed at 1200°C for 5 hours and then quenched in iced water. The two samples were examined using transmission electron microscopy (experimental details can be found in Section 3.5). Fig. 55 and 56 show diffraction patterns of the two binary alloy samples (Ti-27Al and Ti-31Al in at.%). Superlattice spots from the (100) planes in the [001] and [012] electron beam directions can be clearly identified in Fig. 55 taken from the quenched Ti-27at%Al sample. These two patterns confirm that the samples have a B2 structure. The situation in the quenched Ti31at%Al sample is apparently more complex since the two patterns obtained from different regions of a sample are from alpha2 and from B2 as can be seen in figure 56 which shows a [01-10] alpha 2 pattern and an [012] B2 pattern. This suggests either that the quenching rate was inadequate to retain 100% B2 or that the sample was quenched from the (B2+α) phase field; the alloy composition is very close to the α/β phase boundary (see Fig. 24 and 49). The α phase would order during the quench.

Similar experiments have also been done on the ternary Ti-Al-V alloy. Since there is a great deal of data for this ternary system [23], only one composition (Ti-10Al-36V in wt%) close to the A2/B2 boundary was chosen to be annealed at 800°C. The sample was quenched in iced water and examined using transmission electron microscopy. The sample was quenched in iced water and examined using transmission electron microscopy. The two patterns shown in Fig. 57 correspond to beam directions of [012] and [001] and contain superlattice patterns from the (010) and (100) planes confirming the structure as B2.

As suggested by Loretto *et al.* [33] some pieces of Ti-V-Cr-(0,2,4,6,8)Al samples were examined by differential scanning calorimetry to determine whether there is any peak during the heating/cooling process. Unfortunately, no obvious conclusion can be drawn from the results. This may be because the degree of ordering is continuously changing during the heating/cooling, and thus it is quite difficult to identify an abrupt change in the slope of the curve.

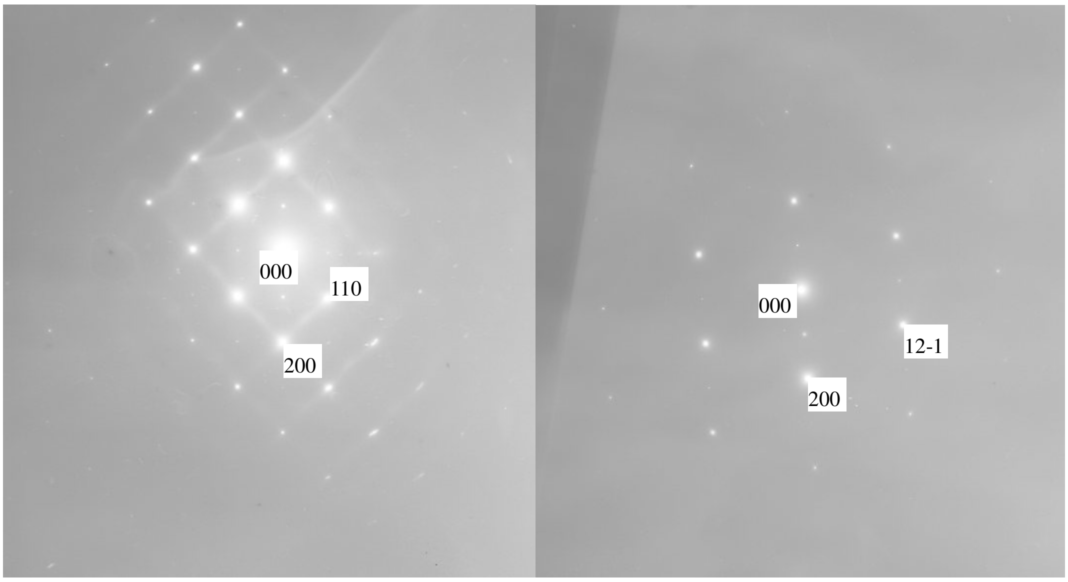

(a) <001>　　(b) <012>

Figure 55: Superlattice reflection found in Ti-27at.%Al alloy sample quenched in iced water from 1200°C (Ti-17wt.%Al).

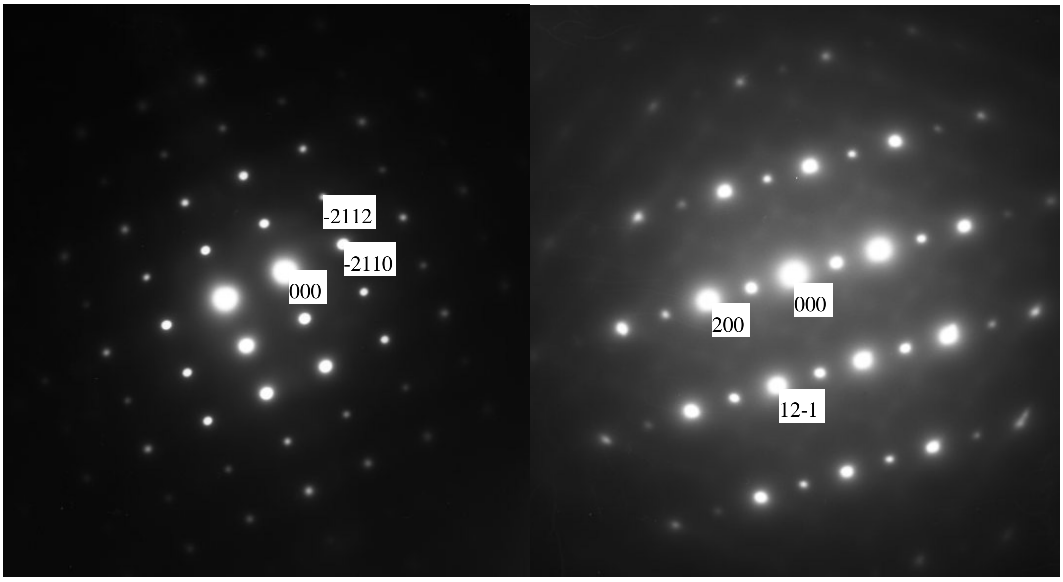

(a) <01-10> α_2 (b) <012> B2

Figure 56: Superlattice reflection found in Ti-31at.%Al alloy sample quenched in iced water from 1200°C (Ti-20wt.%Al).

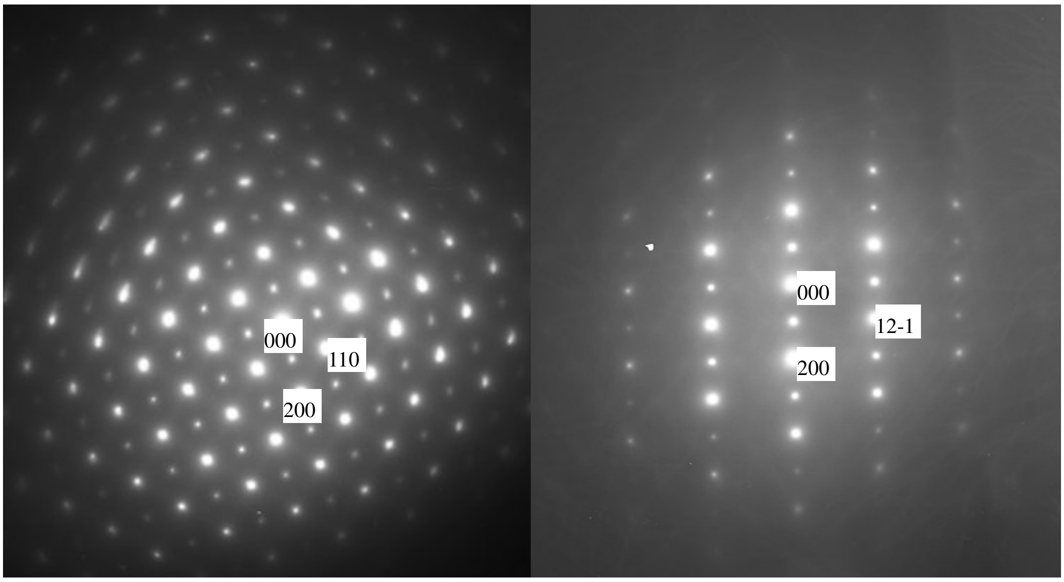

(a) <001> (b) <012>

Figure 57: Superlattice reflection found in Ti-32at.%V-17at.%Al alloy sample quenched in iced water from 800°C (Ti-36wt.%V-10wt.%Al).

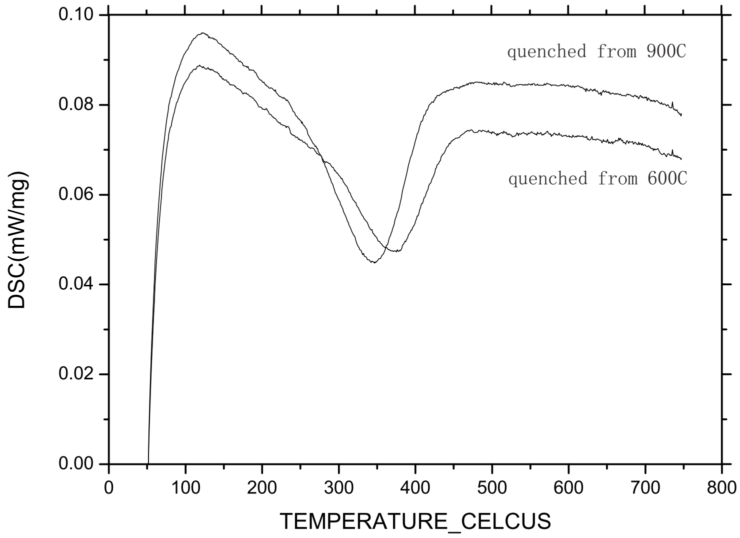

Figure 58: Investigation of kinetics of α precipitation from β matrix (Ti-25V-15Cr-6Al in wt.%) quenched from different temperatures by using differential scanning calorimetry. From the thermodynamic calculation, it is A2 phase region at 900°C, and B2 phase region at 600°C. The α precipitation starts to form from the A2 matrix earlier than from the B2 matrix.

The kinetics of α precipitation from two matrices – A2 (β) and B2 (β_2) in the Ti-25V-15Cr-6Al (in wt.%) alloy were investigated. One sample was annealed at 900°C (A2 regime) and quenched; the other sample was annealed at 600°C (B2 regime) and quenched. Both samples were then reheated from room temperature in the DSC. Both DSC curves were shown in Fig. 58. It can be seen that the α phase forms first from the A2 matrix. Also there is no direct evidence of any accelerating effect of the thermal vacancy induced by ordering on the α precipitations; however this does not mean that the precipitating kinetics does not relate to the ordering. Some further calculations of the activation energy of α precipitating using first-principles calculations may be helpful.

5.7 Summary

Based on the available experimental data, thermodynamic assessment of the relative stability of phases in the Ti alloy system has been carried out. When substitutional vacancies are excluded, the optimised expressions for the Gibbs energy of the ordered B2 phase in the Ti-Al-Cr-V quaternary system and constitutional binary and ternary systems have been chosen. Self-consistent thermodynamic parameters were obtained which should allow the future extension of the database to the analysis of higher order systems. The phase equilibria in the binary system and isothermal sections in the ternary system are well reproduced. The order-disorder transformation lines in the binary and ternary systems were calculated, as well as the degree of ordering in the Ti-Al binary system. The thermodynamic database of the Ti-Al-Cr-V system excluding substitutional vacancy can be used for the prediction of alloy compositions which are prone to the ordering reaction. Since it keeps the parameters from the initial database unchanged, it can be easily merged to a complex database which is useful for industrial applications.

With substitutional vacancies considered, the models for various phases in the Ti-Al-V ternary system have been modified and the thermodynamic parameters optimised. The results confirm improved agreement with the experimental data, as well as the results of first-principles calculations. The concentration of thermal vacancies has been calculated according to the database. This database reflects the crystal structures of the B2 alloy, and can be used to predict the situation with thermal vacancies.

Some experimental work has been carried out to validate the thermodynamic database, although not all the results unambiguously prove the existence of the ordering of the bcc phase. The results from transmission electron microscopy give evidence of the B2 phase in the Ti-Al binary system and the Ti-Al-V system. The differential scanning calorimetry results suggest that the thermal vacancies induced by ordering may not accelerate the kinetics of the α precipitating from the β matrix.

Chapter 6 Kinetic modelling of the atomic mobilities of the bcc phase in the Ti-Al-V system

6.1 Introduction

Besides thermodynamic data, kinetic data such as atomic mobilities are needed for the design of titanium alloys, so that phase equilibria and phase transformations can be simulated. Thus it is important to obtain a complete and comprehensive database for the kinetic mobilities of the bcc phase in the Ti-Al-V ternary system.

Within the methodology of CALPHAD approach, the kinetic assessments are also carried out based upon experimental measurements of diffusion phenomena. For example, the mobilities in the A2 phase have been assessed by Chen *et al.* [154]. Recently, Takahashi *et al.* [155] published some new data for interdiffusion coefficients in the A2 phase, which required the updating of the database. Using these data, Huang *et al.* [156] assessed the atomic mobilities for the A2 phase of the Ti-Al-V system. However, their work [156] is based on an extrapolated thermodynamic database from [112, 157, 158] without ternary thermodynamic parameters. In this chapter, two sets of kinetic parameters were optimised for the disordered bcc phase based on the two thermodynamic databases established in the previous chapter in the Ti-Al-V system.

6.2 Assessment of the experimental information of diffusion

Since the work by Chen *et al.* [154] published in 2004 assessed the experimental diffusivity of the beta phase in this ternary system, only the interdiffusion in the beta phase determined by Takahashi *et al.* [155] will be considered here. In the work by Takahashi *et al.* [155], eight diffusion couples were annealed for different durations, and examined using electron probe microanalysis. The ternary interdiffusion coefficients in the Ti-Al-V alloys were evaluated from the concentration profiles by using the extended Matano-Kirkaldy method [159, 160]. These experimental data were taken into account in the assessment work by Huang *et al.* [156], but the diffusion paths for two diffusion couples were not shown.

Table 11: Mobility parameters of the A2 phase in the Ti-Al-V ternary system. MQ refers to the frequency factor and activation enthalpy as mentioned in Section 3.3.3.

Kinetic parameters	Value/Jmol^{-1}
MQ(BCC_A2&AL,TI,V;0)	196361.50-128.45*T
MQ(BCC_A2&AL,AL,TI,V;0)	4665823.80
MQ(BCC_A2&TI,AL,V;0)	154441.90-450.79*T
MQ(BCC_A2&TI,AL,TI,V;0)	88678.88
MQ(BCC_A2&V,AL,TI;0)	236677.76-37.30*T
MQ(BCC_A2&V,AL,TI,V;0)	6652470.86

6.3 The interdiffusion of the Ti-Al-V system

Using the DICTRA software [41], a set of atomic mobility parameters was obtained; these are listed in Table 11. With these parameters, the direct interdiffusion coefficients were very well reproduced, and the calculated indirect interdiffusion coefficients match the other values with few exceptions, see Tables 12 and 13. The direct interdiffusion coefficients match with other two sources, while the indirect ones are closer to the calculations [156] rather than the experiments [155]. This deviation caused by different methods of obtaining diffusion coefficients has been studied in the work of Huang *et al.* [156].

Table 12: Comparison between calculated and experimental values of interdiffusion coefficients at 1373K ([155]/present work).

x(Al) (at%)	x(V) (at%)	$\tilde{D}^{\mathrm{Ti}}_{\mathrm{Al,Al}}$ (10^{-13}m^2/s)	$\tilde{D}^{\mathrm{Ti}}_{\mathrm{Al,V}}$ (10^{-13}m^2/s)	$\tilde{D}^{\mathrm{Ti}}_{\mathrm{V,V}}$ (10^{-13}m^2/s)	$\tilde{D}^{\mathrm{Ti}}_{\mathrm{V,Al}}$ (10^{-13}m^2/s)
1.3	4.5	1.8/2.3	0.05./-0.17	2.2/3.1	0.50/-0.98
3.3	10.4	1.4/2.3	0.22/-0.21	1.1/2.5	3.3/-1.3
3.8	12.0	2.1//.2	0.006/-0.19	1.7/2.3	0.42/-1.1
5.3	19.0	1.3/1.2	0.21/-0.040	1.2/1.2	0.62/-0.30
3.5	2.5	1.9/3.8	-0.24/-0.54	1.7/3.1	0.28/-0.51
7.1	6.6	1.6/4.4	0.40/-0.55	1.0/2.8	1.5/-0.82
7.5	7.2	2.5/4.3	-0.26/-0.51	1.8/2.7	0.36/-0.81
10.0	12.6	2.2/2.4	0.28/-0.11	1.4/1.5	0.37/-0.30
4.3	1.6	2.8/4.5	0.82/-0.71	2.5/3.0	0.81/-0.31
9.0	3.9	3.1/5.9	1.9/0.028	2.2/1.2	2.4/0.29
9.6	4.3	3.1/5.9	2.1/-0.75	3.0/2.8	2.1/-0.52
12.8	7.5	4.6/4.2	0.44/-0.27	3.3/2.2	4.3/-0.37
4.2	1.7	2.6/4.4	0.62/-0.69	2.1/3.0	0.46/-0.33
9.4	3.3	3.0/6.3	2.0/-0.87	1.2/2.9	0.57/-0.43
10.2	3.5	3.0/6.4	2.3/-0.82	1.3/2.8	0.50/-0.43
13.6	4.8	2.9/5.7	2.6/-0.44	1.0/2.6	0.30/-0.35

With the available mobility parameters, diffusion couple information from the experiment [155] can be reproduced reasonably well. The concentration profiles of two diffusion couples Ti/Ti-16.2Al-10.9V and Ti-9.8Al/Ti-9.9V were obtained versus other works [155, 156] in Figs. 59 and 60. The function lambda given in the graphs is the normalised distance calculated by $\mathrm{distance}/\sqrt{\mathrm{time}}$.

Table 13: Comparison between calculated and experimental values of interdiffusion coefficients at 1473K ([155]/present work/[156]).

x(Al) (at%)	x(V) (at%)	$\tilde{D}^{\mathrm{Ti}}_{\mathrm{Al,Al}}$ ($10^{-13}\mathrm{m}^2/\mathrm{s}$)	$\tilde{D}^{\mathrm{Ti}}_{\mathrm{Al,V}}$ ($10^{-13}\mathrm{m}^2/\mathrm{s}$)	$\tilde{D}^{\mathrm{Ti}}_{\mathrm{V,V}}$ ($10^{-13}\mathrm{m}^2/\mathrm{s}$)	$\tilde{D}^{\mathrm{Ti}}_{\mathrm{V,Al}}$ ($10^{-13}\mathrm{m}^2/\mathrm{s}$)
0.8	4.5	4.9/5.0/4.51	0.60/-0.24/-0.15	7.2/8.9/8.36	1.7/-2.6/-1.7
1.6	9.0	3.8/4.6/3.67	0.82/-0.31/-0.2	4.5/7.6/5.54	0.97/-3.7/-2.6
2.3	13.3	2.5/3.9/2.34	1.4/-0.27/-0.18	4.0/6.3/3.62	2.7/-3.4/-2.71
3.5	18.0	4.5/3.1/2.16	1.6/-0.17/-0.11	2.9/4.4/2.14	2.5/-1.9/-1.72
2.7	3.0	5.6/7.9/5.80	0.060-/0.92/-0.42	6.4/8.5/7.41	0.46/-1.6/-0.86
5.3	5.9	5.7/9.7/5.79	0.49/-1.3/-0.35	5.9/7.5/4.17	1.9/-2.1/-0.55
6.9	8.5	3.3/9.2/5.45	1.3/-1.0/-0.09	3.7/6.5/2.67	3.1/-2.1/0.48
8.1	10.3	4.6/8.1/4.35	-0.19-/0.73/0.11	3.5/5.5/2.01	2.9/-1.7/1.82
3.5	2.3	6.7/9.3/6.62	0.72/-1.3/-0.52	6.2/8.2/7.21	-0.07/-1.1/-0.59
6.4	4.5	7.4/11.8/6.94	1.2/-1.6/-0.39	4.1/7.4/4.19	1.7/-1.6/-0.26
8.5	6.2	6.7/12.1/6.62	3.5/-1.4/-0.08	3.2/6.7/2.71	2.7/-1.6/0.71
9.8	7.4	8.8/11.3/7.67	1.7/-1.1/0.17	3.6/6.0/2.08	2.4/-1.5/1.76
4.5	1.4	9.2/11.2/7.66	4.2/-1.7/-0.65	5.6/7.8/7.09	-0.72/-0.65/-0.32
7.2	2.7	11.0/14.1/8.40	3.3/-2.1/-0.54	2.8/7.2/4.69	-0.005/-1.0/-0.18
10.2	4.1	10.2/15.4/-	9.9/-1.8/-0.11	0.82/6.6/2.83	0.16/-1.1/0.58
11.5	4.8	13.5/15.0/9.97	7.8/-1.5/-0.16	0.97/6.2/2.26	-0.69/-1.1/1.18

Table 14: Symbols for diffusion couples.

Symbols	Diffusion couples
K1	Ti/Ti-6.0Al-21.0V
K2	Ti/Ti-11.2Al-15.8V
K3	Ti/Ti-16.2Al-10.9V
K4	Ti/Ti-20.6Al-5.9V
V1	Ti-5.9Al/Ti-5.0V
V2	Ti-9.8Al/Ti-9.9V
V3	Ti-14.3Al/Ti-14.8V
V4	Ti-19.9Al/Ti-22.9V

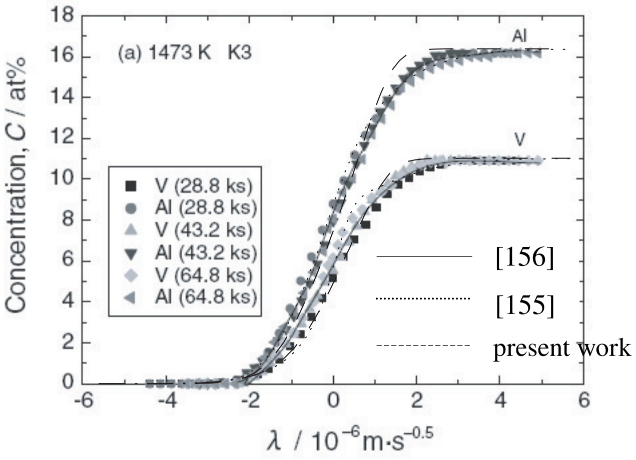

Figure 59: The concentration profile for the diffusion couple Ti/Ti-16.2Al-10.9V annealed at 1473K. The solid line is from experimental work; the dotted line is calculated by Huang *et al.*; the dashed line is obtained from the present work.

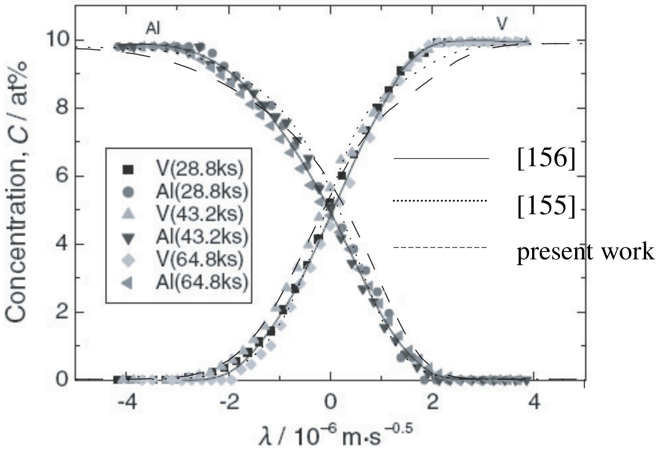

Figure 60: The concentration profile for the diffusion couple Ti-9.8Al/Ti-9.9V annealed at 1473K. The solid line is from experimental work; the dotted line is calculated by Huang *et al.*; the dashed line is obtained from the present work.

Eight diffusion paths were calculated in Figs. 61 and 62, for different diffusion couples annealed at 1473K for 28800s and at 1373K for 72000s, respectively (Note all the symbols standing for diffusion couples are listed in Table 14). The agreement is generally good. For the K1 to K4 diffusion couples, the present calculations are similar with the previous modelling by Huang *et al.* [156], and deviate from the experimental work [155] in a reasonable range. For the V1 and V2 diffusion couples, the calculations can reproduce the experiment very well; while for the V3 and V4 diffusion couples, the deviation of diffusion paths at 1473K still exists, especially for the V4 diffusion couple. In Fig. 61 the solid diffusion path curve of V4 at 1473K drops drastically with increasing V content, which is very different from that at 1373K as shown in Fig. 62 [155]. This is not likely to happen because the diffusion paths of all the other 7 diffusion couples do not change that much when annealing temperature is changed by 100°C. Therefore this indicates a difficulty in the modelling work: although temperature terms have been added to the mobility database, the calculated diffusion path of V4 at 1473K still deviates greatly from the experiment. Another possible reason can also be taken into account: the time taken in the experiments. Considering V4, for example, it took 72,000s at 1373K longer than 28,800s at 1473K, allowing longer time to reach equilibrium, so that the deviation at 1373K in Fig. 62 is much less than 1473K in Fig. 61.

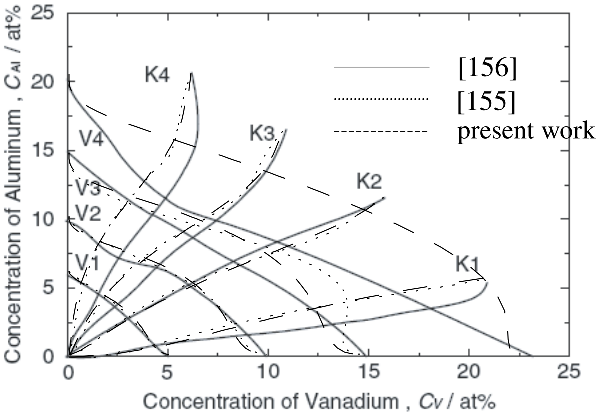

Figure 61: The calculated diffusion paths of different diffusion couples at 1473K for 28,800s. The solid line is from experimental work; the dotted line is calculated by Huang *et al.*; the dashed line is obtained from the present work.

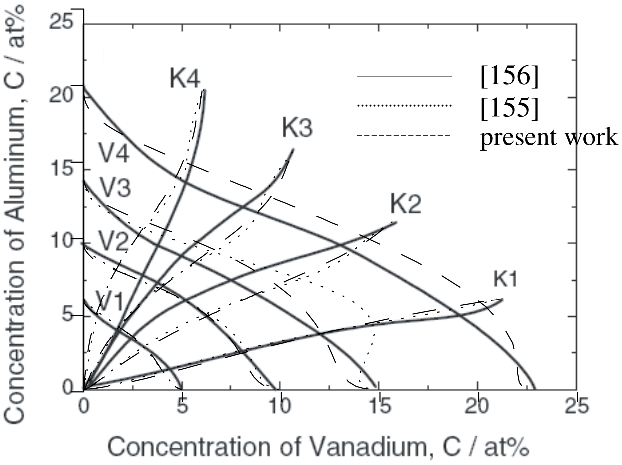

Figure 62: calculated diffusion paths of different diffusion couples at 1373K for 72,000s. The solid line is from experimental work; the dotted line is calculated by Huang *et al.*; the dashed line is obtained from the present work.

6.4 Consideration of substitutional vacancy

Since constitutional vacancies were taken into account in the thermodynamic database (Section 5.5), the corresponding database of atomic mobilities should contain information concerning constitutional vacancies as well. Therefore in this subsection, constitutional vacancies are also added into the atomic mobility database – $(Al,Ti,V,Va\#2)_1$, where the substitutional vacancies (Va#2) are defined separately from the interstitial vacancies (Va by default settings). The basic idea is to make Va_2 hold the same volume as the main element, while keeping Va at zero volume. This treatment [161] allows the mobility parameters in the previous subsection to be kept unchanged. Some new end members as well as interaction parameters are taken to be zero in the new model.

The concentration profiles of two selected diffusion couples in the Ti-Al-V ternary system have been calculated (Ti/Ti-16.2Al-10.9V and Ti-9.8Al/Ti-9.9V). The comparison between calculations and experiments [155] are plotted in Figs. 63 and 64, respectively. Good agreement can be seen in both figures. This is taken to mean that the atomic mobility database is suitable for the phase field simulations which follow.

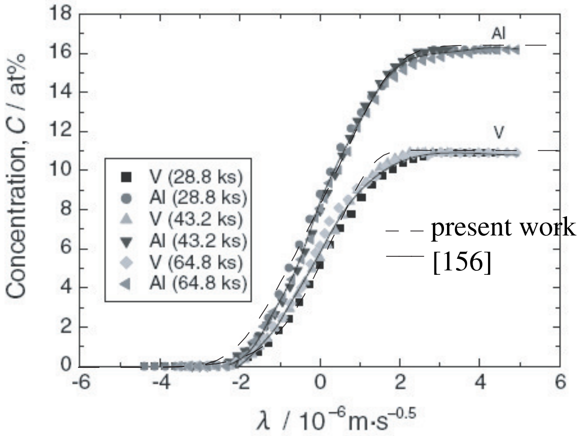

Figure 63: The calculated concentration profiles in diffusion couple Ti/Ti-16.2Al-10.9V with experimental data [155] ($\lambda = \text{distance}/\sqrt{\text{time}}$).The solid line is from experimental work; the dashed line is obtained from the present work.

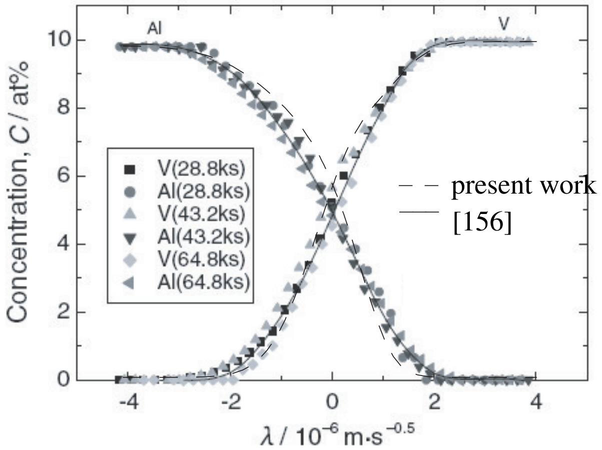

Figure 64: The calculated concentration profiles in diffusion couple Ti-9.8Al/Ti-9.9V with experimental data [155] ($\lambda = \text{distance}/\sqrt{\text{time}}$).The solid line is from experimental work; the dashed line is obtained from the present work.

6.5 Summary

Based upon the thermodynamic driving forces calculated by the thermodynamic databases, interdiffusion in the disordered A2 phase of the ternary Ti–Al–V system has been assessed and optimised. Two sets of parameters describing the atomic mobilities of the disordered A2 phase have been derived, which will be useful for future quantitative models of phase transitions involving this phase. The calculated concentration profiles and diffusion paths match the available experimental information. Additionally, the atomic mobility database has been updated on the basis of the thermodynamic database of Ti-Al-V ternary system taking into account substitutional vacancies. The predicted kinetic properties agree well with the experimental data. The atomic mobilities and diffusivities from the updated database will be used in the following phase-field simulation work to be described in the next chapter.

Chapter 7 Phase-field modelling of the beta-alpha transformation in Ti-6Al-4V

7.1 Introduction

Ti-6Al-4V belongs to the family of α+β Ti alloys, and is commonly used in various fields, particularly the aerospace, marine, chemical processing and medical sectors. It is heat treatable and exhibits an excellent combination of strength, corrosion resistance, weldability and fabricability [10]. Due to its significance, there has been a large amount of research published on its mechanical properties, microstructures and so forth. The phase transformation of β (bcc) to α (hcp) in Ti-6Al-4V is of great importance. Depending on the cooling rate it forms either a martensite structure or Widmanstätten colonies controlled by diffusion, at rather slower cooling rates. Some aspects of the Widmanstätten α transformation are not yet clearly understood, particularly its mechanism of formation. Therefore, in this chapter, phase-field simulations are employed to investigate this microstructure evolution in this well-known alloy.

7.2 Consideration of the existing experimental information

Concerning the mechanism of formation of Widmanstätten α structure (Fig. 65) in Ti alloys, there are currently two diverging opinions. Both groups agree that allotriomorphic α precipitates form first along the grain boundaries between two β grains, but the differences lie in how intergranular α laths form afterwards. A first group believes that formation of inter-granular α laths is due to the instability of the interface between grain boundary α (α_{GB}) and the β matrix [162, 163]. If this view is right, the α phase of Widmanstätten structure (α_W) should have exactly the same orientation as α_{GB}. However, the second group insists that α_W should be nucleated `sympathetically' on the $\alpha_{GB}$ growing subsequently into the β matrix [164, 165]. `Sympathetic nucleation' has been defined as the nucleation of a crystal of α at the α/β boundaries when α and β differ significantly in composition at all stages of its growth [166]. In this case, α_W should hold different variants from those of α_{GB} in order to obtain lower interfacial energy [165].

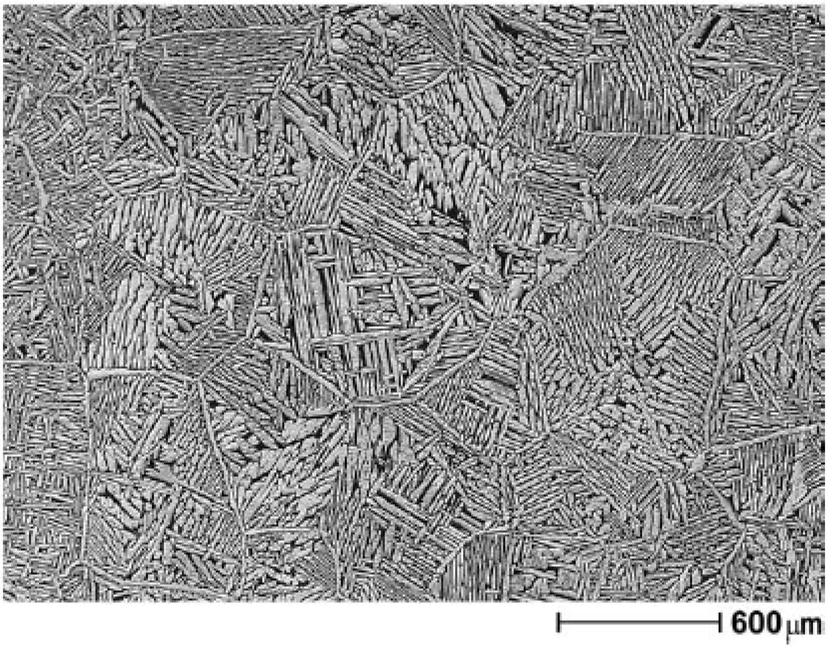

Figure 65: Optical micrograph showing Widmanstätten α in Ti-6Al-4V [167].

Bhattacharyya *et al.* proposed that the growth of α laths on either side of the grain boundary is due to different mechanisms [168]. The side plates on the Burgers side (those holding the Burgers relationship with the β grain) start growing with the same orientation as the grain boundary α; on the non-Burgers side (in which the α grains not holding the

Burgers relationship with the β grain), α laths nucleate on the boundary between the allotriomorphic α and the β matrix, because the grain boundary α has a Burgers orientation relationship with only one of the prior β grains [164]. Some more complicated cases have been investigated by Stanford & Bate [167]: in this case, many orientations of grain boundary α may arise along the grain boundary between two prior β grains; the grain boundary α can form loosely around the Burgers relation in a compromise between adjacent β orientations, and the grain boundary α can restrict the subsequent Widmanstätten growth to the one specific Burgers-related orientation.

It is noteworthy that all of the experimental work mentioned above was based on 2-D cross sections. Undoubtedly, this has contributed to a difficulty in determining the precise formation mechanism of the Widmanstätten structure. For example, as shown in Fig. 66, a schematic illustration is given of the microstructure of α sideplates formed at grain boundary alpha phase, as provided by Furuhara *et al.* [169]. It is proposed that α sideplates (WP_1) in β_1 develop by growth directly from grain boundary alpha (GBA), and α sideplates (WP_2) in β_2 nucleate on the interface between the grain boundary alpha and the matrix. But the related Fig. 67 tells a different story: α sideplates (WP_2) may grow from another grain boundary alpha (GBA_2) which is not shown in the original image. In what follows, both formation mechanisms of the Widmanstätten structure are to be examined by using phase-field simulations.

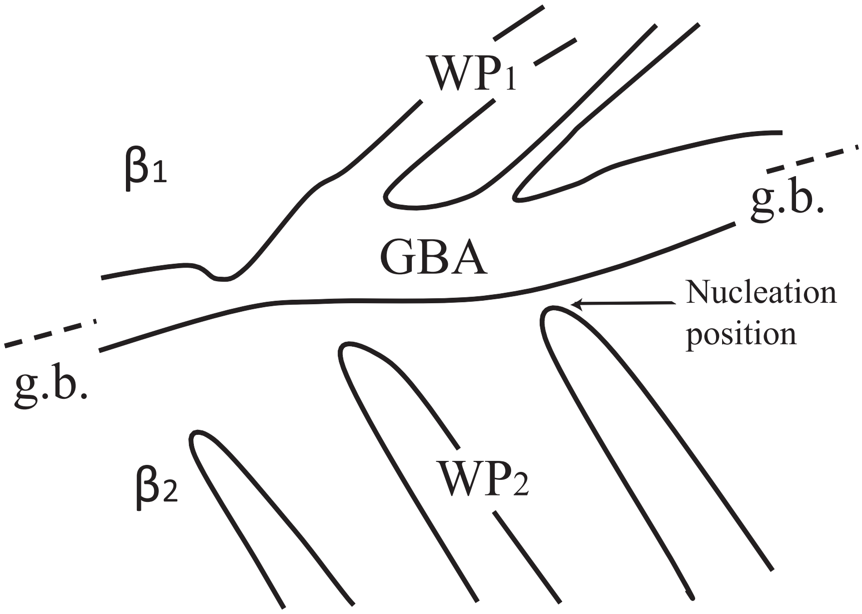

Figure 66: Schematic illustration of microstructure of α sideplates formed at grain boundary alpha [169]. GBA, WP, and g.b. refer to grain boundary alpha, Widmanstätten plate, and grain boundary, respectively.

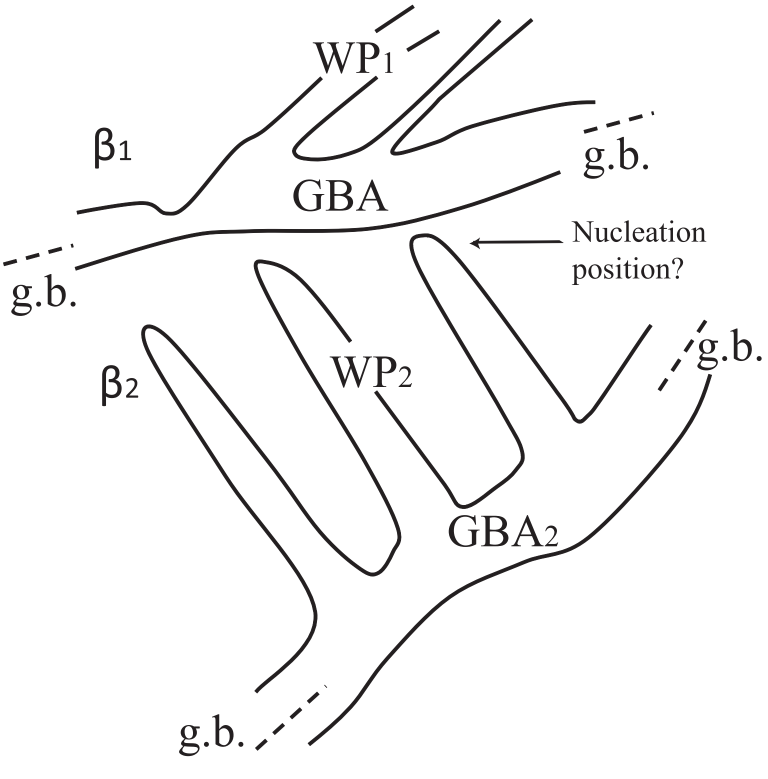

Figure 67: Schematic illustration of another possible mechanism of the formation of α sideplates. GBA, WP, and g.b. refer to grain boundary alpha, Widmanstätten plate, and grain boundary, respectively.

7.3 Microstructure evolution

With the necessary parameters now available (thermodynamics from Chapter 5, atomic mobilities from Chapter 6 and Chen [154], the microstructure evolution during β/α phase transformation has been simulated using the phase-field method implemented in the MICRESS software [96].

Simulations of α precipitation from the β matrix were carried out for Ti-6Al-4V. The simulation domain was discretised using 200×200 square cells with grid spacing of Δx=0.2μm. The interfacial width $\eta_{\alpha\beta}$ in Eq. (28) was chosen to be $4\Delta x$=0.8μm. The simulation was performed consistent with the experimental work [167]: the initial temperature is 983°C, just above the β transus predicted in Chapter 5; the cooling rate is set to be 200°C/hour; the critical undercooling for nucleation was assumed to be 1K since the cooling rate is very low. Facets were used for the α phase in the present work (note that the simulation is 2D, so the y axis is set to be 0 by default). Illustration of two facets was plotted in Fig. 68 – (100) and (001). For each facet, static anisotropy and kinetic anisotropy coefficients are required. Static anisotropy coefficient controls the interfacial energy and kinetic anisotropy controls the interfacial mobility. Taking the vertical grains in Fig. 68 for example, on the (100) facet large static anisotropy coefficient and small kinetic anisotropy coefficient were used; on the (001) facet small static anisotropy coefficient and large kinetic anisotropy coefficient are used. In the present work, no grain orientation has been taken into account; therefore two hypothetic facets were used (100) and (001).

In the present work, various parameters such as the interfacial energy, interfacial mobility and coefficients for the two facts were adjusted for the two mechanisms. The results are discussed as follows to check the rationality of each case.

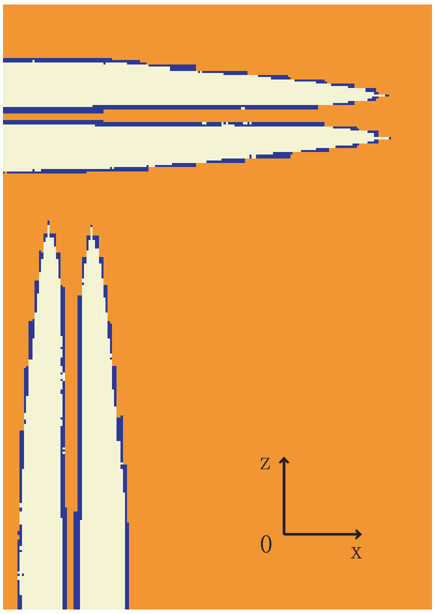

Figure 68: Illustration of the facets used in the present work.

7.3.1 Case I Mullins-Sekerka instability development

Two facets are set for α phase in order to obtain 'needle-shaped' structure: (100) facet with large interfacial mobilities and fairly small interfacial energy, and (001) facet with small interfacial mobilities and normal interfacial energy. The interfacial energy, interfacial mobility and facet coefficients were adjusted. The difficulties of the simulation mainly lie in the appropriate set of facet coefficients; it requires a precise ratio of the coefficients between the two facets in order to simulate a realistic microstructure.

The interfacial energy is set to be $0.10 \mathrm{Jm}^{-2}$; the interfacial mobilities were chosen depending on temperature as shown in Fig. 69. On the (100) facet, static anisotropy coefficient and kinetic anisotropy coefficient are 0.8 and 0.99 respectively; on the (001) facet, the two coefficients are 0.99 and 0.1 respectively. Predicted microstructure evolution is illustrated in Fig. 70. An interface between two β grains is shown in Fig. 70(a). An α grain then forms and grows rapidly along the interface as shown in Fig. 70(b) at 972°C, 200s later. When the temperature decreases to 950°C at 600s, the interface between grain boundary α and β matrix becomes unstable in Fig. 70(c). With continuously cooling down, α phase grows sharply on the (100) facet and forms a 'needle-shaped' structure, as can be seen in Fig. 70(d). As the α/β interfacial mobility is very small at lower temperatures, the α plates virtually stop growing below 900°C. This means the β/α phase transformation is almost complete at around 900°C, which is consistent with the experimental results [170] listed in Table 15. Thus, the microstructure in Fig. 70(d) is considered as the final microstructure after cooling.

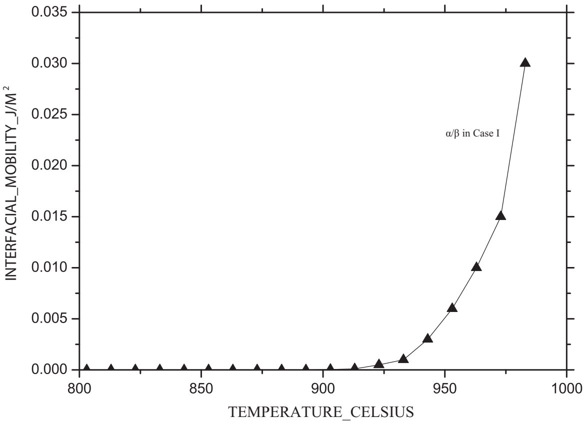

Figure 69: The adjusted interfacial mobilities between α and β phases in case I.

Table 15: The temperatures at which the degree of β/α phase transformation nearly completed during different cooling rates.

Cooling rate (°C/hour)	Temperature (°C)	Source
200	~900	Case I
200	~900	Case II
600	~880	[170, 171]
1200	~860	[170, 171]
1800	~850	[170, 171]
2400	~840	[170, 171]
3000	~830	[171]

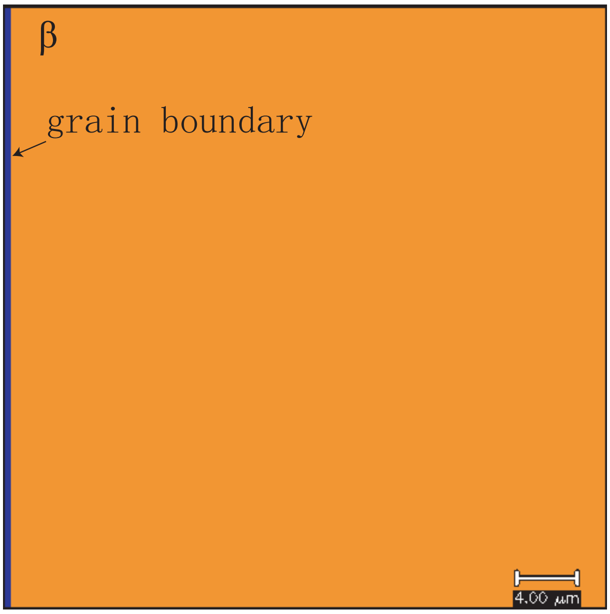

(a) T=983°C, an interface between two β grains (Domain only covers one β grain).

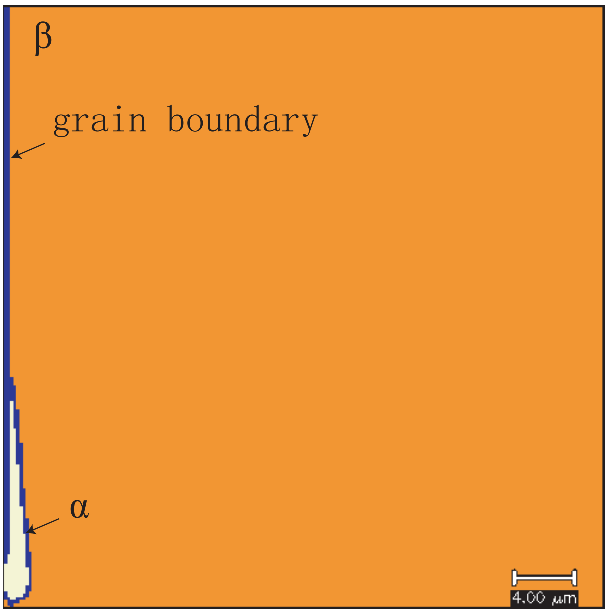

(b) T=972°C, α phase grows rapidly along the grain boundary.

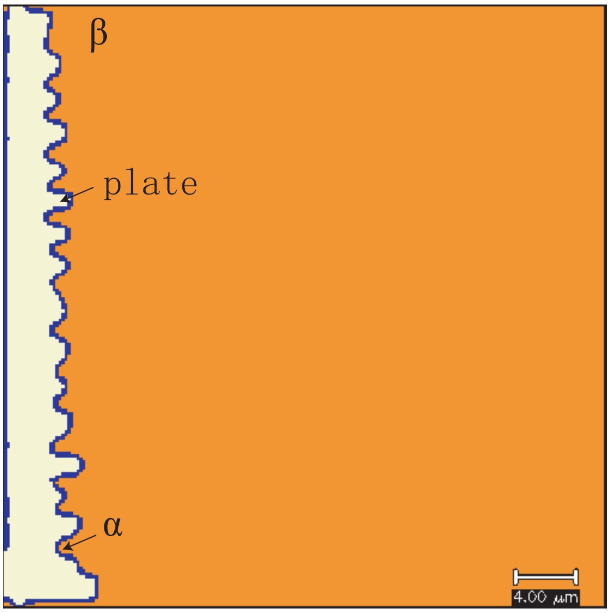

(c) T=950°C, sideplates start to break up from grain boundary α.

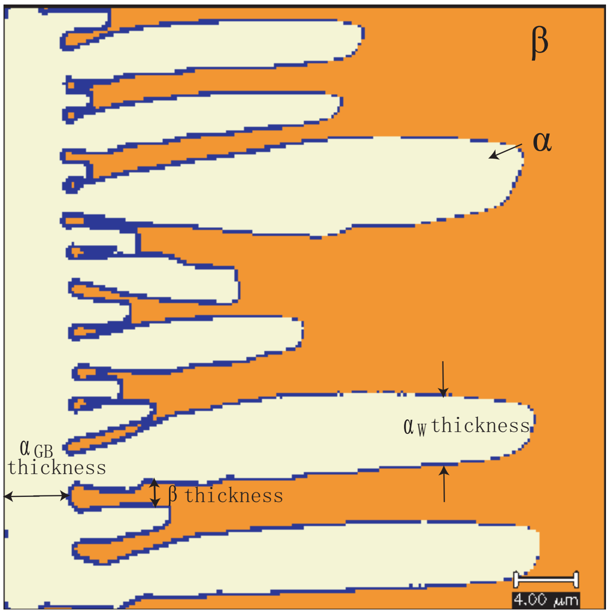

(d) T=909°C, α plates grow further into β matrix and 'needle-shaped' α structure is obtained (this is taken as the final microstructure as the α phase nearly stops growing under 900°C).

Figure 70: Microstructure evolution during slow cooling in Ti-6Al-4V (200°C/hour): Case I Mullins-Sekerka instability development mechanism.

The microstructure obtained in the present work is compared to the experimental work (see Fig. 65 for the microstructure) of Stanford & Bate [167] in what follows. The average thickness of the α phase along the β/β phase boundary is about 3.5μm. As the simulation is limited in one β grain, it is assumed that the grain boundary α phase has the same thickness as the one in the simulation. Thus, the average thickness of the α_{GB} phase is about 7μm, which falls into the region of 5-10μm by the experiment. The main individual Widmanstätten plates have approximate thickness of 2.5-6μm, which is very close to the experimental data 3-7μm. Also the thickness of the β phase which delineates the Widmanstätten plates is less than 1μm, consistent with the experimental observations.

The thickness of Widmanstätten plates is also used to validate the adjusted interfacial mobilities as shown in Table 16. It is very clear that if the variation from the present work is greater than 10%, the thickness of those plates cannot fit the experiment well. It is also worth noting that if the interfacial mobilities are 50% lower than those in the present work, the grain boundary α will not break up into sideplates, and the Widmanstätten structure will not be obtained.

Table 16: The influence of interfacial mobility (J/m^2, see Fig. 69) on the thickness of sideplates.

Source	Thickness of sideplates (μm)
Experiment [167]	3-7
-10% interfacial mobility	1.5-5
present work	2.5-6
+10% interfacial mobility	1.5-5

Furthermore, the α growth kinetics is analysed here. The phase fraction of α at the cooling rate of 200°C/hour is plotted against temperature, and compared to other modelling results in Fig. 71. In the figure, the shape of the curve is classical. It is mainly the grain boundary α_{GB} forming at the temperatures above 950°C, and the α plates forming under 950°C. It is reasonable to find that, at the temperatures above 900°C, the phase fraction in the present work (200°C) is lower than the equilibrium one, and higher than that under any other cooling rate. At lower temperatures, the α phase fraction is lower than usual value. This is because the present simulation is from one grain boundary α and mainly concerning the mechanism of the Widmanstätten structure; the residual β matrix in Fig. 70(d) can be occupied by Widmanstätten α grown from another grain boundary α. Additionally, , usually more α phase can form at lower cooling rate, however the results by 1-D finite element modelling [172] show a contradictory situation (dot-dashed line in Fig. 71).

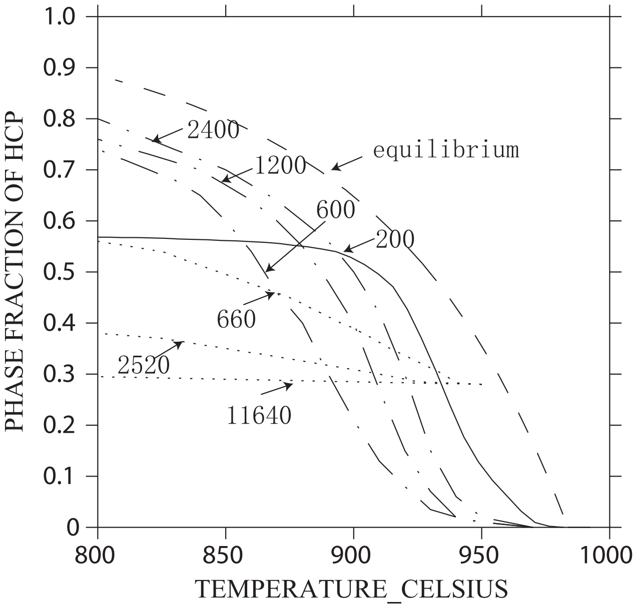

Figure 71: The calculated phase fraction of α during cooling (200°C/hour) is compared to other modelling results (equilibrium calculated from the thermodynamic database in Chapter 5; cooling rates at 600, 1200, 2400°C from [172]; cooling rates at 660, 2520, 11640°C/hour from [173]).

It is also interesting to identify the growth-controlling element in the phase transformation. The calculated compositions of the α and β phases are shown in Fig. 72. It is obvious that there is only very small difference of the Al composition between the two phases, but the difference of the V composition between the two phases is very large. Also when the grain boundary α phase starts to break up sideplates, the composition of the β matrix close to the α/β interface is plotted in Fig. 73. Several places show a kind of 'V concave', and at these places the sideplates grow very fast. Therefore the β/α phase transformation is mainly controlled by V diffusion, consistent with the conclusion from the transmission electron microscopy results [174].

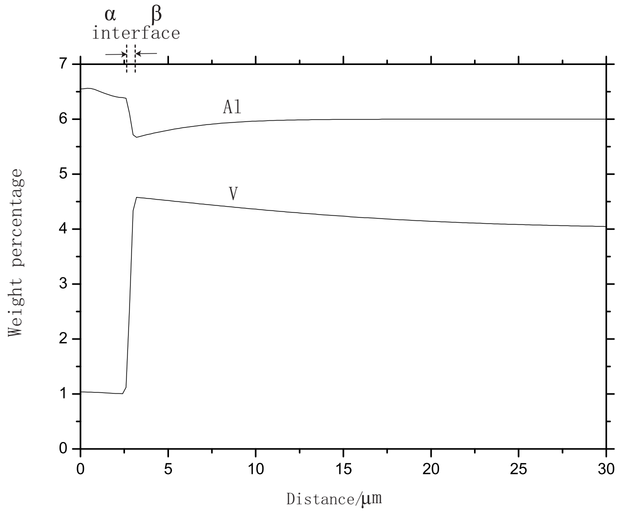

Figure 72: The calculated composition profile of Al and V.

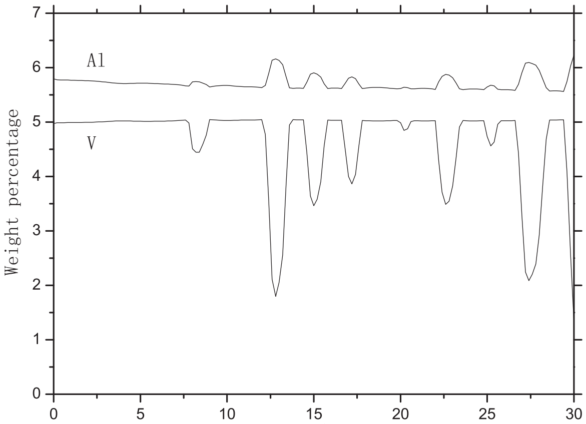

Figure 73: The calculated composition of β matrix along the α/β interface.

The simulation in the present work shows possibilities of Mullins-Sekerka instability development mechanism. This is about to be compared to the sympathetic nucleation mechanism in the later section.

7.3.2 Case II Sympathetic nucleation

Besides the Mullins-Sekerka instability development mechanism, the formation of the sympathetic nucleated α phase has also been simulated in the present work.

Theoretically, the grain boundary α_{GB} phase and Widmanstätten α_W phase are the same phase, but they are practically different phases under the assumption of sympathetic nucleation. The same parameters of thermodynamics and atomic mobility of these two phases are adopted, but different facets are used for them - one facet for α_{GB} and two facets for α_W. For the α_{GB} phase, small interfacial mobility is set for the (100) facet (kinetic anisotropy coefficient being 0.04). For the α_W phase, the same facets are used as α phase in the case I: (100) facet with large interfacial mobility and fairly small interfacial energy (kinetic anisotropy coefficient being 0.99 and static anisotropy coefficient being 0.8), and (001) facet with small interfacial mobility and normal interfacial energy (kinetic anisotropy coefficient being 0.1 and static anisotropy coefficient being 0.99). The interfacial mobilities are adjusted separately for α_{GB} and α_W. The interfacial mobilities of β/α_{GB} and β/α_W on the (100) facet are compared to each other in Fig. 74. Using these adjusted interfacial mobiliteis, the β/α phase transformation has been simulated, which follows.

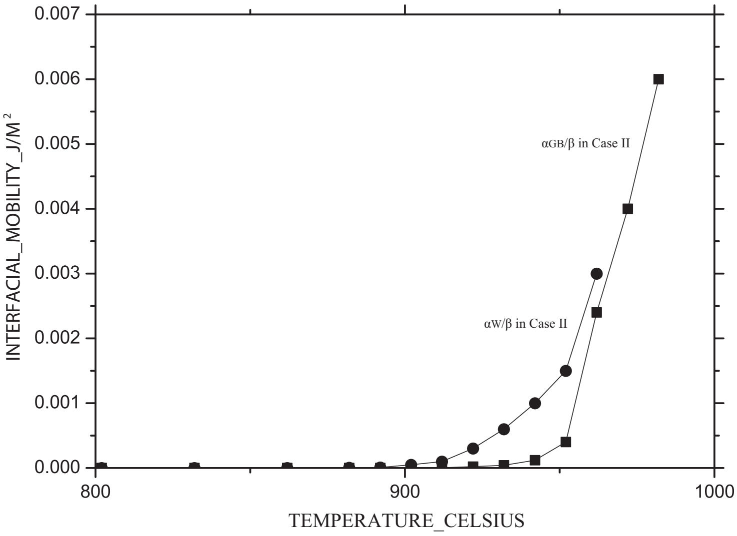

Figure 74: The adjusted interfacial mobilities of β/α_{GB} are compared to those of β/α_W on the (100) direction in case II. Obviously, the interfacial mobilities of β/α_{GB} are lower than those of β/α_W. These interfacial mobilities have been used in the simulation of the β/α phase transformation.

The growth of both α_{GB} and α_W phases is illustrated in Fig. 75. It shows a grain boundary between two β grains in Fig. 75(a). An α_{GB} then grows along the grain boundary at 972°C as shown in Fig. 75(b). At 950°C when the α_{GB} grain covers all the β/β grain boundary, α_W nucleates on the grain boundary between β matrix and α_{GB}, and grow into the matrix plotted in Fig. 75(c). With the growth of α_W, the growth of α_{GB} virtually stops, and the 'needle-shape' structure is also obtained as shown in Fig. 75(d). Again the α_W phase nearly stops growing at around 900°C, which is the same as Case I (see Table 15).

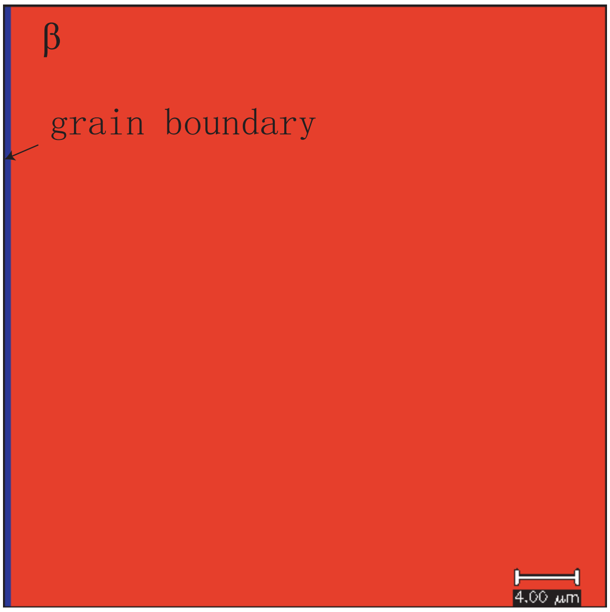

(a) T=983°C, an interface between two β grains (Domain only covers one β grain).

(b) T=972°C, α_{GB} phase grows rapidly along the grain boundary.

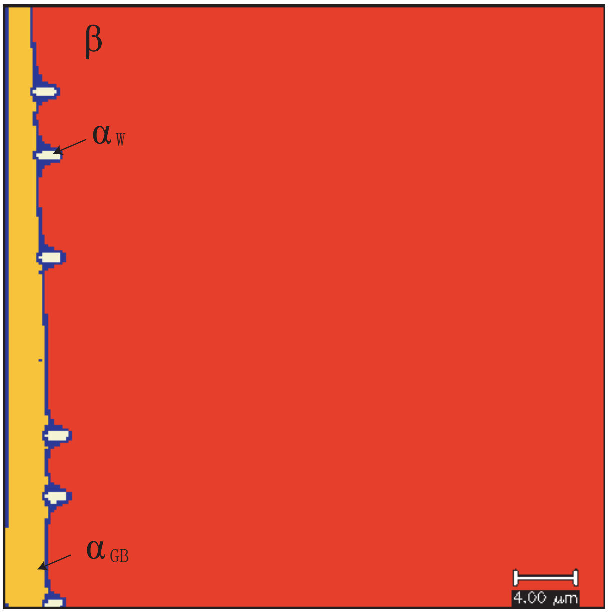

(c) T=950°C, α_W grains start nucleation and growth on the α_{GB}/β interface.

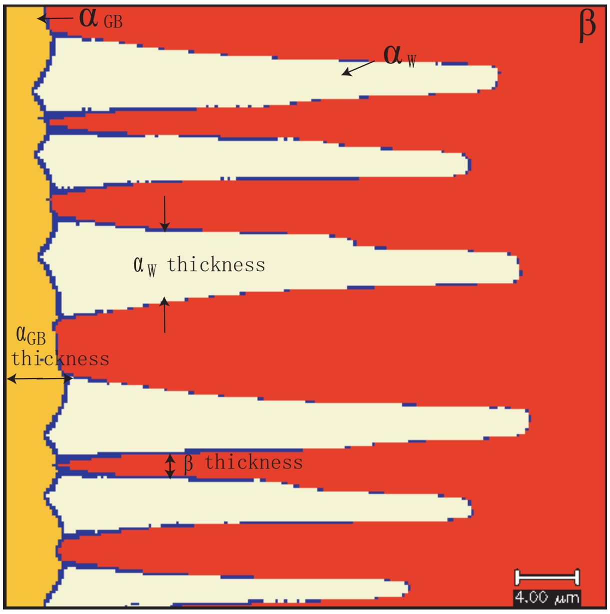

(d) T=909°C, α_W grow further into β matrix and 'needle-shaped' α structure is obtained (this is taken as the final microstructure as the α phase nearly stops growing under 900°C).

Figure 75: Microstructure evolution during slow cooling in the Ti-6Al-4V (200°C/hour): Case II Sympathetic nucleation mechanism.

The simulation results are again consistent with experiment [167]: the thickness of the grain boundary α phase is between 5-10μm; the thickness of the individual Widmanstätten plates is about 2-8μm; the residual β phase between two Widmanstätten plates is less than

3μm thick. The α phase fraction during cooling is also calculated and plotted in Fig. 76. At the temperatures higher than about 950°C, there is only the grain boundary α phase; when the temperature drops down, the α phase fraction is the sum of the grain boundary α_{GB} and Widmanstätten α_W phase. The total α phase fraction is found to be less than that in Case I as shown in Fig. 76. This is because the tip of the α_W plate is very thin, and the interlayer β phase is thick.

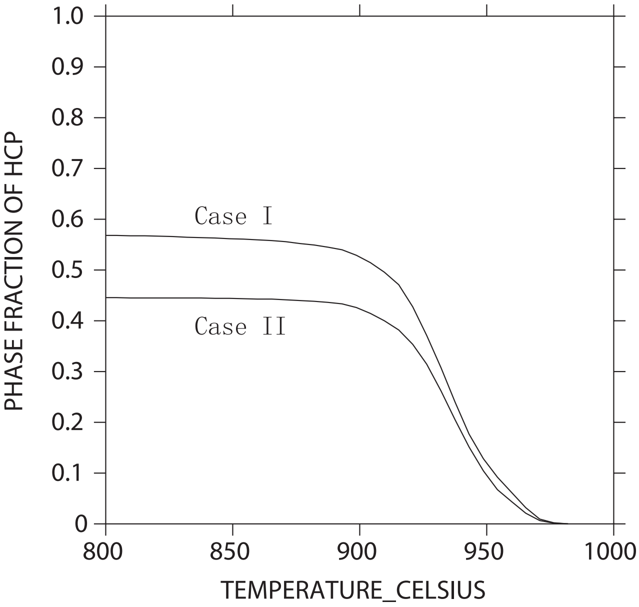

Figure 76: The α phase fraction during cooling (200°C) in case II compared to case I (note the α phase in case II includes the grain boundary α_{GB} phase and the Widmanstätten α_W phase).

Concerning the nucleation rate of the α_W phase, 7 nuclei are set along the 40μm long α_{GB}/β interface. The distance between each of them is 4μm. It is found in the simulation that only 6 of the 7 nuclei can grow into the matrix (see Fig. 75(c)), and the growth of the remaining one is hindered by the high V concentration expelled from the α_W grains on the two sides. If the number of nuclei is less than 6, the α phase fraction will be less than the present work. If the number of nuclei is greater than 10, the thickness of the α_W phase cannot reach a reasonable value.

In addition, it is found that if the interfacial mobility between α_W and β is too low, the moving boundaries between α_W and β would overrun the growth of the Widmanstätten α before they reach certain grain size. Thus, instead of growing further into β matrix, the Widmanstätten α phases stay as 'death points' as shown in Fig. 77. These 'death points' are the interfaces between α_{GB} and α_W in the simulation. Therefore the interfacial mobility between α_W and β must be sufficiently larger (*e.g.* 20% greater) than that between α_{GB} and β along [100] direction.

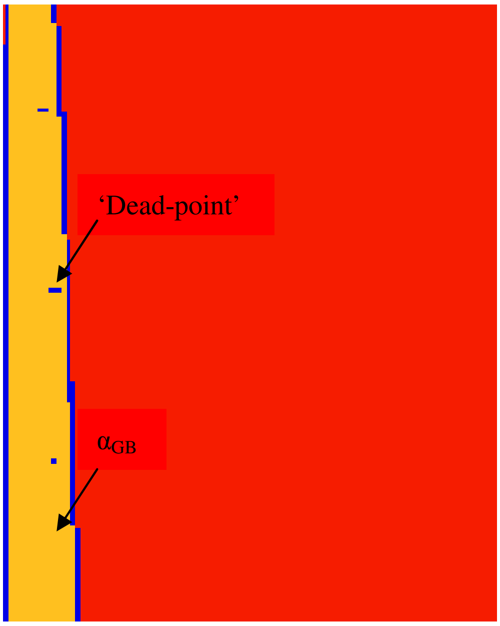

Figure 77: The α_W phases stop growing after nucleation due to low interfacial mobility, and are shown as 'dead points' (The interfaces between α_W and β in the simulation).

7.4 Mechanism of the formation of Widmanstätten α

Through the phase-field modelling, the formation of needle-shaped α phases has been simulated consistent with the two mechanisms. It is worth analysing which mechanism is the more reasonable. It can be readily seen in Fig. 74 that the interfacial mobilities of α_W/β

are much larger than those of α_{GB}/β. As mentioned in the previous subsection, these large interfacial mobilities of α_W/β have been set in order to avoid the sympathetic nuclei overrun by the existing α_{GB}/β phase boundary. However in reality it is more likely that the sympathetic nucleated α_W phase and the existing grain boundary α_{GB} phase have similar interfacial mobilities. This contradiction makes the sympathetic nucleation mechanism unlikely to happen. Moreover, in the definition of sympathetic nucleation, the α phase and the β phase differ significantly in composition at all stages [166], however in Fig. 72 it is clear that the Al compositions in both α and β phases are quite close to each other. This indicates fewer possibilities for sympathetic nucleation.

Orientation of the grain boundary alpha phase also has influence on the growth of the alpha side plates. In the beta grain which does not hold the Burger’s relationship with the grain boundary alpha, the growth of the alpha side plates with Mullins-Sekerka mechanism is likely to be inhibited. However, as illustrated in Fig. 109, the alpha side plates at these positions can be grown from another grain boundary alpha nearby.

Taking into account the above discussion, it can be concluded that Mullins-Sekerka instability development mechanism is more likely to suit the slow cooling procedure in Ti-6Al-4V. As mentioned in Section 7.2, this mechanism indicates that the α_W phase should hold the same orientation as the α_{GB} phase, which is consistent with the EBSD results (see Fig. 78) reported by Stanford & Bate [167].

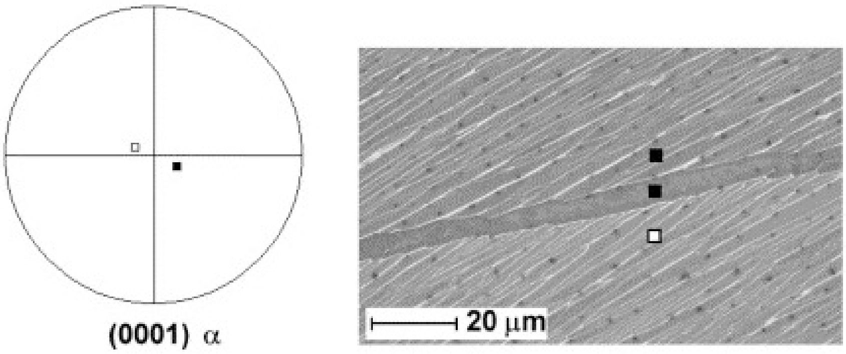

Figure 78: EBSD result shows that the grain boundary α_{GB} hold the same orientation as the α_W phase in the upper grain [167].

Additionally, previous research showing experimental evidence for sympathetic nucleation needs be discussed here [165, 168, 169]. In the experiments, the Ti alloy samples were annealed at certain temperatures roughly 100°C below the corresponding β transus. Under such conditions, the driving force for α precipitation is much greater than that during slow cooling. Large driving force may induce the possibility of sympathetic nucleation during the annealing process. Unfortunately it is difficult to compare the two mechanisms under isothermal condition using the phase-field simulation, mainly because it lacks information for the calculation of the initial sympathetic nucleation time.

7.5 Summary

The Mullins-Sekerka instability development mechanism has been determined for the Widmanstätten α formation during slow cooling in Ti-6Al-4V, by using a phase-field simulation coupled with the CALPHAD approach. Two sets of parameters have been obtained for the two cases (Mullins-Sekerka instability development mechanism and sympathetic nucleation mechanism), which include interfacial energy, interfacial mobility, and facet anisotropy coefficients and so forth. The sensitivity of some important parameters has been analysed, *e.g.* the interfacial mobility and the nucleation rate. It is demonstrated that the simulation results reproduce the microstructural features well, *e.g.* the thickness of grain boundary α phase, the Widmanstätten α phase, and the interlayer β phase. This modelling method can be further extrapolated to other Ti alloy systems and is very useful for tracking the kinetics of β/α phase transformation.

Chapter 8 Conclusions and future work

8.1 Summary of the multi-scale modelling

A framework for multi-scale modelling has been used in the present work. Several methods of modelling have been used: CALPHAD (thermodynamics and atomic mobility), first-principles calculations, and the phase-field simulations. All the models are correlated with each other by the thermodynamic modelling.

Thermodynamic modelling of the high strength, high toughness Ti alloys has been performed as the key part of the whole framework. Experiments were taken to validate the modelling results and further to understand the role of thermal vacancies in microstructural development. The results of first-principles calculations provided the thermodynamic models of the B2 phase with an important physical basis, as well as the concentrations of the thermal vacancies. Some kinetic modelling has also been carried out. The atomic mobilities have been evaluated on the basis of the thermodynamic databases, and the β/α phase transformation has been simulated by using the phase-field method.

The following specific conclusions can be drawn from the present work:

1. The tendency of the sites occupation of the different point defects is predicted in the sublattices of the ordered B2 phase in the Ti-Al system. The anti-site Ti atoms are found to be more stable on the Al site for the Ti-rich alloy, and the substitutional vacancies are favoured on the Ti-site for the Al-rich alloy.
2. The concentration of the constitutional point defects and the thermal point defects

have been calculated at finite temperature. Anti-site Ti defects and Ti vacancies are major constitutional defects in the Ti-rich and the Al-rich alloys, respectively. However, the dominant thermal defects in the corresponding alloys are Ti vacancies and Al anti-site defects.

3. A set of self-consistent thermodynamic parameters have been obtained for the Ti-Al-Cr-V quaternary system on the basis of the parent database. Good agreement has been found between the calculations and the experimental information in the quaternary system and other constitutional binary and ternary systems.
4. The order-disorder transformation temperatures have been calculated for those systems involving the ordered B2 phase. Also the degree of ordering in the Ti-Al binary system has been derived using the thermodynamic database.
5. The composition field has been predicted in the Ti-Al-Cr-V quaternary alloys, which are prone to the ordering reaction. It is found that those alloys with more than 4wt.%Al are likely to have the B2 phase; those alloys with 2-4wt.%Al are not completely ordered, and the ordering effect are not strong; those alloys with less than 2wt.%Al exhibit no ordering. These predictions are consistent with the experimental results.
6. Transmission electron microscopy results show the evidence of the presence of the B2 ordering in the chosen alloys, the compositions of which fall into the predicted B2 phase region in the Ti-Al and Ti-Al-V systems. This again confirms the reliability of the thermodynamic database.

7. Differential scanning calorimetry work suggests the ordering may not have a direct effect of accelerating the kinetics of α precipitating from β matrix, which suggests thermal vacancy might have influence only if combined with C additions.
8. A second set of self-consistent thermodynamic parameters have been optimised for the Ti-Al-V system, taking into account the substitutional vacancies predicted by first-principles calculations. This database has been used for the phase-field simulation.
9. The concentration of the constitutional vacancies at finite temperature has been calculated by using the thermodynamic database. The orders of magnitude of the calculated concentrations of constitutional vacancies are analysed to be within reasonable range.
10. Two sets of atomic mobility parameters have been derived on the basis of the two thermodynamic databases for the Ti-Al-V ternary system. Both fit the experimental data well, and different choices of atomic mobilities are provided for different applications.
11. Two independent sets of parameters have been obtained for (i) Mullins-Sekerka instability development mechanism and (ii) sympathetic nucleation mechanism, including interfacial energy, interfacial mobility, and facet anisotropy coefficients and so forth.
12. The simulation results have been compared to the results from experiment and various analytical models. The features of Widmanstätten structure can be

reproduced. The modelling results are found to be self-consistent.

13. The Mullins-Sekerka instability development mechanism is found to be more reasonable than the sympathetic nucleation mechanism for the β/α phase transformation during slow cooling of Ti-6Al-4V.

8.2 Suggestions to future research

Although the results of the present work are of value and importance, much more research could be carried out. The CALPHAD assessment can be greatly extrapolated into more complex systems to include more elements. Some thermodynamic properties such as enthalpy of formation can be obtained by using first-principles calculations. If computationally possible, the site preference of point defects could be performed for the alloys with compositions deviating greatly from the stoichiometry. Also, the atomic mobilities in the ordered B2 phase can be assessed with available experimental data for diffusion. The phase-field simulation can be later done in the alloy systems involving B2 structure. The suggestions for future research are summarised as follows:

1. First-principles calculations for the site preferences in more complex system, especially ones containing element of C.
2. The binding energy can be predicted by using first-principles calculations in order to evaluate the effect of the thermal vacancy on α precipitation.
3. Thermodynamic extrapolation to the alloy system taking into account further elements such as Sn, Mo, Nb, O, N and C.

4. Synchrotron diffraction can be carried out to determine the B2 phase in Ti alloys at high temperatures.
5. Experiments to determine the diffusion coefficients in the B2 phase although many difficulties can be encountered.
6. With more available data, the database of atomic mobilities can be optimised for the B2 phase.
7. Phase-field simulation could be employed to investigate the microstructure evolution of other high strength, high toughness Ti alloys to obtain a direct view of the effect of refinement by C addition.

References

[1] H. L. Lukas, S. G. Fries and B. Sundman, *Computational Thermodynamics - The Calphad Method*: Cambridge University Press, 2007.

[2] M. Hillert, *phase equilibria, phase diagrams and phase transformations*, 2 ed. New York: Cambridge University Press, 2008.

[3] L. Kaufman, "Computational materials design," *Journal of Phase Equilibria and Diffusion,* vol. 30, pp. 418-428, 2009.

[4] X. Wu, J. del Prado, Q. Li, A. Huang, D. Hu and M. H. Loretto, "Analytical electron microscopy of C-free and C-containing Ti-15-3," *Acta Materialia,* vol. 54, pp. 5433-5448, 2006.

[5] G. H. Narayanan and T. F. Archbold, "Decomposition of the metastable β phase in the all-β alloy Ti-13V-11Cr-3Al," *Materials Transactions A,* vol. 1, pp. 2281-2290, 1970.

[6] H. Fujii and H. G. Suzuki, *Beta Ti Alloys in the 1990's*: TMS, 1990.

[7] P. R. Munroe, "Effect of nickel on vacancy hardening in iron-rich FeAl," *Intermetallics,* vol. 4, pp. 5-11, 1996.

[8] M. A. Morris, O. George and D. G. Morris, "Vacancies, vacancy aggregates and hardening in FeAl," *Materials Science and Engineering A,* vol. 258, pp. 99-107, 1998.

[9] Y. G. Li, P. A. Blenkinsop, M. H. Loretto and N. A. Walker, "Effect of aluminium on ordering of highly stabilised -Ti-V-Cr alloys," *Materials Science and Technology,* vol. 14, pp. 732-737, 1998.

[10] G. Lütjering and J. C. Williams, *Titanium*: Springer, 2003.

[11] W. G. Burgers, "Transition of zirconium crystals," *Physica,* vol. 1, pp. 561-586, 1934.

[12] J. B. Newkirk and A. H. Geisler, "Crystallographic aspects of the beta to alpha transformation in titanium," *Acta Metallurgica,* vol. 1, pp. 370-371, 373-374, 1953.

[13] C. Leyens and M. Peters, *Titanium and Titanium Alloys: Fundamentals and Applications*. Weinheim: WILEY-VCH, 2003.

[14] M. A. Krivoglaz and A. Smirnov, *The theory of order-disorder in alloys*. London: Macdonald, 1964.

[15] N. Saunders and A. P. Miodownik, *CALPHAD (Calculation of Phase Diagrams): A Comprehensive Guide*: Elesevier, 1998.

[16] R. Kainuma, M. Palm and G. Inden, "Solid-phase equilibria in the Ti-rich part of the Ti---Al system," *Intermetallics,* vol. 2, pp. 321-332, 1994.

[17] H. Okamoto and T. B. Massalski, "Thermodynamically Improbable Phase Diagrams," *Journal of Phase Equilibria,* vol. 12, pp. 148-168, 1991.

[18] I. Ohnuma, Y. Fujita, H. Mitsui, K. Ishikawa, R. Kainuma and K. Ishida, "Phase equilibria in the Ti-Al binary system," *Acta Materialia,* vol. 48, pp. 3113-3123, 2000.

[19] T. Helander and O. Tolochko, "An experimental investigation of possible B2-ordering in the Al-Cr system," *Journal of Phase Equilibria,* vol. 20, pp. 57-60, 1999.

[20] A. Hellwig, "Experimental investigation of the constitution of Al-Nb-Ti system," PhD Thesis, University of Dortmund, Germany, 1990.

[21] H. Nakamura, M. Takeyama, Y. Yamabe and M. Kikuchi, "Phase equilibria in TiAl alloys containing 10 and 20 at.% Nb at 1473 K," *Scripta metallurgica et materialia,* vol. 28, pp. 997-1002, 1993.

[22] K. Das and S. Das, "Order-disorder transformation of the body centered cubic phase in the Ti-Ai-X(X = Ta, Nb, or Mo) system," *Journal of Materials Science,* vol. 38, pp. 3995-4002, 2003.

[23] T. Ahmed and H. M. Flower, "Partial isothermal sections of Ti-Al-V ternary diagram," *Materials*

Science and Technology, vol. 10, pp. 272-288, 1994.

[24] G. Shao, P. Tsakiropoulos and A. P. Miodownik, "Ordering and decomposition of the beta phase in melt-spun $TiAl_{1-x}V_x$ alloys," *Materials Science and Engineering A,* vol. 216, pp. 1-10, 1996.

[25] G. Shao and P. Tsakiropoulos, "Ultra-thin twin plates and growth domains in the phase as a product of the B2 phase decomposition in Ti-40 at.% Al-10 at.% V," *Philosophical Magazine A,* vol. 75, pp. 657-676, 1997.

[26] G. Shao, "An ordered long-period superlattice structure of the B2 lattice," *Applied Physics Letters,* vol. 74, pp. 2643-2645, 1999.

[27] M. Kimura, K. Hashimoto and H. Morikawa, "Study on phase stability in Ti-Al-X systems at high temperatures," in *High Temperature Aluminides and Intermetallics. Second International ASM Conference, 16-19 Sept. 1991*, Switzerland, 1992, pp. 54-59.

[28] R. Kainuma, I. Ohnuma, K. Ishikawa and K. Ishida, "Stability of B2 ordered phase in the Ti-rich portion of Ti-Al-Cr and Ti-Al-Fe ternary systems," *Intermetallics,* vol. 8, pp. 869-875, 2000.

[29] T. J. Jewett and M. Dahms, "Investigation of the β-$Ti(Cr,Al)_2$ phase at 800°C and 1000°C," *Scripta metallurgica et materialia,* vol. 32, pp. 1533-1539, 1995.

[30] T. J. Jewett, B. Ahrens and M. Dahms, "Stability of TiAl in the Ti-Al-Cr system," *Materials Science and Engineering A,* vol. A225, pp. 29-37, 1997.

[31] A. Grytsiv, P. Rogl, H. Schmidt and G. Giester, "Constitution of the Ternary System Al-Ru-Ti (Aluminum-Ruthenium-Titanium)," *Journal of Phase Equilibria,* vol. 24, pp. 511-527, 2003.

[32] M. H. Loretto, D. Hu and Y. G. Li, "Microstructural studies on some ordered Ti-based alloys," *Intermetallics,* vol. 8, pp. 1243-1249, 2000.

[33] M. H. Loretto, D. Horspool, R. Botten, D. Hu, Y. G. Li, D. Srivastava, R. Sharman and X. Wu, "Controlling the properties of some ordered Ti-based alloys," *Materials Science and Engineering A,* vol. 329-331, pp. 1-6, 2002.

[34] L. Kaufman and H. Bernstein, *Computer Calculation of Phase Diagram: With Special Reference to Refractory Metals*. New York: Academic Press, 1970.

[35] L. Kaufman, "The lattice stability of metals--I. Titanium and zirconium," *Acta Metallurgica,* vol. 7, pp. 575-587, 1959.

[36] P. J. Spencer, "A brief history of CALPHAD," *Calphad,* vol. 32, pp. 1-8, 2008.

[37] J. J. van Laar, "The enamel- or congealment curves on the binary systems, when the solid phases of a mixture (amorphe solid solutions or mixed crystals) of the two components," *Zeitschrift fur Physikalische Chemie,* vol. 63, pp. 216-253, Jun 1908.

[38] J. J. van Laar, "The melting- and solidifying curves in binary systems, if the solid phase is an alloy (amorphous solid solution or mixed crystals) of both components," *Zeitschrift fur Physikalische Chemie,* vol. 64, pp. 257-297, Sep 1908.

[39] I. Ansara, N. Dupin, H. L. Lukas and B. Sundman, "Thermodynamic assessment of the Al-Ni system," *Journal of Alloys and Compounds,* vol. 247, pp. 20-30, 1997.

[40] N. Dupin and I. Ansara, "On the sublattice formalism applied to the B2 phase," *Zeitschrift fuer Metallkunde/Materials Research and Advanced Techniques,* vol. 90, pp. 76-85, 1999.

[41] J. O. Andersson, T. Helander, L. Hoglund, P. F. Shi and B. Sundman, "Thermo-Calc DICTRA, computational tools for materials science," *Calphad,* vol. 26, pp. 273-312, 2002.

[42] W. Cao, S. L. Chen, F. Zhang, K. Wu, Y. Yang, Y. A. Chang, R. Schmid-Fetzer and W. A. Oates, "PANDAT software with PanEngine, PanOptimizer and PanPrecipitation for multi-component phase

diagram calculation and materials property simulation," *Calphad,* vol. 33, pp. 328-342, 2009.

[43] H. Lukas and S. Fries, "Demonstration of the use of “BINGSS” with the Mg-Zn system as example," *Journal of Phase Equilibria,* vol. 13, pp. 532-542, 1992.

[44] G. Eriksson and K. Hack, "ChemSage. A computer program for the calculation of complex chemical equilibria," *Metallurgical transactions. B, Process metallurgy,* vol. 21, pp. 1013-1023, 1990.

[45] U. R. Kattner, "The thermodynamic modeling of multicomponent phase equilibria," *JOM,* vol. 49, pp. 14-19, 1997.

[46] D. K. Benerjee, M. T. Samonds, U. R. Kattner and W. J. Boettinger, in *the 4th Decennial International Conference on Solidification Processing* University of Sheffield, UK, 1997, pp. 354-357.

[47] J. S. Kirkaldy, B. A. Thomson and E. A. Baganis, "Prediction of multicomponent equilibrium and transformation diagrams for low alloy steels," in *Hardenability Concepts with Applications to Steel,*, J. S. Kirkaldy and D. V. Doane, Eds., ed Chicago, IL, USA: Metall Soc of AIME, 1978, pp. 82-125.

[48] H. K. D. H. Bhadeshia, "Thermodynamic analysis of isothermal transformation diagrams," *Metal science,* vol. 16, pp. 159-165, 1982.

[49] M. Enomoto, "Prediction of TTT-diagram of proeutectoid ferrite reaction in iron alloys from diffusion growth theory," *ISIJ International,* vol. 32, pp. 297-305, 1992.

[50] J. S. Kirkaldy and E. A. Baganis, "Thermodynamic prediction of the Ae3 temperature of steels with additions of Mn, Si, Ni, Cr, Mo, Cu," *Metallurgical Transactions A,* vol. 9, pp. 495-501, 1978.

[51] K. Hashiguchi, J. S. Kirkaldy, T. Fukuzumi and V. Pavaskar, "Prediction of the equilibrium, paraequilibrium and no-partition local equilibrium phase diagrams for multicomponent Fe-C base alloys," *Calphad,* vol. 8, pp. 173-186.

[52] M. Enomoto and H. I. Aaronson, "Calculation of [alpha] + [gamma] phase boundaries in Fe-C-X systems from the central atoms model," *Calphad,* vol. 9, pp. 43-58, 1985.

[53] A. A. B. Sugden and H. K. D. H. Bhadeshia, "Thermodynamic estimation of liquidus, solidus, Ae3 temperatures, and phase compositions for low alloy multicomponent steels," *Materials Science and Technology,* vol. 5, pp. 977-984, 1989.

[54] A. Kroupa and J. Kirkaldy, "Computed multicomponent phase diagrams for hardenability (H) and HSLA steels with application to the prediction of microstructure and mechanical properties," *Journal of Phase Equilibria,* vol. 14, pp. 150-161, 1993.

[55] J. Agren, "Computer-simulations of diffusional reactions in complex steels," *ISIJ International,* vol. 32, pp. 291-296, 1992 1992.

[56] D. Marx and J. Hutter, *Ab initio molecular dynamics: Basic theory and advanced methods*. New York: Cambridge University Press, 2009.

[57] W. F. van Gunsteren and H. J. C. Berendsen, "Computer simulation of molecular dynamics. Methodology, applications, and perspectives in chemistry," *Angewandte Chemie (International Edition in English),* vol. 29, pp. 992-1023, 1990.

[58] C. G. Gray and K. E. Gubbins, *Theory of Molecular Fluids* vol. 1. New York: Oxford University Press, 1984.

[59] G. C. Schatz, "The analytical representation of electronic potential-energy surfaces," *Reviews of Modern Physics,* vol. 61, pp. 669-688, 1989.

[60] M. Sprik, "Effective pair potentials and beyond," in *Proceedings of NATO ASI on New Perspectives in Computer Simulation, 14-24 Sept. 1992*, Dordrecht, Netherlands, 1993, pp. 211-259.

[61] A. J. Stone, *The Theory of Intermolecular Forces*. Oxford: Clarendon Press, 2002.

[62] M. C. Payne, M. P. Teter, D. C. Allan, T. A. Arias and J. D. Joannopoulos, "Iterative minimization techniques for ab initio total-energy calculations: molecular dynamics and conjugate gradients," *Reviews of Modern Physics,* vol. 64, pp. 1045-1097, 1992.

[63] D. K. Remler and P. A. Madden, "Molecular dynamics without effective potentials *via* the Car-Parrinello approach," *Molecular Physics,* vol. 70, pp. 921-966, 1990.

[64] J. F. Shackelford, *Introduction to Materials Science for Engineers*, 7 ed. New Jersey, USA: Pearson Education International, 2009.

[65] J. Hafner, "Ab-initio simulations of materials using VASP: density-functional theory and beyond," *Journal of Computational Chemistry,* vol. 29, pp. 82-116, 2008.

[66] A. Baldereschi, "Mean-value point in the Brillouin zone," *Physical Review B,* vol. 7, pp. 5212-5215, 1973.

[67] D. J. Chadi and M. L. Cohen, "Special points in the Brillouin zone," *Physical Review B,* vol. 8, pp. 5747-5753, 1973.

[68] H. J. Monkhorst and J. D. Pack, "Special points for Brillouin-zone integrations," *Physical Review B* vol. 13, pp. 5188-5192, 1976.

[69] M. I. McMahon, O. Degtyareva and R. J. Nelmes, "Ba-IV-type incommensurate crystal structure in group-V metals," *Physical Review Letters,* vol. 85, pp. 4896-4899, 2000.

[70] U. Haussermann, K. Soderberg and R. Norrestam, "Comparative study of the high-pressure behavior of As, Sb, and Bi," *Journal of the American Chemical Society,* vol. 124, pp. 15359-15367, 2002.

[71] S. Ogata, J. Li and S. Yip, "Ideal pure shear strength of aluminum and copper," *Science,* vol. 298, pp. 807-811, 2002.

[72] T. Li, J. W. Morris, Jr. and D. C. Chrzan, "Ideal tensile strength of B2 transition-metal aluminides," *Physical Review B,* vol. 70, pp. 54107-50112, 2004.

[73] M. Jahnatek, M. Krajci and J. Hafner, "Response of trialuminides to [110] uniaxial loading: an ab initio study for Al_3(Sc,Ti,V)," *Physical Review B,* vol. 76, pp. 14110-14128, 2007.

[74] P. Souvatzis, O. Eriksson and M. I. Katsnelson, "Anomalous thermal expansion in alpha-titanium," *Physical Review Letters,* vol. 99, pp. 015901-015905, 2007.

[75] P. Souvatzis and O. Eriksson, "Ab initio calculations of the phonon spectra and the thermal expansion coefficients of the 4d metals," *Physical Review B,* vol. 77, pp. 024110-024116, 2008.

[76] G. Kresse and J. Hafner, "Ab initio molecular-dynamics simulation of the liquid-metal-amorphous-semiconductor transition in germanium," *Physical Review B,* vol. 49, pp. 14251-14269, 1994.

[77] L. Gao, W. Ji, Y. B. Hu, Z. H. Cheng, Z. T. Deng, Q. Liu, N. Jiang, X. Lin, W. Guo, S. X. Du, W. A. Hofer, X. C. Xie and H. J. Gao, "Site-Specific Kondo Effect at Ambient Temperatures in Iron-Based Molecules," *Physical Review Letters,* vol. 99, pp. 106402-106405, 2007.

[78] L. E. Ramos, E. Degoli, G. Cantele, S. Ossicini, D. Ninno, J. Furthmuller and F. Bechstedt, "Structural features and electronic properties of group-III-, group-IV-, and group-V-doped Si nanocrystallites," *Journal of Physics: Condensed Matter,* vol. 19, pp. 466211-466223, 2007.

[79] G. Kresse, M. Schmid, E. Napetschnig, M. Shishkin, L. Kohler and P. Varga, "Materials Science: Structure of the ultrathin aluminum oxide film on NiAl(110)," *Science,* vol. 308, pp. 1440-1442, 2005.

[80] J. K. Nrskov, M. Scheffler and H. Toulhoat, "Density functional theory in surface science and

heterogeneous catalysis," *MRS Bulletin,* vol. 31, pp. 669-674, 2006.

[81] S. M. Opalka, T. H. Vanderspurt, R. Radhakrishnan, Y. She and R. R. Willigan, "Design of water gas shift catalysts for hydrogen production in fuel processors," *Journal of Physics,* vol. 20, pp. 064237-064249, 2008.

[82] L.-Q. Chen, "Phase-field models for microstructure evolution," *Annual Review of Materials Science,* vol. 32, pp. 113-140, 2002.

[83] W. J. Boettinger, J. A. Warren, C. Beckermann and A. Karma, "Phase-field simulation of solidification," *Annual Review of Materials Science,* vol. 32, pp. 163-194, 2002.

[84] L. V. Mikheev and A. A. Chernov, "Mobility of a diffuse simple crystal-melt interface," *Journal of Crystal Growth,* vol. 112, pp. 591-596, 1991.

[85] I. Steinbach, "Phase-field models in materials science," *Modelling and Simulation in Materials Science and Engineering,* vol. 17, pp. 073001-073031, 2009.

[86] J. S. Rowlinson, "Translation of J.D. van der Waals' `The thermodynamic theory of capillarity under the hypothesis of a continuous variation of density'," *Journal of Statistical Physics,* vol. 20, pp. 197-244, 1979.

[87] L. D. Landau and I. M. Khalatikow, *The selected Works of L.D. Landau (Engl. transl.).* Oxford: Pergamon, 1963.

[88] M. Hillert, "A theory of nucleation for solid solutions," D.Sc Thesis, MIT, Cambridge, MA, 1956.

[89] J. W. Cahn and J. E. Hilliard, "Free energy of a nonuniform system. I.Interfacial free energy," *Journal of Chemical Physics,* vol. 28, pp. 258-267, 1958.

[90] J. W. Cahn and J. E. Hilliard, "Free energy of a nonuniform system. III. Nucleation in a two-component incompressible fluid," *Journal of Chemical Physics,* vol. 31, pp. 688-699, 1959.

[91] J. Tiaden, B. Nestler, H. J. Diepers and I. Steinbach, "The multiphase-field model with an integrated concept for modelling solute diffusion," *Physica D,* vol. 115, pp. 73-86, 1998.

[92] J. Eiken, B. Bottger and I. Steinbach, "Multiphase-field approach for multicomponent alloys with extrapolation scheme for numerical application," *Physical Review E,* vol. 73, pp. 66122-66130, 2006.

[93] D. Fan and L. Q. Chen, "Microstructural evolution and grain growth kinetics in two-phase silids with auqdrijunctions," in *Mathematics of Microstructure Evolution*, L. Q. Chen*, et al.*, Eds., ed Warrendale, PA: TMS, 1996, pp. 215-223.

[94] D. Fan and L. Q. Chen, "Computer simulation of grain growth using continuum field model," *Acta Materialia,* vol. 45, pp. 611-622, 1997.

[95] R. Kobayashi, J. A. Warren and W. C. Carter, "Mathematical models for solidification and grain boundary formation," *Ach-Models in Chemistry,* vol. 135, pp. 287-295, 1998 1998.

[96] MICRESS. Available: http://www.micress.de

[97] Y. Nomura, S. Minamoto and S. Nomoto, "Simulations of solidification in Sn-3Ag-0.5Cu alloys by the multi-phase-field method," *ISIJ International,* vol. 50, pp. 1920-1924, 2010.

[98] L. Zhang, I. Steinbach and Y. Du, "Phase-field simulation of diffusion couples in the Ni-Al system," *International Journal of Materials Research,* vol. 102, pp. 371-380, 2011.

[99] J. Rudnizki, B. Bottger, U. Prahl and W. Bleck, "Phase-field modeling of austenite formation from a ferrite plus pearlite microstructure during annealing of cold-rolled dual-phase steel," *Metallurgical and Materials Transactions A,* vol. 42, pp. 2516-2525, 2011.

[100] P. E. A. Turchi, I. A. Abrikosov, B. Burton, S. G. Fries, G. Grimvall, L. Kaufman, P. Korzhavyi, V.

Rao Manga, M. Ohno, A. Pisch, A. Scott and W. Zhang, "Interface between quantum-mechanical-based approaches, experiments, and CALPHAD methodology," *Calphad,* vol. 31, pp. 4-27, 2007.

[101] A. T. Dinsdale, "SGTE data for pure elements," *Calphad,* vol. 15, pp. 317-425, 1991.

[102] O. Redlich and A. T. Kister, "Algebraic Representation of Thermodynamic Properties and the Classification of Solutions," *Industrial & Engineering Chemistry,* vol. 40, pp. 345-348, 1948.

[103] M. Hillert, "The compound energy formalism," *Journal of Alloys and Compounds,* vol. 320, pp. 161-176, 2001.

[104] M. Hillert and L. I. Staffanson, "Regular Solution Model for Stoichiometric Phases and Ionic Melts," *Acta Chemica Scandinavica,* vol. 24, pp. 3618-3626, 1970.

[105] J. O. Andersson and J. Agren, "Models for numerical treatment of multicomponent diffusion in simple phases," *Journal of Applied Physics,* vol. 72, pp. 1350-1355, 1992.

[106] B. Jonsson, "Assessment of the mobility of carbon in fcc C-Cr-Fe-Ni alloys," *Zeitschrift fur Metallkunde,* vol. 85, pp. 502-509, 1994.

[107] I. Steinbach, B. Bottger, J. Eiken, N. Warnken and S. G. Fries, "CALPHAD and phase-field modeling: A successful liaison," *Journal of Phase Equilibria and Diffusion,* vol. 28, pp. 101-106, Feb 2007.

[108] I. Steinbach and F. Pezzolla, "A generalized field method for multiphase transformations using interface fields," *Physica D,* vol. 134, pp. 385-393, 1999.

[109] J. S. Kirkaldy and D. J. Young, *Diffusion in the condensed state*. London, UK: The Institute of Metals, 1987.

[110] D. Vanderbilt, "Soft self-consistent pseudopotentials in a generalized eigenvalue formalism," *Physical Review B,* vol. 41, pp. 7892-7895, 1990.

[111] M. Hagen and M. W. Finnis, "Point defects and chemical potentials in ordered alloys," *Philosophical Magazine A,* vol. 77, pp. 447-64, 1998.

[112] V. T. Witusiewicz, A. A. Bondar, U. Hecht, S. Rex and T. Y. Velikanova, "The Al-B-Nb-Ti system. III. Thermodynamic re-evaluation of the constituent binary system Al-Ti," *Journal of Alloys and Compounds,* vol. 465, pp. 64-77, 2008.

[113] R. R. Zope and Y. Mishin, "Interatomic potentials for atomistic simulations of the Ti-Al system," *Physical Review B,* vol. 68, pp. 241021-2410213, 2003.

[114] R. E. Watson and M. Weinert, "Transition-metal aluminide formation: Ti, V, Fe, and Ni aluminides," *Physical Review B,* vol. 58, pp. 5981-5988, 1998.

[115] G. Ghosh and M. Asta, "First-principles calculation of structural energetics of Al-TM (TM = Ti, Zr, Hf) intermetallics," *Acta Materialia,* vol. 53, pp. 3225-3252, 2005.

[116] J. L. Murray, "Calculation of the titanium-aluminium phase diagram," *Metallurgical Transactions A,* vol. 19, pp. 243-247, 1988.

[117] A. Lozovoi, K. Ponomarev, Y. Vekilov, P. Korzhavyi and I. Abrikosov, "First-principles investigation of thermal point defects in B2 NiAl," *Physics of the Solid State,* vol. 41, pp. 1494-1499, 1999.

[118] F. Zhang, F. Y. Xie, S. L. Chen, Y. A. Chang, D. Furrer and V. Venkatesh, "Predictions of titanium alloy properties using thermodynamic modeling tools," *Journal of Materials Engineering and Performance,* vol. 14, pp. 717-721, 2005.

[119] J. L. Murray, "Al-Ti (Aluminum-Titanium)," in *Binary Alloy Phase Diagram*. vol. 1, T. B. Massalski, Ed., 2 ed: TMS, 1990, pp. 225-227.

[120] H. Okamoto, "Al-Ti (aluminum-titanium)," *Journal of Phase Equilibria,* vol. 14, pp. 120-121, 1993.

[121] H. Okamoto, "Al-Ti (aluminum-titanium)," *Journal of Phase Equilibria,* vol. 21, p. 311, 2000.

[122] V. Raghavan, "Al-Ti (aluminum-titanium)," *Journal of Phase Equilibria and Diffusion,* vol. 26, pp. 171-172, 2005.

[123] J.-C. Schuster and M. Palm, "Reassessment of the binary aluminum-titanium phase diagram," *Journal of Phase Equilibria and Diffusion,* vol. 27, pp. 255-277, 2006.

[124] R. D. Shull and J. P. Cline, "High temperature X-ray diffractometry of Ti-Al alloys," *High temperature science,* vol. 26, pp. 95-117, 1988.

[125] J. Murray, "The Al-Cr (aluminum-chromium) system," *Journal of Phase Equilibria,* vol. 19, pp. 367-375, 1998.

[126] H. Okamoto, "Al-Cr (Aluminum-Chromium)," *Journal of Phase Equilibria and Diffusion,* vol. 29, pp. 112-113, 2008.

[127] J. L. Murray, "The Ti−V (Titanium-Vanadium) system," *Bulletin of Alloy Phase Diagrams,* vol. 2, pp. 48-55, 1981.

[128] J. L. Murray, "The Cr−Ti (chromium-titanium) system," *Bulletin of Alloy Phase Diagrams,* vol. 2, pp. 174-181, 1981.

[129] J. L. Murray, "The Cr-Ti (Chromium-Titanium) system," in *Phase Diagrams of Binary Titanium Alloys*, J. L. Murray, Ed., ed Metals Park OH: ASM, 1987, p. 68.

[130] J. Smith, D. Bailey and O. Carlson, "The Cr−V (Chromium-Vanadium) system," *Journal of Phase Equilibria,* vol. 2, pp. 469-473, 1982.

[131] J. Murray, "Al-V (aluminum-vanadium)," *Journal of Phase Equilibria,* vol. 10, pp. 351-357, 1989.

[132] F. H. Hayes, "Al-Ti-V (aluminum-titanium-vanadium) system," *Journal of Phase Equilibria,* vol. 16, pp. 163-176, 1995.

[133] V. Raghavan, "Al-Ti-V (aluminum-titanium-vanadium)," *Journal of Phase Equilibria and Diffusion,* vol. 26, pp. 276-279, 2005.

[134] F. H. Hayes, "The al-cr-ti system (aluminum-chromium-titanium)," *Journal of Phase Equilibria,* vol. 13, pp. 79-86, 1992.

[135] E. Ence, P. A. Farrar and H. Margolin, "The Ti-Al phase diagram," Wright Air Development Division1960.

[136] V. Raghavan, "Al-Cr-Ti (aluminum-chromium-titanium)," *Journal of Phase Equilibria and Diffusion,* vol. 26, pp. 349-356, 2005.

[137] M. Enomoto, "The Cr-Ti-V system (chromium-titanium-vanadium)," *Journal of Phase Equilibria,* vol. 13, pp. 195-200, 1992.

[138] I. I. Kornilov, E. N. Pylaeva, M. A. Volkova, P. I. Kripyakevich and V. Y. Markiv, "Phase structure of alloys in the binary system Ti-Al containing from 0 to 30% Al," *Doklady Akademii Nauk SSSR,* vol. 161, pp. 843-846, 1965.

[139] K. Ouchi, Y. Iijima and K. Hirano, "Interdiffusion in Ti-Al system," in *Titanium '80. Science and Technology*. vol. 1, H. Kimura and O. Izumi, Eds., ed: TMS, 1980, pp. 559-568.

[140] P. L. Martin, H. A. Lipsitt, N. T. Nuhfer and J. C. Williams, "The effects of alloying on the microstructure and properties of Ti_3Al and TiAl," in *Titanium '80. Science and Technology*. vol. 2, H. Kimura and O. Izumi, Eds., ed: TMS, 1980, pp. 1245-1254.

[141] E. W. Collings, "Magnetic investigations of electronic bonding and α through γ phase equilibria in the titanium aluminum system," in *Titanium and Titanium Alloys*. vol. 2, J.C. Williams and A. F.

Belov, Eds., ed New York: Plenum Press, 1982, pp. 1391-1402.

[142] R. M. Waterstrat, "Effect of intersititial elements on phase relationships in the titanium-aluminum system, NISTIR 88-3856," US Department of Commerce1988.

[143] A. Suzuki, M. Takeyama and T. Matsuo, "Transmission electron microscopy on the phase equilibria among , and 2 phases in Ti-Al binary system," *Intermetallics,* vol. 10, pp. 915-924, 2002.

[144] E. Ence and H. Margolin, "Phase relations in titanium-aluminum system," *Metallurgical Society of American Institute of Mining, Metallurgical and Petroleum Engineers -- Transactions,* vol. 221, pp. 151-157, 1961.

[145] P. A. Farrar and H. Margolin, "Air Force Materials Labotary Technology Report 65-69," Air Force Materials Labotary1965.

[146] L. A. Willey and H. Margolin, "Al-Ti Aluminium-Titanium," in *Metals Handbook*, T. Lyman, Ed., 8th ed Metals Park OH: ASM, 1973, p. 264.

[147] D. Clark, K. S. Jepson and G. I. Lewis, "A study of the titanium - aluminium system up to 40 At.-% aluminium," *Journal of the Institute of Metals,* vol. 91, pp. 197-203, 1963.

[148] I. I. Kornilov, T. T. Nartova and S. P. Chernyshova, "The Ti-rich range of the Ti-Al phase diagram," *Russian Metallurgy,* vol. 6, pp. 156-161, 1976.

[149] T. Tsujimoto and M. Adachi, "Reinvestigation of titanium-rich region of titanium-aluminium equilibrium diagram," *Journal of the Institute of Metals,* vol. 94, pp. 358-363, 1966.

[150] T. Tsujimoto and M. Adachi, "Study on the titanium-rich region of the titanium-aluminium equilibrium diagram," *Transactions of National Research Institute for Metals,* vol. 9, pp. 69-81, 1967.

[151] H. Sasano and T. Tsujimoto, "On the quenched structure and aging process of Ti-8~15.8wt%Al alloy," in *Titanium Science and Technology*. vol. 3, R.I. Jaffee and H. M. Burte, Eds., ed New York: Plenum Press, 1973, pp. 1635-1647.

[152] T. J. Jewett and M. Dahms, "Stability of the Ti(Cr,Al)$_2$ phase," *Zeitschrift fur Metallkunde,* vol. 87, pp. 254-261, 1996.

[153] H. Wang, N. Warnken and R. C. Reed, "Thermodynamic and kinetic modeling of bcc phase in the Ti-Al-V ternary system," *Materials Science and Engineering A,* vol. 528, pp. 622-630, 2010.

[154] Q. Chen, N. Ma, K. S. Wu and Y. Z. Wang, "Quantitative phase field modeling of diffusion-controlled precipitate growth and dissolution in Ti-Al-V," *Scripta Materialia,* vol. 50, pp. 471-476, 2004.

[155] T. Takahashi, Y. Minamino and M. Komatsu, "Interdiffusion in phase of the ternary Ti-Al-V system," *Materials Transactions,* vol. 49, pp. 125-132, 2008.

[156] L. Huang, Y. W. Cui, H. Chang, H. Zhong, J. S. Li and L. Zhou, "Assessment of atomic mobilities for BCC phase of Ti-Al-V system," *Journal of Phase Equilibria and Diffusion,* vol. 31, pp. 135-143, 2010.

[157] K. C. H. Kumar, P. Wollants and L. Delaey, "Thermodynamic calculation of Nb-Ti-V phase diagram," *Calphad,* vol. 18, pp. 71-79, 1994.

[158] W. P. Gong, Y. Du, B. Y. Huang, R. Schmid-Fetzer, C. F. Zhang and H. H. Xu, "Thermodynamic reassessment of the Al-V system," *Zeitschrift fuer Metallkunde/Materials Research and Advanced Techniques,* vol. 95, pp. 978-986, 2004.

[159] J. S. Kirkaldy, "Diffusion in multicomponent metallic systems," *Canadian Journal of Physics,* vol. 35, pp. 435-440, 1957.

[160] J. S. Kirkaldy, J. E. Lane and G. R. Mason, "Diffusion in multicomponent metallic systems -- Solutions of multicomponent diffusion equations with variable coefficients," *Canadian Journal of Physics,* vol. 41, pp. 2174-2186, 1963.

[161] P. Zhou, S. L. Cui, D. D. Liu, L. J. Zhang, Y. Du and W. Q. Jie, "Assessment of the atomic mobilities for Fcc_A1 and Bcc_A2 Cu-Fe-Zn alloys," in *CALPHAD XL*, Rio de Janeiro, Brazil, 2011.

[162] W. W. Mullins and R. F. Sekerka, "Morphological stability of a particle growing by diffusion or heat flow," *Journal of Applied Physics,* vol. 34, pp. 323-329, 1963.

[163] W. W. Mullins and R. F. Sekerka, "Stability of a planar interface during solidification of a dilute binary alloy," *Journal of Applied Physics,* vol. 35, pp. 444-451, 1964.

[164] T. Furuhara and T. Maki, "Variant selection in heterogeneous nucleation on defects in diffusional phase transformation and precipitation," *Materials Science and Engineering A,* vol. 312, pp. 145-154, 2001.

[165] T. Furuhara, T. Makino, H. Watanabe and T. Maki, "Crystallography of sideplates in a titanium alloy," in *Proceedings of International Conference on Solid-Solid Phases Transformations in Inorganic Materials '94, 17-22 July 1994*, Warrendale, PA, USA, 1994, pp. 237-242.

[166] H. I. Aaronson, G. Spanos, R. A. Masamura, R. G. Vardiman, D. W. Moon, E. S. K. Menon and M. G. Hall, "Sympathetic nucleation: an overview," *Materials science and engineering. B,* vol. 32, pp. 107-123, 1995.

[167] N. Stanford and P. S. Bate, "Crystallographic variant selection in Ti-6Al-4V," *Acta Materialia,* vol. 52, pp. 5215-5224, 2004.

[168] D. Bhattacharyya, G. B. Viswanathan, R. Denkenberger, D. Furrer and H. L. Fraser, "The role of crystallographic and geometrical relationships between and phases in an / titanium alloy," *Acta Materialia,* vol. 51, pp. 4679-4691, 2003.

[169] T. Furuhara, S. Takagi, H. Watanabe and T. Maki, "Crystallography of grain boundary precipitates in a titanium alloy," *Metallurgical and Materials Transactions A,* vol. 27, pp. 1635-1646, 1996.

[170] S. Malinov and W. Sha, "Modeling thermodynamics, kinetics, and phase transformation morphology while heat treating titanium alloys," *The Journal of The Minerals, Metals and Materials Society* vol. 57, pp. 42-45, 2005.

[171] S. Malinov, Z. Guo, W. Sha and A. Wilson, "Differential scanning calorimetry study and computer modeling of beta to alpha phase transformation in a Ti-6Al-4V alloy," *Metallurgical and Materials Transactions A,* vol. 32, pp. 879-887, 2001.

[172] I. Katzarov, S. Malinov and W. Sha, "Finite element modeling of the morphology of beta to alpha phase transformation in Ti-6Al-4V alloy," *Metallurgical and Materials Transactions A,* vol. 33, pp. 1027-1040, 2002.

[173] S. Semiatin, S. Knisley, P. Fagin, D. Barker and F. Zhang, "Microstructure evolution during alpha-beta heat treatment of Ti-6Al-4V," *Metallurgical and Materials Transactions A,* vol. 34, pp. 2377-2386, 2003.

[174] M. P. Ginebra, F. X. Gill, J. M. Manero and J. A. Planell, "Effects of solution and cooling rate on the Widmanstätten morphologies in the Ti-6Al-4V alloy," in *Titanium '95 Science and Technology*, Birmingham, UK, 1995, pp. 2563-2569.